



# KOCAELI JOURNAL OF SCIENCE AND ENGINEERING

## Owner

Prof. Dr. Sadettin HÜLAGÜ - (Kocaeli University)

## Editor in Chief

Prof. Dr. K. Süleyman YİĞİT - (Kocaeli University)

## Editors

Prof. Dr. Murat HOŞÖZ - (Kocaeli University)  
Assoc. Prof. Dr. H. Hakan GÜREL - (Kocaeli University)  
Assoc. Prof. Dr. Mihriban CİVAN - (Kocaeli University)  
Asst. Prof. Dr. Recep Kaya GÖKTAŞ- (Kocaeli University)

## Production Editors

R.A. Abdurrahman GÜN - (Kocaeli University)  
Lecturer Yusuf YAĞCI - (Kocaeli University)

## Copy Editor (English)

Lecturer İsmail Hakkı PASLI - (Kocaeli University)

## Asistant Editors

Asst. Prof. Dr. Alp Eren ŞAHİN - (Kocaeli University)  
R.A. Abdurrahman GÜN - (Kocaeli University)

## Secretary

Durmuş İMAT - (Kocaeli University)

## Section Editors

Prof. Dr. Adem TEKİN (İTU)  
Prof. Dr. Adnan SÖZEN (Gazi University)  
Assoc. Prof. Dr. Ahmet SAYAR (Kocaeli University)  
Prof. Dr. Ahmet Ziyaettin ŞAHİN (KFUPM, S.A.)  
Prof. Dr. Aleksandrs SOSTAKS (University of Latvia)  
Assoc. Prof. Dr. Ali TÜRKCAN (Kocaeli University)  
Asst. Prof. Dr. Atakan ALKAN (Kocaeli University)  
Assoc. Prof. Dr. Başar UYAR (Kocaeli University)  
Prof. Dr. Beyhan PEKEY (Kocaeli University)  
Prof. Dr. Bülent ORUÇ (Kocaeli University)  
Prof. Dr. Cihan KARAKUZU (Bilecik Şeyh Edebali University)  
Prof. Dr. Dilek ODAÇI DEMİRKOL (Ege University)  
Asst. Prof. Dr. Dilek OKUYUCU (Erzurum Technical University)  
Asst. Prof. Dr. Ekin EKİNCİ (Sakarya University of Applied Sciences)  
Prof. Dr. Engin ÖZDEMİR (Kocaeli University)  
Prof. Dr. Fatma GÜLTEKİN (Karadeniz Technical University)  
Prof. Dr. Fatma KANCA (Fenerbahçe University)  
Prof. Dr. Günay ÖZTÜRK (İzmir Demokrasi University)  
Prof. Dr. Hakan PEKEY (Kocaeli University)  
Assoc. Prof. Dr. Halil YİĞİT (Kocaeli University)  
Assoc. Prof. Dr. Halim Aytekin ERGÜL (Kocaeli University)  
Prof. Dr. Hamid EL-QARNIA (Cadi Ayyad University)

Dr. Helena AZEVEDO (Queen Mary University of London)  
Prof. Dr. Hüseyin Metin ERTUNÇ (Kocaeli University)  
Prof. Dr. İulian STANASEL (University of Oradea)  
Asst. Prof. Dr. İbrahim MUTLU (Kocaeli University)  
Prof. Dr. Kerem KÜÇÜK (Kocaeli University)  
Asst. Prof. Dr. Mehlika KOCABAŞ AKAY (Kocaeli University)  
Asst. Prof. Dr. Mehmet Aytaç ÇINAR (Kocaeli University)  
Prof. Dr. Mehmet BAYRAK (Sakarya University)  
Prof. Dr. Mustafa ÇANAKCI (Kocaeli University)  
Asst. Prof. Dr. Mustafa Hikmet Bilgehan UÇAR (Kocaeli University)  
Assoc. Prof. Dr. Müslüm ARICI (Kocaeli University)  
Assoc. Prof. Dr. Oana Delia STANASEL (University of Oradea)  
Prof. Dr. Özer YILMAZ (Bursa Uludağ University)  
Prof. Dr. Semra BORAN (Sakarya University)  
Asst. Prof. Dr. Suhap ŞAHİN (Kocaeli University)  
Asst. Prof. Dr. Şaban Hakan ATAPEK (Kocaeli University)  
Prof. Dr. Tamer SINMAZÇELİK (Kocaeli University)  
Prof. Dr. Recep Taygun GÜRDAY (Kocaeli University)  
Prof. Dr. Yunus Emre ERDEMLİ (Kocaeli University)  
Prof. Dr. Zerrin ALADAĞ (Kocaeli University)  
Asst. Prof. Dr. Zeynep Hilal KİLİNCİ (Kocaeli University)

## Advisory Board

Assoc. Prof. Dr. Ahmet KARAKAŞ (Kocaeli University)  
Prof. Dr. Ali KILIÇARSLAN (Hitit University)  
Prof. Dr. Ali SÜRMELEN (Uludağ University)  
Prof. Dr. Ata ATUN (Cyprus Science University)  
Asst. Prof. Dr. Ayşe Arzu ARI (Kocaeli University)  
Prof. Dr. Ayşe Nilgün AKIN (Kocaeli University)  
Assoc. Prof. Dr. Burcu ONAT (İstanbul University)  
Asst. Prof. Dr. Canan Dilek EREN (Kocaeli University)  
Prof. Dr. Cenk SAYIN (Marmara University)  
Prof. Dr. Dong LI (Northeast Petroleum University)  
Asst. Prof. Dr. Emre KİSHALI (Kocaeli University)  
Prof. Dr. Erhan PULAT (Bursa Uludağ University)  
Prof. Dr. Fadime SERTÇELİK (Kocaeli University)  
Prof. Dr. Hasan KÜRÜM (Firat University)  
Assoc. Prof. Dr. Hikmet SÜRMELE (Mersin University)  
Assoc. Prof. Dr. İlyas KANDEMİR (Gebze Technical University)  
Prof. Dr. Kamaruzzaman SOPIAN (The National University of Malaysia)  
Assoc. Prof. Dr. Kasım BAYNAL (Kocaeli University)  
Prof. Dr. Mehmet YILMAZ (Kocaeli University)  
Prof. Dr. Mehmet ARIK (Özyeğin University)

Assoc. Prof. Dr. Mehmet Ufuk KASIM (Kocaeli University)  
Assoc. Prof. Dr. Murat Selim ÇEPNİ (Kocaeli University)  
Prof. Dr. Nevim GENÇ (Kocaeli University)  
Prof. Dr. Nil Pembe ÖZER (Kocaeli University)  
Prof. Dr. Nilgün FIĞLALI (Kocaeli University)  
Prof. Dr. Nurhan Turgut DUNFORD (Oklahoma State University)  
Prof. Dr. Oğuzhan URHAN (Kocaeli University)  
Assoc. Prof. Dr. Onur ÇOBAN (Kocaeli University)  
Prof. Dr. Oscar CASTILLO (Tijuana Institute of Technology)  
Prof. Dr. Özcan GÜNDOĞDU (Kocaeli University)  
Prof. Dr. Raşit KÖKER (Sakarya University)  
Prof. Dr. Rezzan KASIM (Kocaeli University)  
Prof. Dr. Safa Bozkurt ÇOŞKUN (Kocaeli University)  
Prof. Dr. Serdar İPLİKÇİ (Pamukkale University)  
Prof. Dr. Sezai TOKAT (Pamukkale University)  
Prof. Dr. Şeref Naci ENGİN (Yıldız Technical University)  
Prof. Dr. Tahsin ENGİN (Sakarya University)  
Assoc. Prof. Dr. Vildan ÇETKİN (Kocaeli University)  
Assoc. Prof. Dr. Wang FUQIANG (Harbin Institute of Technology)

## Printed By

Kocaeli University - Graduate School of Natural and Applied Sciences - Umuttepe Campus 41001, Kocaeli / TURKEY

Tel: +090 (262) 303 35 56 Fax: +090 (262) 303 30 33 E-mail: kojose@kocaeli.edu.tr



**COVER PAGE** ..... I

**EDITORIAL AND ADVISORY BOARDS** .....II

**TABLE OF CONTENTS** ..... III

**Osman KABASAKAL, Alev MUTLU**

Named Entity Recognition in Turkish Bank Documents..... 86-92  
(*Research Paper*)

**Özgür Fatih ÇÜMEN, Ahmet KARAKAŞ**

Engineering Geological Investigation of the Kırık Tunnel Route..... 93-102  
(*Research Paper*)

**Emel OKKALI, Hilmiye ATAMTÜRK, Zeynep Hilal KİLİMCİ**

Evaluation of Society Response to Violence against Women in Turkey via Twitter  
using Topic Modeling..... 103-112  
(*Research Paper*)

**Elif DOĞAN, Ayşe Elif BÜYÜKBAYRAM**

Conducting Polymer Based Enzyme Electrodes Fabricated by Invertase and  
Polyphenol Oxidase ..... 113-119  
(*Research Paper*)

**Sonjoh CHEBELEM, Hakan ERDOĞAN**

Effect of Pylon Shapes on Seismic Response of a Long-Span Steel Box-Girder  
Cable-Stayed Bridge ..... 120-127  
(*Research Paper*)

**Serap YEŞİLKIR BAYDAR, Rabia ÇAKIR KOÇ, Yasemin BUDAMA KILINÇ,  
Burak ÖZDEMİR, Zeynep KARAVELİOĞLU**

Fabrication and Characterization of Persea Gratissima Oil Loaded Chitosan  
Nanoparticles and Investigation of Its Neuroprotective Effects..... 128-135  
(*Research Paper*)

**Mehmet GÜL**

Representing American Sign Language Letters and Numbers with Humanoid  
Robot Arm..... 136-145  
(*Research Paper*)

**Tuğcan KORAK, Murat KASAP**

Searching for the Roots of Bloom Syndrome Protein and Its Homologs Using  
Phylogenetic Analysis..... 146-159  
(*Research Paper*)

**Ergin ULUTAŞ, Özkan CORUK, Ahmet KARAKAŞ**

Local Geology Effects on Soil Amplification and Predominant Period in Düzce  
Basin, NW Turkey..... 160-170  
(*Research Paper*)

**Kemal ERMİŞ, Hüseyin ÜNAL**

Tribological Behavior of Ultra-High Molecular Weight Polyethylene Polymer  
with Artificial Neural Network Modeling..... 171-178  
(*Research Paper*)



## Named Entity Recognition in Turkish Bank Documents

Osman KABASAKAL<sup>1</sup> , Alev MUTLU<sup>2,\*</sup> 

<sup>1</sup> Department of Computer Engineering, Kocaeli University, Kocaeli, 41001, Turkey, **ORCID:** 0000-0003-1187-5147

<sup>2</sup> Department of Computer Engineering, Kocaeli University, Kocaeli, 41001, Turkey, **ORCID:** 0000-0003-0547-0653

### Article Info

#### Research paper

Received : January 31, 2021

Accepted : April 13, 2021

#### Keywords

Bank Document  
Conditional Random Fields  
Named Entity Recognition  
Natural Language Processing  
Turkish Documents

### Abstract

Named Entity Recognition (NER) is the process of automatically recognizing entity names such as person, organization, and date in a document. In this study, we focus on bank documents written in Turkish and propose a Conditional Random Fields (CRF) model to extract named entities. The main contribution of this study is twofold: (i) we propose domain-specific features to extract entity names such as law, regulation, and reference which frequently appear in bank documents; and (ii) we contribute to NER research in Turkish document which is not as mature as other languages such as English and German. Experimental results based on 10-fold cross validation conducted on 551 real-life, anonymized bank documents show the proposed CRF-NER model achieves 0.962 micro average F1 score. More specifically, F1 score for the identification of law names is 0.979, regulation name is 0.850, and article no is 0.850.

## 1. Introduction

Named Entity Recognition (NER) is the process of automatically recognizing named entities in a text document and mapping them to semantic categories such as person, place, organization, time, and date. It is one of the most studied tasks of natural language processing and has applications in domains such as keyword extraction [1], question answering [2], text clustering [3], and text summarization [4].

The NER problem was first defined in MUC-6 [5], and since then several NER systems have been proposed. Based on the learning technique, these systems can be classified as rule-based [6, 7], unsupervised [8], supervised [9, 10], and semi-supervised [11]. Rule-based systems are among the earliest NER attempts and employ gazetteer information and hand-crafted rules to identify and classify named entities. Such systems have high precision and low recall due to domain-dependent and user-defined rules. Unsupervised approaches are generally based on the

clustering of a large corpus. These systems identify and classify named entities based on the context similarity of clustered documents. In supervised techniques, NER is formulated as a multi-class classification problem. In supervised NER, words are represented using word-, document-, and corpus-level features and learning algorithms such as support vector machines (SVM) and decision trees; sequence labeling algorithms including conditional random fields (CRF) and Hidden Markov Models (HMM) are used. Supervised learning builds models on annotated data, which is labor-intensive and requires domain expertise to attain. Semi-supervised learning algorithms aim to overcome document annotating problem of supervised learning algorithms by extending limited annotated data by self-labeled unlabeled data. More recently, NER systems based on deep learning models are also proposed [12, 13]. Such systems benefit from the ability to discover hidden features automatically [14].

NER systems can also be classified as generic and domain-specific based on the type of named entities they aim to recognize. The former focuses on identifying generic named entities such as organization, person, location, and percentage. The latter, on the other hand,

\* Corresponding Author: [alev.mutlu@kocaeli.edu.tr](mailto:alev.mutlu@kocaeli.edu.tr)



aims at learning domain-specific named entities such as adverse drug reactions [15], legal norms [16], and chemical entities [17].

In this study, we propose a domain-specific CRF-based NER system to recognize named entities in bank documents. The proposed system aims to recognize domain-specific named entities such as money amount, law name, regularity law, law article, and reference. Moreover, the proposed system is modeled to recognize generic named entities including organization, date, time duration, abbreviation, and e-mail. This study does not focus on place and person categories as such entities are removed from documents due to privacy concerns.

To evaluate the performance of the proposed features' in identifying named entities in bank documents, we conducted experiments on real-life anonymized bank documents. The experimental results show a 0.962 micro-averaged F1-score. Considering the domain-specific named entities, 0.850, 0.979, 0.975, and 0.947 F1-scores are achieved, respectively, for regulation, law name, article number, and money amount.

The rest of the paper is organized as follows. In Section 2, we introduce CRF-based named entity recognition. In Section 3, we introduce the domain-specific features proposed for the bank domain. Section 4 presents the experimental findings, and the last section concludes the paper with possible future directions.

## 2. Background

This section introduces CRF-based named entity recognition and later provides a literature summary related to named entity recognition in Turkish, financial, and legal domains.

Conditional Random Fields are statistical methods for sequence modeling. They are undirected graphical models that consider context while determining a sequence label. CRF aims to learn the conditional probability of values on designated output nodes given values of the designated input nodes. More specifically, let  $o = \langle o_1, o_2, \dots, o_n \rangle$  be observed input sequence and  $s = \langle s_1, s_2, \dots, s_T \rangle$  be a state sequence corresponding to labels assigned to observations in  $o$ , the conditional probability is calculated as in Equation (1).

$$P(s|o) = \frac{1}{Z_o} \exp \left( \sum_{i=1}^n \sum_{j=1}^m \lambda_j f_j(s_{i-1}, s, o, i) \right) \quad (1)$$

In Equation (1),  $Z_o$  is a normalization factor,  $f_j(s_{i-1}, s, o, i)$  is one of  $m$  functions that describe a feature, and  $\lambda_j$  is a learned weight. Training in CRF corresponds to

maximize the learned weights such that a learned weight,  $\lambda_j$ , for each feature,  $f_j$ , should be positive when there is a correlation with the target label, negative when there is an anti-correlation, and close to 0 when uninformative.

One of the earliest studies on Turkish NER is presented in [18]. The authors of the study propose a method to model morphological and contextual patterns for named entity recognition.

A rule-based NER for generic named entities for Turkish is proposed in [19]. The authors contribute to the literature by evaluating a rule-based NER system on diverse types of text documents.

A recent study [20] investigates the effect of different features in CRF-based NER performance for Turkish. To this aim, the authors investigate the effect of different positional and semantic features on the performance of NER in generic Turkish named entities.

A rule-based NER system for financial documents was introduced in [21]. The authors aim to identify organization, person, and location names by defining hand-crafted rules.

A rule-based system that aims to extract specific information, namely current/previous financial factor, current/previous volume, change type, and volume from financial documents is introduced in [22]. The authors induce rules to extract such entity names using symbolic learning model trained by greedy and tabu search.

A CRF-based NER system to identify stock names, company names and their abbreviations from financial documents is introduced in [23]. To recognize company names, the authors define features regarding suffix keys and location names. The authors define features based on mutual information and information entropy between full names and abbreviations to identify abbreviated stock names.

A NER system to support credit risk assessment is introduced in [24]. The authors present a CRF-based NER model to extract person, organization, location, and miscellaneous entities from financial documents. The study contributes to the literature by enhancing domain-data with a large amount of out-of-domain annotated data to improve performance.

A NER system to identify person names from Turkish financial news is presented in [25]. The authors define local grammars based on reporting verbs to identify person names. The study concludes that the local grammars are successful in named entity extraction; however, they are difficult to construct due to Turkish word-formation.

A NER system to identify legal name entities such as legal norm, ordinance, court decision as well as generic named entities such as person, location, and organization is for German legal documents is introduced in [26]. The

authors make use of gazetteers of persons, locations, and laws to improve performance further. The authors compare CRF- and BiLSTM-based NER systems and conclude that the BiLSTM model is superior over the CRF model.

A deep learning model for NER to recognize court names, judgment date petitioner, respondent, judge name, and act entities in legal documents is proposed in [27]. The authors propose a four-layer CNN model wherewith residual connections and the max out activation function to perform the encoding step.

The NER system proposed in this study differs from [21,24,25] as it does not require defining domain-specific rules, which require expert knowledge, are costly, and difficult to keep up-to-date. The proposed NER system differs from [25] as it works only with binary attributes.

The proposed study also differs from [24] as it aims to identify a larger number of named entities. The proposed method differs from [26], as it does not need external resources such as gazetteers.

### 3. NER for Bank Documents

In Table 1, we list the categories that the proposed NER system aims to recognize. Table 1 also provides a brief description of these categories and gives some examples for each category. There are ten categories, the first four of which are generic, and the last six are domain-specific. In this study, we do not aim to recognize locations and person names, as the bank documents we are working on are anonymized.

**Table 1.** Semantic Categories and their definition.

Category	Symbol	Explanation	Example
E-mail	EMA	E-mail addresses	yonetim@banka.com.tr
Time duration	ZAM	This entity indicates time durations or time intervals	yedi gün içinde, 1 yıllık dönem
Organization	ORG	Indicates an organization name	Türkiye Cumhuriyeti Merkez Bankası
Date	TAR	Indicates a date	11/05/2020, 13 Ocak 2020
Money amount	PAR	Indicates the amount of money	2 TL, 85 Avro
Article number	MAD	A paragraph or section of a legal document or statute	28 inci madde
Abbreviation	KIS	A shortened form of a name or phrase	IBAN, DAB
Law name	KAN	Name of law	Elektronik Para Kuruluşları hakkında kanun 5. maddesi
Reference	ILG		131161/A sayılı yatırım
Ordinance	YON	Rules and regulations created by federal and state agencies.	Bankaların Kredi İşlemlerine İlişkin Yönetmelikte

To recognize these named entities, we defined the following nine features.

- POS: Each word has a feature indicating its part-of-speech tag.
- isNumber: This is a boolean feature indicating either a token is a number or not.
- isCapital: This feature indicates either a token is all capitalized, letter case or small case. Our observation is that all capitalized tokens are generally abbreviations. Organization names are letter cases.
- containsAt: This is a boolean feature indicating if a term contains the “@” sign. This feature is used to help recognize e-mails.
- isTime: This is a boolean feature indicating if a token contains “:” sign or precedes the term “saat”.
- isDate: This is a boolean value indicating if a number is followed or preceded by a month

name or includes the “/” sign.

- isTimeInterval: This is a boolean feature that indicates if a term is followed by “gün”, “ay” or “yıl”.
- precedesYonetmelik: This is a boolean feature that indicates if a term precedes a term that includes “yönet”. Our observation is that the length of regulation names ranges from 4 to 14 tokens. Hence, we look ahead to 4 to 10 tokens to set this feature to true.
- precedesCurrency: This is a Boolean feature indicating if a term precedes currency names such as “Avro”, “Euro”.

We implemented the proposed model using Python’s sklearn-crfsuite library. L-BFGS is used to train the model. Figure 1 is a snapshot of a sample input file. The named entities recognized for this file along with their tags are listed in Table 2.

Resmi Gazetenin 01.03.2006 tarih ve 26095 sayılı nüshasında yayımlanarak yürürlüğe giren 5464 sayılı Banka Kartları ve Kredi Kartları Kanununun 9 uncu maddesinin ikinci fıkrası “*Kart çıkaran kuruluş tarafından bir gerçek kişinin sahip olduğu tüm kredi kartları için tanınacak toplam kredi kartları limiti, ilk yıl için, ilgilinin aylık ortalama net gelirinin iki katını, ikinci yıl için ise, dört katını aşamaz. Bu fıkra uygulamasında bin Yeni Türk Lirasına kadar limitler hariç olmak üzere, aylık veya yıllık ortalama gelir düzeyi kart hamili tarafından beyan edilen ve ilgili kuruluşlarca teyit edilen gelirler üzerinden tespit edilir.*” hükmünü amirdir.

Figure 1. Sample Input File

Table 2. Sample output of the named entites

Resmi - ORG
Gazetenin - ORG
01.03.2006 - TAR
26095 - ILG
5464 - ILG
Banka - KAN
Kartları - KAN
ve - KAN
Kredi - KAN
Kartları - KAN
Kanununun - KAN
9 - MAD
uncu - MAD
maddesinin - MAD
ikinci - ZAM
yıl - ZAM
Yeni - PAR
Türk - PAR
Lirasına - PAR
aylık - ZAM
yıllık - ZAM

## 4. Experiments

This section introduces the dataset used in the experiments, the data preprocessing procedure, and the experimental setting. Next, we present and discuss the experimental findings.

### 4.1. Experimental Setting

The dataset used to evaluate the proposed NER system's performance consists of 551 real-life, anonymized bank documents. The documents' length ranges from 7 to 633 words, with an average length of 99 words. In Table 3, we list the distribution of the categories over the documents. As the categories' distribution indicates, domain-related categories such as law name, article number, and regulation law frequently appear within the dataset. On the other hand, instances related to e-mail and abbreviation categories are less frequent.

Table 3. Distribution of the semantic categories

Category name	#	%
E-mail	11	0.12
Time duration	497	5.56
Ordinance	560	6.27
Date	1044	11.69
Money amount	388	4.34
Organization	2688	30.09
Article no	1605	17.97
Abbreviation	250	2.80
Law name	994	11.13
Reference	897	10.04
Total	9430	100

The documents we conducted experiments on are in PDF format. To convert the files into text format, we used PyTesseract<sup>†</sup>, Python's optical character recognition tool. The documents consist of three sections: title, main text, and signature section. As the documents are structured, we wrote a script that extracts the main text from the documents. To tokenize the main text and determine the POS-tags, we used Zemberek<sup>‡</sup>. Named entity recognition is applied to the main text of the documents.

To evaluate category-based performance, precision, recall, and F1-score are used. Precision in NER is formulated in (2). It refers to the fraction of the correctly predicted named entities for a category (COR) over the total number of the category predictions (ACT). Recall refers to the number of correct predictions for a category (COR) over the number of instances that belong to that category (POS). Recall is formulated in (3). F1-score refers to the harmonic mean of precision and recall and is formulated in (4).

$$\text{Precision} = \frac{\text{COR}}{\text{ACT}} \quad (2)$$

$$\text{Recall} = \frac{\text{COR}}{\text{POS}} \quad (3)$$

<sup>†</sup> <https://pypi.org/project/pytesseract/>

<sup>‡</sup> <https://github.com/ahmetaa/zemberek-nlp>



$$F1 - \text{score} = 2 * \frac{\text{Precision} * \text{Recall}}{\text{Precision} + \text{Recall}} \quad (4)$$

To evaluate the overall performance of the proposed system, we employ the micro-averaged F1-score. Micro-averaged F1-score is preferred when there is a class imbalance. Micro-averaged F1 is formulated in (5), where  $n$  indicates the number of classes,  $TP_i$  indicates the number of true positive predictions for class  $i$ , and  $FP_i$  indicates the false positive predictions for class  $i$ .

$$\text{MicroAveraged} - F1 = \sum_{i=1}^n \frac{TP_i}{TP_i + FP_i} \quad (5)$$

The experimental results presented below are based on 10-fold cross validation. At each fold, 90% of the data is used for training and the remaining 10% of the data is used for testing.

## 4.2. Experimental Results

In Table 4, we report class-based precision, recall, and F1-scores. As the results indicate, the highest precision and the lowest recall values are achieved for the e-mail category. This is an expected result as there are only 11 instances that belong to the e-mail category. When the confusion matrix given in Table 5 is examined, one can observe that 8 out of 11 e-mail instances are correctly predicted, while the remaining 3 are misclassified as other. This may due to the fact that, no e-mail instances are present in training sets during some folds. Category

ordinance ranks the second-worst in terms of F1-score. The rest of categories achieve F1-scores around 0.97. The system achieves 0.962 micro-averaged F1-score.

A recent study [26] that focuses on legal documents reports an F1-score 0.867 for the ordinance category, 0.966 for law names. Compared to that system, the proposed features achieve similar results, 0.850 and 0.979 for ordinance and law name, respectively. The proposed NER system is superior over [26] when compared with respect to the organization category. The proposed NER system achieves 0.973 F1-score while [26] reports at a rate of 0.908.

**Table 4.** Category-based results

Category	Precision	Recall	F1-Score
E-mail	1.0	0.73	0.842
Time duration	0.97	0.84	0.900
Ordinance	0.92	0.79	0.850
Date	0.98	0.99	0.986
Money amount	0.97	0.93	0.947
Organization	0.97	0.98	0.973
Article no	0.98	0.99	0.985
Abbreviation	0.93	0.92	0.926
Law name	0.97	0.99	0.979
Reference	0.99	0.98	0.984

In Table 5, we present the confusion matrix. As the results indicate, most of the misclassifications are assigned to the category *other*.

**Table 5.** The confusion matrix

		Predicted											
		ORG	PAR	KAN	YON	ILG	TAR	ZAM	KIS	EMA	MAD	OTHER	
Actual	ORG	2631	0	0	0	0	0	0	1	0	0	56	
	PAR	0	360	0	0	2	4	0	5	0	0	17	
	KAN	0	0	981	0	0	0	0	3	0	0	10	
	YON	0	0	0	441	0	0	0	0	0	0	119	
	ILG	0	1	3	0	879	8	0	0	0	0	6	
	TAR	0	0	0	0	1	1034	2	0	0	0	7	
	ZAM	0	0	0	0	0	0	418	0	0	0	79	
	KIS	1	3	0	0	3	0	0	231	0	0	12	
	EMA	0	0	0	0	0	0	0	0	8	0	3	
	MAD	0	0	2	0	0	0	0	0	0	1593	10	
	OTHER	87	8	25	37	4	8	12	9	0	35	35117	

## 5. Conclusion

In this study, we focused on bank documents to recognize domain-specific categories such as law-name, ordinance, and article no. To this aim, we trained a CRF-based NER system with nine features. The experimental results show that the achieved results are comparable to those reported in the literature.

As a future work, we plan to annotate data using the

IOB standard and reevaluate the proposed features' performance.

## Declaration of Ethical Standards

The authors of this article declare that the materials and methods used in this study do not require ethical committee permission and/or legal-special permission.

## Conflict of Interest

The authors declare that they have no known competing financial interests or personal relationships that could have appeared to influence the work reported in this paper.

## Acknowledgements

This work is partially supported by TUBITAK under grant number 5190074. The authors would like to thank Dr. Kerem Kucuk and Mahir Temur for their valuable comments on this work.

## References

- [1] Nagy I., Berend G., Vincze V., 2011. Noun compound and named entity recognition and their usability in keyphrase extraction. International Conference Recent Advances in Natural Language Processing, Hissar, Bulgaria, 12-14 September.
- [2] Rodrigo A., Perez-Iglesias J., Penas A., Garrido G., Araujo L., 2013. Answering questions about European legislation. Expert Systems with Applications, **40**(15), pp. 5811-5816.
- [3] Cao T. H., Tang T. M., Chau C. K., 2012. Text clustering with named entities: a model, experimentation and realization. In Data mining: Foundations and intelligent paradigms, Springer, Berlin, Heidelberg.
- [4] Hassel M., 2003. Exploitation of named entities in automatic text summarization for Swedish. 14<sup>th</sup> Nordic Conference on Computational Linguistics, Reykjavik, Iceland, 30-31 May.
- [5] Grishman R., Sundheim B. M., 1996. Message Understanding Conference – 6: A brief history. The 16<sup>th</sup> International Conference on Computational Linguistics, Copenhagen, Denmark, 5-9 August.
- [6] Black W. J., Rinaldi F., Mowatt D., 1998. FACILE: Description of the NE System Used for MUC-7. 7<sup>th</sup> Message Understanding Conference, Fairfax, Virginia, 29 April – 1 May.
- [7] Aone C., Halverson L., Hampton T., Ramos-Santacruz M., 1998. SRA: Description of the IE2 system used for MUC-7. 7<sup>th</sup> Message Understanding Conference, Fairfax, Virginia, 29 April – 1 May.
- [8] Nadeau D., Turney P. D., Matwin S., 2006. Unsupervised named-entity recognition: Generating gazetteers and resolving ambiguity. 19<sup>th</sup> Canadian Conference on Artificial Intelligence, Quebec, Canada, 7-9 June.
- [9] Özkaya S., Diri B., 2011. Named entity recognition by conditional random fields from Turkish informal texts. 19<sup>th</sup> Signal Processing and Communications Applications Conference, Antalya, 20-22 April.
- [10] Lin W., Ji D., Lu Y., 2017. Disorder recognition in clinical texts using multi-label structured SVM. BMC bioinformatics, **18**(1), 75, pp. 1-11.
- [11] Zhang M., Geng G., Chen J., 2020. Semi-Supervised Bidirectional Long Short-Term Memory and Conditional Random Fields Model for Named-Entity Recognition Using Embeddings from Language Models Representations. Entropy, **22**(2), pp. 252.
- [12] Zhu Q., Li X., Conesa A., Pereira C., 2018. GRAM-CNN: a deep learning approach with local context for named entity recognition in biomedical text. Bioinformatics, **34**(9), pp. 1547-1554.
- [13] Korvigo I., Holmatov M., Zaikovskii A., Skoblov M., 2018. Putting hands to rest: efficient deep CNN-RNN architecture for chemical named entity recognition with no hand-crafted rules. Journal of cheminformatics, **10**(1), pp. 1-10.
- [14] Li J., Sun A., Han J., Li C., 2020. A survey on deep learning for named entity recognition. IEEE Transactions on Knowledge and Data Engineering.
- [15] Chen Y., Zhou C., Li T., Wu H., Zhao X., Ye K., Liao J., 2019. Named entity recognition from Chinese adverse drug event reports with lexical feature based BiLSTM-CRF and tri-training. Journal of Biomedical Informatics, **96**, pp. 103252.
- [16] Leitner E., Rehm G., Moreno-Schneider J., 2019. Fine-grained Named Entity Recognition in Legal Documents. 15<sup>th</sup> International Conference on Semantic Systems, Karlsruhe, Germany, 9-12 September.
- [17] Leaman R., Wei C. H., Lu Z., 2015. tmChem: a high performance approach for chemical named entity recognition and normalization. Journal of cheminformatics, **7**(S1), S3.
- [18] Cucerzan S., Yarowsky D., 1999. Language independent named entity recognition combining morphological and contextual evidence. In 1999 joint SIGDAT conference on empirical methods in natural language processing and very large corpora.
- [19] Küçük D., 2009. Named entity recognition experiments on Turkish texts. In International

Conference on Flexible Query Answering Systems.  
Springer, Berlin, Heidelberg.

- [20] Cekinel R. F., Ağrımın M., Karagöz P., Yılmaz B., 2019. Named Entity Recognition with Conditional Random Fields on Turkish News Dataset: Revisiting the Features. 27<sup>th</sup> Signal Processing and Communications Applications Conference, Sivas, Turkey, 24-26 April.
- [21] Farmakiotou D., Karkaletsis V., Koutsias J., Sigletos G., Spyropoulos C. D., Stamatopoulos P., 2000. Rule-based named entity recognition for Greek financial texts. In Proceedings of the Workshop on Computational lexicography and Multimedia Dictionaries (COMLEX 2000).
- [22] Sheikh M., Conlon S., 2012. A rule-based system to extract financial information. *Journal of Computer Information Systems*, **52**(4), pp. 10-19.
- [23] Wang S., Xu R., Liu B., Gui L., Zhou Y., 2014. Financial named entity recognition based on conditional random fields and information entropy. In 2014 International Conference on Machine Learning and Cybernetics, Lanzhou, China, 13-16 July
- [24] Alvarado J. C. S., Verspoor K., Baldwin T., 2015. Domain adaptation of named entity recognition to support credit risk assessment. In Proceedings of the Australasian Language Technology Association Workshop 2015
- [25] Bayraktar O., Temizel T. T., 2008. Person name extraction from Turkish financial news text using local grammar-based approach. In 2008 23<sup>rd</sup> International Symposium on Computer and Information Sciences (pp. 1-4). IEEE.
- [26] Leitner E., Rehm G., Moreno-Schneider J., 2019. Fine-grained Named Entity Recognition in Legal Documents. In International Conference on Semantic Systems (pp. 272-287). Springer, Cham.
- [27] Vardhan H., Surana N., Tripathy B. K., 2020. Named-Entity Recognition for Legal Documents. In International Conference on Advanced Machine Learning Technologies and Applications (pp. 469-479), Jaipur, India. Springer, Singapore, 13-15 February.



Kocaeli University

## Kocaeli Journal of Science and Engineering

<http://dergipark.org.tr/kojose>**Engineering Geological Investigation of the Kırık Tunnel Route**Özgür Fatih ÇÜMEN<sup>1</sup>, Ahmet KARAKAŞ<sup>2,\*</sup><sup>1</sup> Department of Geological Engineering, Kocaeli University, Kocaeli, 41001, Turkey, **ORCID:** 0000-0002-8184-3776<sup>2</sup> Department of Geological Engineering, Kocaeli University, Kocaeli, 41001, Turkey, **ORCID:** 0000-0002-4672-2063**Article Info****Abstract****Research paper**

Received : March 29, 2021

Accepted : May 20, 2021

**Keywords**

Kırık Tunnel

NATM

Rock Class

Tunnel Support

Engineering structures are of great importance in the comfort and safe travel of people who prefer the highway in the existing transportation networks. Highway tunnels are one of the most important engineering structures that easily overcome transportation problems. This study investigates the geological and geotechnical structures of the Kırık tunnel on the Erzurum-Rize highway route, makes the rock mass classification required for tunnel excavation according to the New Austrian Tunneling Method and determines the tunnel support systems. Geological mapping, drillings, geological- geotechnical investigation based on in-situ and laboratory tests were carried out in order to reveal the physical and mechanical properties of the geological formations on the tunnel and to determine the basic data required by the project. It is divided into 4 classes on the basis of NATM Rock Classification along the tunnel axis. Rock support types related to rock classes defined as B1, B2, B3 and C2.

**1. Introduction**

On the Erzurum-Rize highway which is the main artery on the north-southeast axis in our country's road network, the passages connecting the Black Sea to Eastern Anatolia increase in the winter months due to the heavy snowfall of the road and the high tourism potential of Black Sea Region in the summer. By building a tunnel (Kırık tunnel) in sections where snowfall, icing and heavy snow are intense, the current Erzurum- Rize highway transportation is made safer for drivers.

The Kırık Tunnel is expected to contribute to the trade and tourism of the country as well as the convenience of transportation, by increasing the existing highway standard. Since the transportation between the Rize-Erzurum highway is reduced to 2 hours after the tunnel is opened for transportation, it is also aimed to facilitate the access of tourists from Black Sea to Erzurum, especially in winter for skiing.

The route had to be improved due to the frequent closure of the working area in winter due to snow and its type, and the high cost of maintenance and repair work for the road pavement that deteriorated due to freeze-thaw effects. For this reason, with the construction of the Kırık Tunnel, the use of this corridor more frequently and especially in the winter months and in the Kırık Tunnel, which is opened to increase the road standards between Erzurum and İspir, to examine the geological and geotechnical setting required for the tunnel and to classify the rock mass required for tunnel excavation. The geological and geotechnical model of the tunnel was created by correlating the geological unit and tunnel section profiles of the tunnel route. Rock mass rating (RMR), NGI Rock Tunnel quality index (Q system) and Geological Strength Index (GSI) rock mass classification systems according to New Austrian Tunneling Method) and tunnel support systems were determined.

**2. Study Area**

The study area is located on the Erzurum-Pazaryolu-İspir highway between Erzurum and İspir and is

\* Corresponding Author: ahmet.karakas@kocaeli.edu.tr



approximately 90 km away from Erzurum province. The Kırık tunnel is located on 1/25000 scale H45-b3 and H45-b2 map sheets (Figure 1). The tunnel on the route of the study area enters at Km: 64 + 730.00 and 2043.905 m elevations. Tunnel at Km: 71 + 826.00 (Right Line), Km: 71 + 843.00 (Left Line) and 1706.950m elevation, the tunnel is designed to be in line with the geometry of the road on which it is located, with two lanes in two separate tubes. The shortening of 33 km and its deactivation of the Gölyurt Pass with an altitude of 2,380 meters, which

became a nightmare for travelers especially in the winter months, has become even more important with the opening of the Ovit Tunnel. Tunnel entrance Km: 64 + 730.00 and tunnel exit Km: 71 + 826.00 (Right Line) / Km: 71 + 843.00 (Left Line) and the tunnel length is 7096 meters for the right line and 7113 meters for the left line. Tunnel entrance is at 2043,905 m elevation and exit is at 1706,950 m elevation and the elevation difference is 336.955 meters. Each of the tunnels has two lanes with 8.0 meter height and 5.0 meter width.

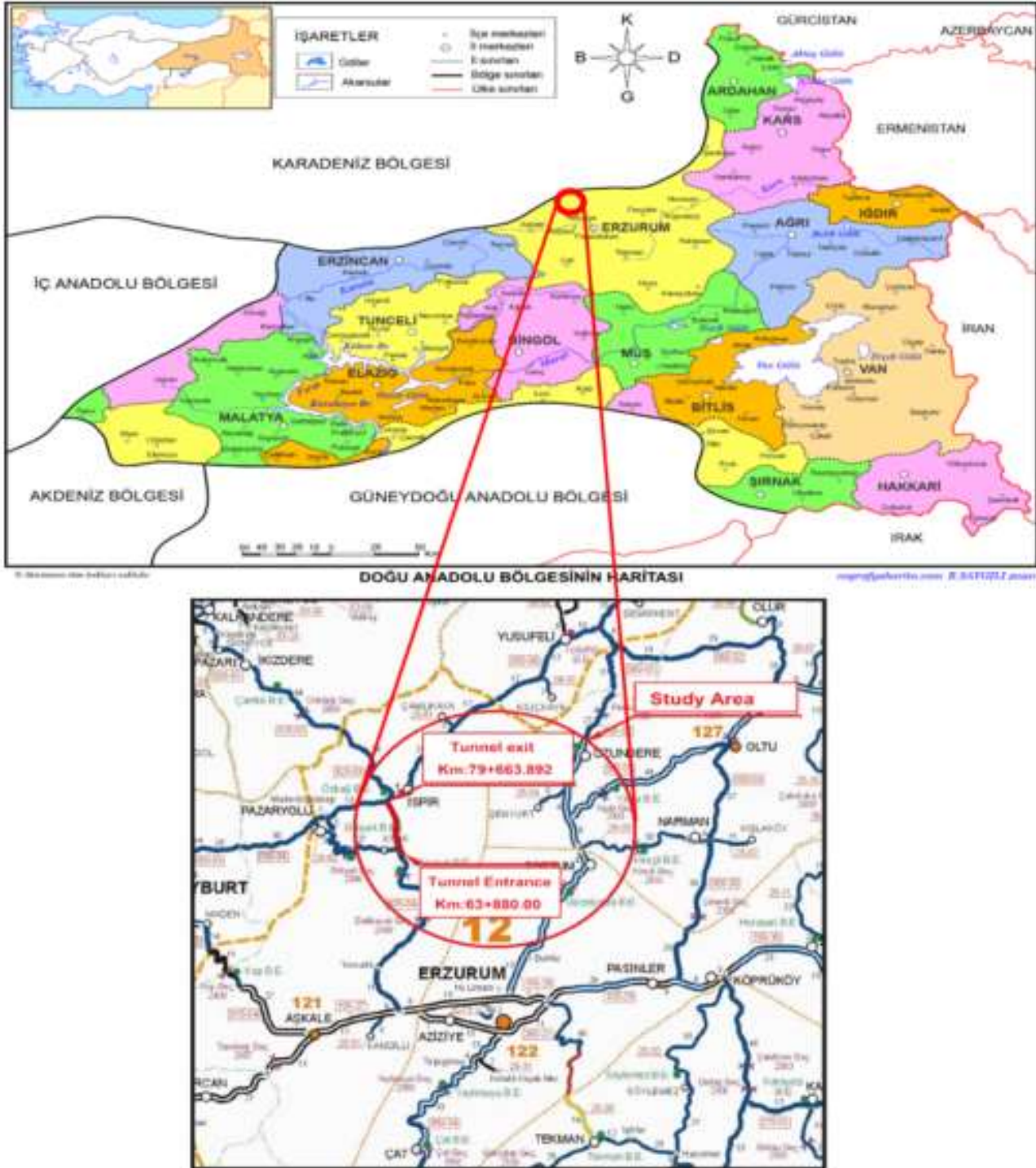


Figure 1. Study area location map

### 3. Geology of the Study Area

The formation and units seen in the tunnel route and its vicinity are from old to young. Karagüney formation consists of Jurassic-Cretaceous sandstone, sandy limestone, laminated chert and brecciated limestones at the bottom. The Hatungüney formation consisting of turbiditic sandstone, clayey limestone and limestones starts with clayey limestones, sandstones overlying the formation and formation consisting of conglomerate, sandstone, limestone alternation and clayey limestones. The Mescitdağları formation consisting of the alternation of Tertiary aged andesitic-basaltic rocks, agglomerate, tuff, tuffite, and volcanic of sandstone and mudstone is formed on these units [1]. Finally, Quaternary alluvium and slope debris overlies unconformably. Geology map of the study area is shown in Figure 2 (adapted from MTA 2002).

### 4. Tectonic Setting and Structural Geology of the Study Area

The Eastern Anatolia region, including the study area, has been under the control of the N-S oriented compressional stress since Late Cretaceous [2].

As the Neo-Tethys northern branch began to close in Late Cretaceous, the large ophiolite nappes were emplaced in the Senonian on the Anatolide / Tauride platform from this branch to the south. Before Late Eocene, with the collision of the Anatolide / Tauride platform and the Pontide island arc, the Eocene - Oligocene asymmetric flysch / molasse basins developed in front of the ophiolitic nappes advancing towards the south in the Eastern Anatolia Region [3].

In the Neotectonic period, as a result of compression in the region, high angle thrusts with EW strike or N dips, NW - SW trending left strike-slip faults, NW - SE striking right strike-slip faults, N - S striking tension cracks and widespread volcanic rocks emerging from these cracks have been formed [4].

During Late Miocene - Early Pliocene, the continental-continental collision between the Eurasian and Arabian plates caused the formation of a large number of left and right lateral faults, especially within the Eurasian plate. As is known, two of these faults of regional dimension are right-lateral North Anatolian and left-lateral East Anatolian faults [5].

The study area covers tectonic structures developed in compressional stress control since Late Cretaceous. An ophiolitic mixed Late Maestrichtian transgressive marine sequence that forms the basement in this area

unconformably overlies [6]. This indicates that the first emplacement age of the ophiolite unit in the study area and its vicinity is pre-Late Maestrichtian. In the study area under the control of N - S directional compressive stress, approximately E-W trending thrust and large angle reverse faults, NE-SW trending left lateral and NW-SE trending right lateral strike-slip faults and approximately E-W axis trending folds were developed.

These tectonostratigraphic units with their NE - SW extensions in the study area and its immediate surroundings and which are defined as tectonostratigraphic units since they have different stratigraphic sequences, are in autochthonous or allochthonous positions according to their relative movements. Allochthonous units, which form a above each other structure by pushing on the autochthonous or another allochthonous slice along low angle thrust planes from these slices which are tectonically related with each other, have been distinguished in the style of "nap" masses in order to to express these features more clearly [7]. All of the faults determined in the study area are reverse faults and are seen intensely in the region between the tunnel exit and the end of the line.

### 5. Materials and Methods

Preliminary investigation studies have become an important issue within the scope of engineering geology studies to be carried out on the tunnel route. It is necessary to collect all necessary materials related to the field of study and its subject. In the field observations made on the tunnel route, slope debris derived from tuffite, carbonated siltstone and clayey limestone units was observed in the entrance the portal. The slope debris is completely weathered and the pebbles in the slope debris unit are of claystone origin. In the exit portal, there are units of clayey limestone origin in the slope debris and completely decomposed from the slope debris. In order to determine the problems that the rock masses in the study area may experience during tunnel boring, the status of the layers and discontinuities was tried to be determined. From the samples taken during the drilling studies, soil and rock coring samples were taken from in-situ test to detail the geological-geotechnical geological units on the tunnel route and to determine the engineering properties of the units in this section. In order to determine the index and engineering properties of the soil on it; Natural water content, Atterberg limits (liquid limit, plastic limit), plasticity index, grain size distribution (sieve analysis) tests were carried out.

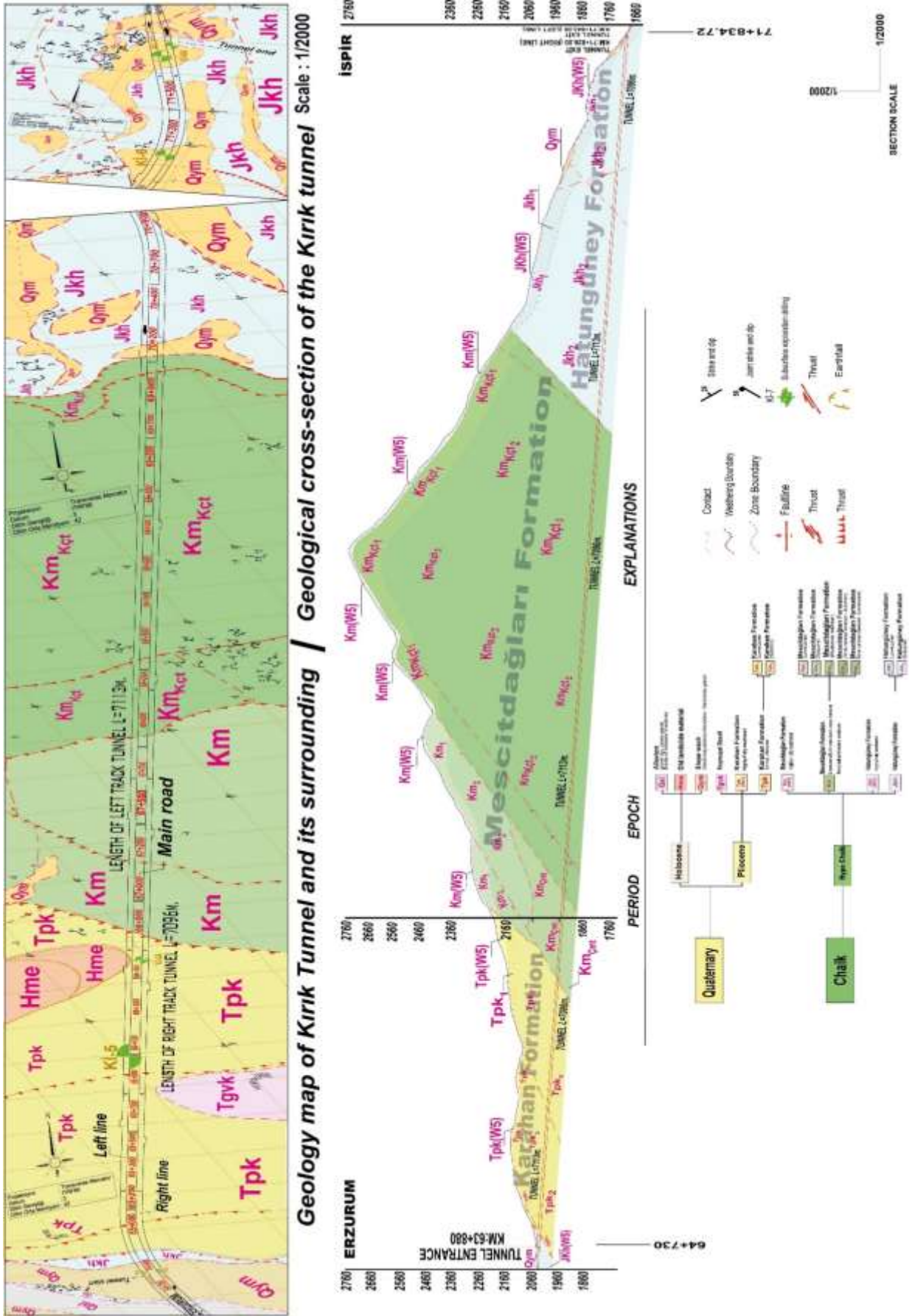


Figure 2. Geology map and cross section of Kırık tunnel alignment and its surrounding

In addition, to determine the basic parameters for tunnel design, rock mechanics tests were carried out from rock-specific units and the natural unit weight, uniaxial and triaxial compression tests in the rock were performed to reveal the mechanical and physical properties of the rock units. As a result, compressive strength, modulus of elasticity, poisson ratio values were determined.

In order to make the tunnel excavations safe, the geological units should be evaluated and support systems suitable for the excavation should be made according to the result of this assessment. While tunnel excavations can be done differently, different tunnelling methods have been developed depending on the way it is opened. Depending on the tunneling methods developed, it is important that the tunnel opening in the planned location can safely stay in the excavated area with support and maintain its purpose-based function. Tunnel excavations today can be excavated by using mechanical machinery and drilling-blasting method. Mechanical excavations are carried out by hydraulic breakers, arm tunnel boring machines, shielded machines, micro tunnel boring machines and various TBM (Tunnel Boring Machine) methods. The last method applied in the field of tunneling is NATM. NATM method is a method developed by taking advantage of the stability of the rock to hold itself.

The main purpose of NATM, which is opened without the use of a specific equipment, is to transform the environment surrounding the tunnel into a self-holding static system by controlling and directing the secondary stresses and deformations that will occur after the first excavation and consolidation [8].

Shotcrete, mesh steel, rock bolts and steel mesh, which are used as primary supports in NATM, form a composite structure together with the rock mass. This composite system, consisting of rock and support elements, provides the redistribution of the pressures around the tunnel, increasing the strength of the rock, which decreases as a result of loosening. Deformations occur in a controlled manner without collapsing or creating an unsafe environment in the tunnel [9].

As a result of the studies, suggestions were made for excavation and support systems with the help of the RMR, Q and NATM classification systems of the geological units on the route with the help of engineering geology data on the tunnel route.

## 6. Results and Discussion

The tunnel route is opened within the Late Jurassic Karagüney formation, Akçağıl formation and Lower Cretaceous Hatungüney formation, Mescitdağları formation and Quaternary Karahan formation and slope

debris. The tunnel route is divided into 24 different zones (Structural zone) depending on the layer locations of the geological units, the cover height, the portal structures and the structural features of the tunnel route (Table 1).

**Table 1.** Dividing the tunnel route into structural zones

KM	Formation	Lithology	Meter
64+730-64+825	Hatungüney Formation	JKh (W5) / JKh <sub>1</sub>	95
64+825-64+945	Karahana Formation	Tpk <sub>1</sub>	120
64+945-65+480		Tpk <sub>2</sub>	535
65+480-65+590		Tpk <sub>2</sub>	110
65+590-66+250	Mescitdağları Formation	Tpk <sub>2</sub>	660
66+250-66+380		Kmçmt	130
66+380-66+780		Kmçmt	400
66+780-66+850		Kmçkt2	70
66+850-66+860	Fault Zone	Kmçkt2	10
66+860-66+870	Fault Zone	Kmçkt2	10
66+870-67+080	Mescitdağları Formation	Kmçkt2	210
67+080-67+150		Kmçkt2	70
67+150-69+540		Kmçkt2	2390
69+540-69+550	Fault Zone	Kmçkt2	10
69+550-69+630	Hatungüney Formation	JKh <sub>2</sub>	80
69+630-69+640	Fault Zone	JKh <sub>2</sub>	10
69+640-70+750	Hatungüney Formation	JKh <sub>2</sub>	1110
70+750-70+760	Fault Zone	JKh <sub>2</sub>	10
70+760-70+850	Hatungüney Formation	JKh <sub>2</sub>	90
70+850-71+070		JKh <sub>2</sub>	229
71+070-71+600		JKh <sub>2</sub>	530
71+600-71+720		JKh <sub>2</sub>	120
71+720-71+760		JKh <sub>2</sub>	40
71+760-71+834.72		JKh <sub>1</sub>	74,72

Geological and geotechnical research studies were conducted to determine the ground conditions of Km: 63 + 880.00 - 71 + 834.72 of the proposed route belonging to the Kırık tunnel in the study area. Engineering geology mapping consists of foundation drilling and in – situ test, research and laboratory test.

A total of 728 meters of foundation drilling has been completed in 7 locations in order to detail the rock units in terms of geological and geotechnical aspects, determine the engineering characteristics of the units located in this section and determine the groundwater level, observed along the tunnel.

Pressiometer tests were carried out in the study area in order to determine the deformation properties of the soil and rock units observed in the foundation drillings. LouisMenard GA type pressiometer and 60 mm N type probe were used in the tests. For each drill, the variation of the deformation modulus (Em) and the limit (Pln) and net limit (PL\*) pressures along the depth were determined. The deformation modulus values were found as 38 kg/cm<sup>2</sup> in minimum carbonated siltstones and 5186 kg/cm<sup>2</sup> in units with sandstone-clayey limestone-micrite alternation.

In order to determine the point load strength index value (Is<sub>50</sub>) of the rock units in the study area, a point



loading test was performed on the samples taken from the Kİ-5 and Kİ-6 boreholes. The test instrument consisting of loading system (loading body, loading pump and two conical ends), load indicator and measuring systems measuring the distance between conical ends are used. It is based on the principle of breaking the rock sample placed between two conical ends. As a result of the test performed on the samples the average point load strength index ( $I_{S50}$ ) of the claystone unit is in the range of 0.41- 1.82 MPa, and the point load strength index of limestones ( $I_{S50}$ ) is in the range of 11.44 - 14.14 MPa.

In order to determine the permeability of rock units constituting the tunnel floor, "Pressurized Water Tests (BST)" were carried out in the Kİ-5 and Kİ-6 boreholes. The test results calculated as "Lugeon" were shown in Table 2.

**Table 2.** Summary of pressurized water test results obtained in the study area

Drilling Number	-Lugeon Values	Depth (m)	Lugeon classification	Units passed
Kİ-5		122.00-126.00		Karahan Formation
Kİ-5	0.20	127.00-130.00	Impermeable	Karahan Formation
Kİ-5		132.00-135.00		Karahan Formation
Kİ-5	0.20	137.00-140.00	Impermeable	Karahan Formation
Kİ-5	0.47	148.00-150.00	Impermeable	Karahan Formation
Kİ-6	11.68	152.00-154.00	Permeable	Hatungüney Formation
Kİ-6	0.10	157.00-159.00	Impermeable	Hatungüney Formation
Kİ-6	1.42	162.00-164.00	Low Permeable	Mescitdağları Formation
Kİ-6	2.01	167.00-169.00	Low Permeable	Mescitdağları Formation
Kİ-6	3.45	172.00-174.00	Low Permeable	Mescitdağları Formation

It has been determined that the tunnel section and its immediate surroundings include slope debris (Qym), Karahan formation (Tpk), Mescitdağları formation (Km), Mescitdağları formation mudstone member ( $K_{m\text{çmt}}$ ) and Hatungüney (Jkh) formation.

Karahan formation (Tpk) in general consists of claystone and sandstone units. The claystone unit is gray - greenish gray, little - medium hard, medium weak, locally weak, moderately weathered in places. Marine shells are distinguished in the unit and certain levels are completely weathered. The sandstone unit is green - greenish gray, friable - slightly hard, medium weak, moderately weathered and fine grained. The highly weathered level (Tpk / W5) of this unit is generally represented by a yellowish brown, pebbly sandy clay unit. It is moist-dry, plasticity-free, low-medium hard, angular, intense claystone / siltstone origin, with limestone origin blocks in places.

Mudstone member of Mescitdağları formation ( $K_{m\text{çmt}}$ ), consists of mudstone and breccia. The mudstone

member is generally red - burgundy -like - greenish colored, slightly hard - moderately hard, moderately weak - weak in places, moderately - severely weathered in places. Discontinuities cannot be traced due to segregation. The mudstone member of the Mescitdağları formation ( $K_{m\text{çmt}}$ ) has generally impermeable - less permeable properties in terms of groundwater.

In general, Hatungüney formation (JKh), observed in the entrance and exit sections of the tunnel route and in a large part of the project route, consists of the intercalation of limestone, claystone, tuff, sandstone and clayey limestone. Limestone and clayey limestone unit in general; beige and gray colored, hard, medium resistant, slightly weathered. Discontinuities are in the range of  $10^\circ - 90^\circ$  rough, dense - very dense, segmented and FeO colored. The claystone unit is beige-off-white colored, hard-medium hard, medium weak, slightly weathered. Discontinuities are  $10^\circ - 30^\circ$  open, rough, dense - very dense, FeO colored,  $0^\circ - 90^\circ$  closed and very dense. grayish dark brown, friable - slightly hard, weak - very weak, very - completely weathered.

Sandstones, medium hard with hard, medium weak, moderately weathered; Consists of friable - less hard, weakly weathered clayey limestones and medium hard - medium strength, slightly - moderately weathered limestones. Very - completely weathered level (JKh / W5) of this unit is silty sandy gravel and sandy gravel. The results of the laboratory tests performed on the SPT samples obtained from this level determined that they were GM, GP - GM, SC, SM, GP according to the Unified Soil Classification System.

The safe and economical underground excavations is directly proportional to the envisaged rock classification and related in tunnel support design. In today's modern in tunneling, the rock classifications, which are the basis for projecting, take into account the mass features of the rock. In this context, there are 3 important rock classifications in the main rock mass classifications developed and widely used in underground excavations in many different countries.

These classifications are; Rock Quality Index (Q) is the Geomechanical Classification of Jointed Rock Masses (RMR) and the Geological Strength Index (GSI) [12].

In the Q-classification, the Q-value takes values between 0.001 and 1000, covering the range between the worst rock condition and the perfect rock. Similarly, the RMR classification based on a score system ranging from 0-100 defines 5 rock classes from very good to very bad. In the GSI classification, it is expressed numerically in 25 categories ( $5 \times 5$ ), 5 depending on the structural characteristics of the rock mass, and 5 in terms of the state of the cracks and the degree of weathering (depending on the discontinuity surface).

GSI classification is preferred over RMR classification, especially in terms of engineering evaluations, due to its applicability to worst to best rock condition. GSI, which was initially associated with RMR and Q classification scores, has been used as a stand-alone classification system after 1999 with changes made in later years [10].

In the application of the RMR system, the rock mass in the study area is divided into structural sub-units and after determining the numerical values corresponding to each parameter separately according to the specific characteristics of the rock in the units, the total number of values is found and this number obtained is corrected according to the location of the discontinuities. The corrected total number is defined as the RMR rock mass number. RMR classification, the support type for each rock class, the cohesion of the tunnel rock and the internal friction angle, and the average standstill time can be predicted. RMR classification system was calculated according to [11], and rock classification was given according to the general result value for the rock units to be passed at the level of each different structural zoning tunnel separated due to different geological conditions along the route of the tunnel (Table 3).

**Table 3.** RMR classification system for tunnel route

Km	Drilling Number	Geological Unit	Rock Strength	RQD	Joint Frequency	Joint Status	Inclusion Level	Correction	RMR	Rock Class
54+730-64+825	KI-3 KI-4	JKh/WG JKh	1	3	5	11	7	-10	17	Poor
54+825-64+945	-	Tpk <sub>1</sub>	2	8	5	13	7	-5	30	Poor
54+945-65+480	-	Tpk <sub>1</sub>	2	13	8	16	7	-5	41	Fair
55+480-65+590	-	Tpk <sub>1</sub>	2	3	5	9	7	-5	21	Poor
55+590-66+250	KI-5	Tpk <sub>2</sub>	2	13	8	16	7	-5	41	Fair
56+250-66+380	-	Km <sub>100</sub>	2	3	5	9	7	-5	21	Poor
56+380-66+780	KI-5A	Km <sub>100</sub>	4	8	8	12	6	-10	35	Poor
56+780-66+800	-	Km <sub>100</sub>	2	3	5	9	7	-5	21	Poor
56+800-67+080	-	Km <sub>100</sub>	7	17	10	23	7	-5	59	Fair
57+080-67+100	-	Km <sub>100</sub>	7	13	10	21	6	-5	50	Fair
57+100-68+500	-	Km <sub>100</sub>	12	17	10	23	7	-5	64	Good
58+500-68+630	-	JKh <sub>2</sub>	2	8	8	13	4	-5	30	Poor
58+630-70+700	-	JKh <sub>2</sub>	12	13	10	23	7	-5	60	Good
70+700-70+850	-	JKh <sub>2</sub>	2	8	8	13	4	-5	30	Poor
70+850-71+070	-	JKh <sub>2</sub>	7	13	10	18	7	-5	50	Fair
71+070-71+600	KI-8	JKh <sub>2</sub>	12	13	10	21	7	-5	59	Fair
71+600-71+720	KI-8A	JKh <sub>2</sub>	7	13	8	18	7	-5	48	Fair
71+720-71+780	KI-8A	JKh <sub>2</sub>	4	8	8	16	4	-5	30	Poor
71+780-71+834.72	KI-7	JKh <sub>1</sub>	2	3	5	14	4	-10	19	Poor
56+850-66+880	KI-5A	Fault Zone	2	13	8	16	7	-5	41	Fair
56+880-66+870	-	Fault Zone	7	13	10	21	4	-5	50	Fair
58+540-68+500	-	Fault Zone	7	13	10	18	7	-5	50	Fair
59+630-69+640	-	Fault Zone	7	13	8	18	7	-5	48	Fair
70+750-70+760	-	Fault Zone	7	13	8	18	7	-5	48	Fair

In the application of the Q system, the rock mass classification of the geological units in the tunnel opening was defined by the Q or NGI (Norwegian Geotechnical Institute) system. (1) Rock tunneling quality (Q) is calculated from the following expression as a function of 6 parameters independent of each other [10].

$$Q = \frac{RQD}{J_n} \cdot \frac{J_r}{J_a} \cdot \frac{J_w}{SRF} \tag{1}$$

(RQD / J<sub>n</sub>) value; block size or size of the rock formed by different joint set, (J<sub>r</sub> / J<sub>a</sub>) value defines the roughness and friction between the joint surfaces and the filling material (shear strength between the blocks), (J<sub>w</sub> / SRF) value indicates the effective stress (Table 4).

**Table 4.** Q classification system of the tunnel route

Km	Drilling Number	Unit	RQD	J <sub>n</sub>	J <sub>r</sub>	J <sub>a</sub>	J <sub>w</sub>	SRF	Q	Rock Class
64+730-64+825	KI-3 KI-4	JKh/WG JKh	20 (1A)	2x12 (2G)	1 (3E)	3 (4C)	0.66 (5B)	10 (6B)	0.016	Extremely poor
64+825-64+945	-	Tpk <sub>1</sub>	33 (1A)	12 (2G)	1.5 (3D)	3 (4C)	0.66 (5B)	5.0 (6B)	0.162	Very poor
64+945-65+480	-	Tpk <sub>1</sub>	50 (1C)	12 (2G)	1.5 (3D)	2 (4C)	0.66 (5B)	2.5 (6C)	0.825	Very poor
65+480-65+590	-	Tpk <sub>2</sub>	20 (1A)	12 (2G)	1.5 (3D)	6 (4K)	0.66 (5B)	5.0 (6C)	0.035	Extremely poor
65+590-66+250	KI-5	Tpk <sub>2</sub>	70 (1C)	12 (2G)	1.5 (3D)	1 (4B)	0.66 (5B)	7.5 (6D)	0.770	Very poor
66+250-66+380	-	Km <sub>100</sub>	20 (1A)	12 (2G)	1.5 (3D)	6 (4K)	0.66 (5B)	5.0 (6C)	0.026	Extremely poor
66+380-66+780	KI-5A	Km <sub>100</sub>	35 (1A)	12 (2G)	1.5 (3D)	3 (4C)	0.66 (5B)	10.0 (6A)	0.086	Extremely poor
66+780-66+850	-	Km <sub>100</sub>	20 (1A)	12 (2G)	1.5 (3D)	6 (4K)	0.66 (5B)	5.0 (6C)	0.059	Extremely poor
66+850-67+080	-	Km <sub>100</sub>	80 (1D)	12 (2G)	1.5 (3D)	1 (4B)	0.66 (5B)	1.0 (6A)	6.900	Fair
67+080-67+150	-	Km <sub>100</sub>	70 (1C)	12 (2G)	1.5 (3D)	3 (4C)	0.66 (5B)	10.0 (6A)	1.925	Poor
67+150-69+550	-	Km <sub>100</sub>	85 (1D)	12 (2G)	1.5 (3E)	1 (4B)	0.5 (5C)	1.0 (6A)	5.311	Fair
69+550-69+630	-	JKh <sub>2</sub>	25 (1B)	12 (2G)	1.5 (3E)	3 (4D)	0.66 (5B)	2.5 (6F)	0.275	Very poor
69+630-70+760	-	JKh <sub>2</sub>	70 (1C)	12 (2G)	1.5 (3E)	1 (4A)	0.66 (5B)	1.0 (6A)	5.770	Fair
70+760-70+850	-	JKh <sub>2</sub>	35 (1B)	12 (2G)	1.5 (3E)	6 (4K)	0.66 (5B)	2.5 (6C)	0.193	Very poor
70+850-71+070	-	JKh <sub>2</sub>	55 (1C)	12 (2G)	1.5 (3E)	1 (4B)	0.66 (5B)	2.5 (6C)	1.810	Poor
71+070-71+600	KI-6	JKh <sub>2</sub>	65 (1C)	12 (2G)	1.5 (3E)	1 (4A)	0.66 (5B)	1.0 (6A)	5.363	Fair
71+600-71+720	KI-6A	JKh <sub>2</sub>	60 (1C)	12 (2G)	1.5 (3E)	1 (4B)	0.66 (5B)	2.5 (6F)	1.980	Poor
71+720-71+780	KI-6A	JKh <sub>2</sub>	30 (1B)	12 (2G)	1.5 (3E)	2 (4C)	0.66 (5B)	5.0 (6E)	0.248	Very poor
71+780-71+834.72	KI-7	JKh <sub>1</sub>	20 (1A)	12x2 (2G)	1.5 (3E)	3 (4C)	0.66 (5B)	5.0 (6E)	0.065	Extremely poor
66+850-66+880	KI-5A	Fault Zone	70 (1C)	12 (2G)	1.5 (3D)	1 (4B)	0.66 (5B)	7.5 (6D)	0.770	Very poor
66+880-66+870	-	Fault Zone	70 (1C)	12 (2G)	1.5 (3D)	3 (4C)	0.66 (5B)	1.0 (6A)	1.925	Poor
69+540-69+550	-	Fault Zone	55 (1C)	12 (2G)	1.5 (3E)	1 (4B)	0.66 (5B)	2.5 (6F)	1.815	Poor
69+630-69+640	-	Fault Zone	60 (1C)	12 (2G)	1.5 (3E)	1 (4B)	0.66 (5B)	2.5 (6F)	1.980	Poor
70+750-70+760	-	Fault Zone	60 (1C)	12 (2G)	1.5 (3E)	1 (4B)	0.66 (5B)	2.5 (6F)	1.980	Poor

The geotechnical properties of the geological units on the tunnel route evaluated in terms of engineering geology are given in the table below (Table 5).

**Table 5.** Geotechnical characteristics of the geological units on the tunnel route

Model Km	Geological Unit	C (kPa)	φ (°)	γ (kN/m <sup>3</sup> )	E (MPa)
64+762	Qym	10	33	20	15
	Jkh / W5	19	32	21	35
	Jkb <sub>1</sub>	88	50	25	640
64+980	Tpk / W5	16	28	22	15
	Tpk <sub>1</sub>	47	35	23	70
	Tpk <sub>2</sub>	260	52	24	2170
66+240	Tpk / W5	11	33	22	15
	Tpk <sub>1</sub>	39	37	23	70
	Tpk <sub>2</sub>	618	41	24	2170
66+780	Km / W5	15	39	20	30
	Km <sub>1</sub>	70	29	22	170
	Km <sub>2</sub>	280	30	23	700
	Km <sub>Qant</sub>	960	38	25	4000
68+880	Km / W5	20	34	20	30
	Km <sub>Qc1</sub>	463	47	25	7330
	Km <sub>Qc2</sub>	4698	44	27	33000
69+640	Km / W5	13	39	20	30
	Km <sub>Qc1</sub>	404	49	25	7330
	Km <sub>Qc2</sub>	3500	53	27	45100
	Jkb <sub>1</sub>	2951	47	26	18100
70+850	Jkh / W5	12	37	21	35
	Jkb <sub>1</sub>	131	45	25	640
	Jkb <sub>2</sub>	2141	52	26	18100
71+620	Jkh / W5	12	37	21	35
	Jkb <sub>1</sub>	143	44	25	640
	Jkb <sub>2</sub>	1635	57	26	18100
71+721	Qym	10	33	20	15
	Jkb <sub>1</sub>	131	45	25	640
	Jkb <sub>2</sub>	1778	61	26	25600
71+780	Qym	10	33	20	15
	Jkb <sub>1</sub>	131	45	25	640

Rock masses with different geomechanical properties forming the ground profile of the tunnel route were evaluated based on Q and RMR rock classifications and the tunnel rock conditions were divided into 4 classes on the basis of NATM Rock Classification. The rock classes defined as B1, B2, B3 and C2 [13] were approximately 60%, 6% of the tunnel, respectively. Represents 20% and 14%. For the tunnel route where rock classification was made, the tunnel support systems were determined depending on the rock classes and rock classification.

The intervals of tunnel: Km: 66 + 870 - 67 + 080, Km: 67 + 150 - 69 + 540, Km: 69 + 640 - 70 + 750, Km: 71 + 070 - 71 + 600 were determined as B1 rock class within the Mescitdağları formation and the Hatungüney formation (JKh) As a result of the evaluation of rock conditions, The "B1" support type recommended for these sections is established from the following support

elements.

Proposed support and excavation stages of support types were determined according to Q and RMR rock classification with mixed elements method.

- Shotcrete (ds = 100 mm)
- Wire mesh (1 layer), (Q221/221)
- Systematic bolt (L = 4.00 meter long, 2.00 x 2.00 meter spacing Φ28mm PG - bolt)

In B1 rock mass defined as "brittle", the deformations are small and decrease very rapidly. The loosening of the rock caused by blasting and the low strength of the rock mass cause dismantling of the tunnel ceiling and the upper part of the side walls. Systematic bracing is required in limited areas in this rock class, and the implementation of the bracing outlined above is recommended.

The intervals of tunnel: Km: 67 + 080 - 67 + 150, Km: 70 + 850 - 71 + 070 and Km: 71 + 600 - 71 + 720 were determined as B2 rock class within the Mescitdağları formation and Hatungüney formation. As a result of the evaluation of rock conditions, "B2" support type recommended for these sections is established from the following support elements.

- Shotcrete (ds = 150 mm)
- Wire mesh (1 layer), (Q221/221)
- Systematic bolt (L = 4.00 meter long, 2.00 x 2.00 meter spacing Φ28mm PG - bolt)
- Continuing with 1.5 " injection when necessary

In B2 rock mass defined as "very brittle", if the support is done in time, the deformations decrease rapidly. If the support is not done in time or is not sufficient, there may be loosening and related ruptures in the B2 rock mass at the depths. It is recommended to apply the bracing outlined above on the tunnel ceiling, side walls and tunnel face to ensure stability.

The tunnel route designated as B3 rock class, for the tunnel Km: 64 + 945 - 65 + 480, Km: 65 + 590 - 66 + 250, Km: 69 + 550 - 69 + 630, Km: 70 + 760 - 70 + 850, and Km : 71 + 720 - 71 + 760 intervals formed within Karahan formation (Tpk), Mescitdağları formation (Km) and Hatungüney formation (JKh). The components of the "B3" support type suggested for these sections as a result of the evaluation of rock conditions are explained below.

- Excavation progress length maximum 1.25 - 1.50 m in the upper half and maximum 3.00 m in the lower half.
- The surface is covered with 2 cm shotcrete.
- Injected driving pipes are driven in every two shots.
- Steel mesh is placed Q589/221 tip
- Steel shoring is placed (NPI 140)
- Shotcrete thickness is completed to 13 cm.
- Second row steel mesh is placed Q589/221 tip
- Shotcrete is completed to 15 cm.
- Φ28mm PG bolts are placed

In the excavations made in B3 rock class, overbreak occurred in the rock mass. Fractured and weak rock with low cohesion created stability problems.

The intervals of the tunnel: Km: 64 + 730 - 64 + 945, Km: 65 + 480 - 65 + 590, Km: 66 + 250 - 66 + 850, Km: 71 + 760 - 71 + 834.72 were determined as C2 rock class within the Karahan formation (Tpk), Mescitdağları formation (Km) and the Hatungüney formation (JKh). As a result of the evaluation of rock conditions, the components of the "C2" support type suggested for these sections are explained below.

- Excavation progress length is maximum 1.00 m in the upper half, maximum 2.00 m in the lower half, 3.00 m in the base.

- Shotcrete (ds = 250 mm), The surface face covered with 3 cm shotcrete.

- Injected driving pipes are driven in every two shots.

- Steel mesh is placed Q589/221 tip

- Steel shoring will be placed (NPI 160)

- Sprayed concrete thickness is completed to 21 cm

- Second row steel mesh will be placed Q589/221 tip

- It will be covered with 4 cm more shotcrete and completed to a total of 25 cm.

- $\Phi$ 28mm PG bolts are placed

- Base arch concrete

In terms of rock mass behavior, the C2 support class consists mainly of rocks disturbed by fault zones in the NATM standard. Even in split excavations (upper half - six half excavations), spillages occur in the rock mass. Less cohesion and less cementing cause insufficient stability of the the area to be excavated.

## 7. Conclusions

The Kırık tunnel is a double-tube road tunnel on the Erzurum- İspir (D925) state road at Km: 64 + 730.00- 71 + 826.00 (Right) / 71 + 843.00 (Left) of the main road project route. Geological mapping, foundation drillings, geological- geotechnical research based on in-situ and laboratory test were carried out in order to reveal the physical and mechanical properties of the geological formations on the tunnel passage route of the tunnel under construction, and to determine the data. Although units belonging to three different formations are passed along the designed tunnel passage on the surface, it is predicted that Mescitdağları formation can be seen mostly at the tunnel elevation. On the tunnel route the transition, no geological geotechnical negativity was encountered in large dimensions (landslide, liquefaction, settlement, etc.). Engineering geology definitions, drilling data and rock mechanics test results of the rocks, constituting the basis of rock classification and defined by kilometer intervals throughout the tunnel passage, have been evaluated and

interpreted. In line with the engineering geology definition, the rock masses likely to be encountered at on the tunnel route were evaluated according to the Q and RMR Rock Classifications. It is divided into 4 classes on the basis of NATM Rock Classification along the tunnel pass. Rock support types related to rock classes defined as B1, B2, B3 and C2 have been proposed. The tunnel front support design was carried out as a result of the engineering geology definitions and rock classifications of the rocks along the tunnel route. Rock conditions indicate that tunnel excavation is generally appropriate to be done in the form of upper half / lower half. In addition, drilling-blasting method in the tunnel should be applied in sections with appropriate rock classification. In order to contribute to the safe and economical construction of the tunnel, it is necessary to determine possible stability problems, produce solution suggestions, and prepare a perimetric map of the tunnel in order to re-evaluate the rock class and support types foreseen in the project during excavation. Weak parts of the tunnel be built in C2 class, depending on the unfavorable geological conditions that could be encountered in faulted zones. Engineering geologic investigations provided necessary data for rock mass classification, developing geological model and support type along the tunnel axis for a safe and economical tunnel design.

## Conflict of Interests

No conflict of interest was stated by the authors.

## Acknowledgements

Authors express their gratitude to the managers and employees of Seza Civil San. Tic. A.Ş. and Yüksel Project International A.Ş for their contribution to the study.

## Declaration of Ethical Standards

The authors of this article declare that the materials and methods used in this study do not require ethical committee permission and legal-special permission.

## References

- [1] Akdeniz N., Akçören F., Timur E., 1994, Geology of Aşkale-İspir Between.
- [2] Ketin İ., 1969. Kuzey Anadolu Fayı hakkında, Maden Tetkik ve Arama Dergisi 72, pp.1-27.
- [3] Şengör A.M.C., 1980. Türkiye'nin neotektoniğinin esasları. Türkiye Jeoloji Kurumu, Konferans Serisi 2,

Ankara, 40 s.

- [4] Şaroğlu F., Yılmaz Y., 1984. Neotectonics and related Magmatism of Eastern Anatolia. İhsan Ketin Symposium, pp.149-162.
- [5] Koçyiğit A., 1985. Geotectonic Characteristics of the Çobandede Fault Belt Between Muratbağı-Balabantaş (Horasan) and Surface Fractures of the Horasan-Narman Earthquake. C. Ü. Eng. Faculty Journal, **2** (1), pp.17-34.
- [6] Bozkuş C., 1992. Çayırılı-Tercan Tertiary Basin of East (Tercan- Aşkale Break) Stratigraphy: Turkey Geological Congress newsletter, **7**, pp.97-107, Ankara.
- [7] Yüksel Project International A.Ş., 2013. Kırık Tunnel Geological-Geotechnical Assessment Report. Ankara.
- [8] Köse H., Gürgen S., Onargan T., Yenice H., Aksoy C.O., 2007. Tunnel and Well Drilling. İzmir: Dokuz Eylül University, Faculty of Engineering Publications No: 256.
- [9] Vardar M., Müller L., Sauer G., 1978. Dreidimensionale Spannungumlagerungs-prozesse im Bereich der Ortsrust. Rock Mech. Suppl., **9**, pp.67-85.
- [10] Barton N.R., Lien R., Lunde J., 1974. Engineering classification of rock masses for the design of tunnel support. Rock Mechanics and Rock Engineering, **6** (4), pp.189-236.
- [11] Bieniawski, Z.T. 1989. Engineering Rock Mass Classifications, John Wiley & Sons p. 251.
- [12] Hoek E, 1998; Rock Engineering For Tunnels, Technical Course Notes, Vancouver, Canada.
- [13] Austrian Standards Institute: ONORM B 2203-1. 2001.



## Evaluation of Society Response to Violence against Women in Turkey via Twitter using Topic Modeling

Emel OKKALI<sup>1</sup> , Hilmiye ATAMTÜRK<sup>2</sup> , Zeynep Hilal KİLİMCİ<sup>3,\*</sup> 

<sup>1</sup> Department of Information Systems Engineering, Kocaeli University, Kocaeli, 41001, Turkey, **ORCID:** 0000-0003-4214-6270

<sup>2</sup> Department of Information Systems Engineering, Kocaeli University, Kocaeli, 41001, Turkey, **ORCID:** 0000-0003-2349-3285

<sup>3</sup> Department of Information Systems Engineering, Kocaeli University, Kocaeli, 41001, Turkey, **ORCID:** 0000-0003-1497-305X

### Article Info

#### Research paper

Received : March 31, 2021

Accepted : May 26, 2021

#### Keywords

Violence against Women  
Opinion Mining  
Latent Dirichlet Allocation  
Social Media Mining  
Topic Modeling

### Abstract

In recent times, people's reactions to violence against women, harassment and murder have been shared more and more, thanks to social media. This, in turn, led to the organization of people and increased awareness of violence against women. Inspired by this study, it focuses on subject modeling techniques to determine people's perspectives on violence against women, which is growing day by day. Opinions from users about violence against women are collected using the social media platform Twitter in order to analyze the reaction of the society. After the preprocessing stage, Turkish tweets are analyzed using Latent Semantic Analysis (LSA), Latent Dirichlet Allocation (LDA), Hierarchical Dirichlet Process (HDP), Non-Negative Matrix Factorization (NMF) techniques. The results of the experiment show that the LDA technique significantly reveals the reaction of the society to violence against women and social awareness in Turkey.

## 1. Introduction

Violence against women is an important public health problem that can cause loss of workforce and even death in women and requires health care, as well as being a widespread social problem that is increasing day by day in society [1-2]. According to a report published by the World Health Organization in 2013 [3], approximately one-third (35%) of women worldwide experience physical and/or sexual violence. The same report also states that up to 38% of femicides worldwide are committed by a male partner. According to the 2002 report [4] in which the World Health Organization analyzed 48 studies conducted in different parts of the world, it was determined that 10-69% of women were exposed to physical violence by their husbands or partners at least once in their lives.

Social networks have a serious place in our daily life. Users evaluate their time using social platforms such as

Twitter, Facebook or Instagram. For this reason, the continuous use of social media platforms by millions of people has become a common research area and data source for researchers. The main reason for this is that the data is published on these platforms in different types such as images, texts, videos, in large volumes, by millions of people at the same time. For this reason, researchers or institutions who see Twitter as a data source and advantage, or profit factor have sought different ways to analyze the data [5-6]. Therefore, in this paper, we propose to analyze the responses of women to violence against women by extracting the views of people on Twitter with topic modeling techniques.

Topic modeling is an unsupervised approach to finding groups of words called topics in a text document. These topics consist of words that often appear together and often share a common theme. Therefore, with a predefined set of words, these topics can be used as a group of words to best

\* Corresponding Author: zeynep.kilimci@kocaeli.edu.tr



describe the entire document. Topic modeling facilitates us with different methods for organizing, understanding, and summarizing large collections of text data. In this study, Latent Semantic Analysis (LSA) [7-9], Latent Dirichlet Allocation (LDA) [10-12], Hierarchical Dirichlet Process (HDP) [13-15], Non-Negative Matrix Factorization (NMF) [16-18] methods are employed as topic modeling algorithms to determine people's perspective and requests on violence against women.

The remainder of this document is organized as follows: Chapter 2 provides a summary of work on issue modeling and machine learning approaches to violence issues. Chapter 3 explains the proposed framework. Chapters 4 and 5 present the experimental results and results, respectively.

## 2. Related Work

This section provides a brief summary of the limited computer science studies on violence against women.

In [19], Rodríguez-Rodríguez et. al propose to estimate and model gender-based violence (GBV) with the help of machine learning techniques. Authors evaluate the possibility of predicting the reports of gender violence with acceptable accuracy employing the most suitable technique for selecting variables and the most successful algorithm to get higher prediction performance. In order to demonstrate the effectiveness of the proposed model data set is gathered from January 2009 to September 2019 in Spain. Then, the training procedure is applied with Linear Regression (LR), Support Vector Machines (SVM), Random Forest (RF) and Gaussian Process (GP) models. Experiment results show that the combination of Multi-Objective Evolutionary Search Strategy (MOES) and RF is the best model for estimating GBV. In [20], Xue et. They evaluate the covert domestic violence epidemic during COVID-19 by presenting a broad analysis of the public discourse on domestic violence on Twitter. For this purpose, 1 million tweets about domestic violence and COVID-19 were collected between April 12 and July 16, 2020. Like our study, the authors focus on the unsupervised learning approach, using the Hidden Dirichlet Allocation (LDA) model to find prominent themes and topics. As a result of the study, the authors reveal 9 themes from nearly 1 million tweets about domestic violence and the COVID-19 pandemic. The results strikingly reflect the reason behind domestic violence and the COVID-19 pandemic.

In [21], Bello et. al concentrate on machine learning methodology to investigate the impact of gender-based violence in the Spain news media. Authors collect about 800,000 news from January 2005 to March 2020 by specifying class labels such as feminism, technology,

economy, politics, etc. After determining the relation between news and GBV, two consecutive neural network models are applied. Experiment results indicate that there is a clear relationship between GBV news and public consciousness, the effect of mediatic GBV cases, and the intrinsic thematic relationship of GBV news. In [22], Amusa et. al propose to forecast the vulnerability of women to intimate partner violence (IPV) in South Africa by employing machine learning techniques. For this purpose, South African demographic and health survey dataset that is constructed with contribution of 1,816 ever-married women, carried out in the experiments. In addition to regression analysis, authors also focus on decision trees both classification and regression purpose, random forest, and gradient boosting techniques to determine patterns and relationships in the data set. Among these models, random forest exhibits the superior performance to find the correlation between IPV and the fear of the husband.

In [23], Xue et. al investigate domestic violence topics on Twitter with the help of data mining methods. Thus, the authors propose to explore hidden subjects and thematic structures among domestic violence-related texts on the Twitter platform. To analyze, 322,863 comments are gathered utilizing the “domestic violence” tag. To discover domestic violence topics, LDA approach is proposed. They conclude the study that the most common 20 pairs of words are “violence awareness,” “Greg Hardy,” “awareness month,” “victims domestic,” “stop domestic,” and “Ronda Rousey”. This work also demonstrates the viability of employing topic-modeling techniques for detecting gender-based violence data on Twitter. In [24], Frenda et. al propose to automatically identify misogyny and sexism on Twitter by analyzing online hate speech against women. For this purpose, authors classify English tweets as misogynistic and sexist. The authors conclude the paper that the proposed approach can determine the two sides of patriarchal behavior, misogyny, and sexism, evaluating three collections of English tweets, and acquiring promising results.

Our study differs from the aforementioned literature works in terms of analyzing violence against women with various topic modeling techniques such as Latent Semantic Analysis (LSA), Latent Dirichlet Allocation (LDA), Hierarchical Dirichlet Process (HDP), Non-Negative Matrix Factorization (NMF) that provides the performance comparison. Moreover, this is the first attempt in terms of analyzing Turkish tweets related to violence against women and public awareness in Turkey by employing natural language processing techniques.

### 3. Proposed Framework

In this section of the study, topic modeling algorithms to be used in the construction of the proposed models, collection of the data set, pre-processing methods, and proposed model are mentioned.

#### 3.1. Latent Semantic Analysis (LSA)

Latent Semantic Analysis, or LSA, is one of the fundamental methods in subject modeling. The main idea is to create a matrix of documents and terms and decompose it into a standalone document-subject matrix and a subject-term matrix. The first step is to create a document term matrix.

Given  $x$  documents and  $y$  words in the vocabulary, the  $x \times y$  matrix can be constructed in which each row demonstrates a document, and each column indicates a word. In the plain version of LSA, each input can simply be a raw count of the number of times the  $j$ -th word seemed in the  $i$ -th document. In practice, however, raw counts do not work especially well because they do not account for the importance of each term in the document. For example, the term "5G" surely notifies more about the topics of a given document than the term "model." Consequently, LSA models generally substitute raw counts in the document-term matrix with a term frequency-inverse document frequency (tf-idf) score.

Once getting the document-term matrix, it is come across that the matrix is quite sparse, rather noisy, and somewhat redundant across its many dimensions. Consequently, to discover the few latent topics that find the relations among the words and documents, it is required that to conduct dimensionality reduction on the  $x \times y$  matrix. In this paper, dimension reduction is performed using truncated singular value decomposition (SVD), which is a technique in linear algebra that factorizes any matrix  $M$  into the product of 3 separate matrices:  $M=U \times S \times V$  where  $S$  is a diagonal matrix of the singular values of  $M$ .  $U$  means document-topic matrix, and  $V$  implies term-topic matrix. After that, cosine similarity is evaluated to assess the similarity of different documents, the similarity of different words and the similarity of terms and documents.

#### 3.2. Latent Dirichlet Allocation (LDA)

Latent Dirichlet Allocation (LDA) is a generative statistical technique that allows clusters of observations to be identified by unobserved clusters, which explains why parts of the data are similar. For instance, if the observations are terms gathered into documents, it assumes that each document is a combination of a small number of topics and

that the existence of each term is intrinsic to one of the topics of documents. Moreover, LDA is a kind of unsupervised learning technique that assesses documents as bag of words. That is, LDA ignores the order of terms in a document. LDA works by producing a document in two ways: choosing a set of topics and a set of words for each topic. Thus, there are 2 parts to be determined in LDA. The first one is that the terms/words that belong to a document. The second part is that the words that pertain to a topic or the probability of terms pertaining to a topic, that it is required to compute.

LDA demonstrates documents as a consolidation of topics. Likewise, a topic is a combination of words. If a word has a high probability of being in a topic, all the documents containing the word "w" will be more heavily involved with topic "t" as well. Like this, if the word "w" is not very possible to be in the topic "t", the documents which include the word "w" will be comprising very low probability of being in topic "t", because remnants of the words in the document "d" will pertain to some another topic and thence document "d" will have a higher probability for those topics. In the order to find the words that pertain to a topic or the probability of words pertaining to a topic, the proportion of words in document  $d$  that are assigned to topic  $t$  is calculated as a first step. This calculation finds how many terms pertain to the topic "t" for a given document "d". As a next step, the proportion of assignments to topic "t" over all documents is computed that come from the word "w". This presents how many documents are in topic "t" due to the word "w". Finally, the probability for the word "w" pertain to topic "t" is updated by multiplying the outputs of step 1 and step 2.

#### 3.3. Hierarchical Dirichlet Process (HDP)

Standard parametric topic models such as LDA confront the difficulty of specifying the number of topics. The nonparametric topic modeling concept defeats this problem exploiting Bayesian nonparametric, in which the number of topics does not require to be specified previously and can be deduced from the data. The hierarchical Dirichlet Process which is an expansion of the LDA model can conduct as well as the best LDA model in terms of perplexity while doing so without any model selection process. The main structure stone of HDP is the Dirichlet process (DP), a probability distribution of discrete distributions over the topic space. Topic modeling necessitates the topics to be agreed upon both within each document and across different documents. In order to meet sharing topics across different documents, HDP extends the DP approach. This way, it is capable of topic sharing across different documents by putting into practice a shared DP prior to the basis distributions of the DPs for each document.



### 3.4. Nonnegative Matrix Factorization (NMF)

The non-negative matrix approach is a set of algorithms in multivariate analysis and linear algebra where a matrix  $M$  is generally resolvable into factors by providing two matrices  $N$  and  $R$ , with the characteristic that there are no negative elements in all three matrices. The non-negativity allows the result matrices simpler to examine. NMF is applied in such fields as astronomy, computer vision, document clustering, missing data imputation, chemometrics, audio signal processing, and bioinformatics, etc.

NMF is a kind of unsupervised machine learning like other topic modeling methods. The main cornerstone of unsupervised learning is the quantification of the distance between the elements. The distance between elements is calculated by different methods such as generalized Kullback–Leibler divergence, Frobenius norm, etc. Generalized Kullback–Leibler divergence, statistical measurement, is employed to quantify how one distribution is varied from another. If the value of divergence is less which means the value of Kullback–Leibler divergence is close to zero, the proximity of the correspondent terms increases.

In addition to generalized Kullback–Leibler divergence, Frobenius norm is also employed for NMF. In addition to generalized Kullback–Leibler divergence, Frobenius norm is also employed for NMF. Frobenius norm, aka euclidean norm, is described by the square root of sum of absolute squares of its elements. In topic modeling, non-negative matrix factorization, a statistical method, is applied for the purpose of decreasing the dimension of the input corpus. Thence, NMF employs the technique of factor analysis in order to ensure rather less weight to the terms with less coherency. Assume that, there is an input matrix  $M$  of shape  $a \times b$ . Through NMF,  $M$  is factorized into two matrices namely,  $N$  and  $R$ , such that the dimension of  $N$  is  $a \times c$  and that of  $R$  is  $c \times b$ . In this situation,  $M$  demonstrates the term document matrix. This means each row of matrix  $R$  is a word embedding and each column of the matrix  $N$  shows the weight of each term obtained from each sentence. Thus, the relationship between words with each sentence is obtained semantically.

### 3.5. Proposed Model

In this section, we introduce the proposed framework for the purpose of evaluating society's reaction to violence against women in Turkey through Twitter using four different topic modeling techniques. As a first step, we focus on data gathering. In order to analyze the Turkish user comments related to violence against women, the dataset is

constructed through the Twitter social media platform. For this purpose, different hashtags are determined and crawled employing Selenium crawler. Hashtags are chosen on words that evoke violence against women, and sometimes they are collected with the names of women who are the subject of women's murders. These include KadinaSiddeteHayir, KadinaSiddet, KadinCinayeti, KadinaSiddeteDurDe, İstanbulSözleşmesi, İstanbulSözleşmesiYaşatır, KadinaŞiddeteTepkisizKalma, KadınKatliamıVar, İstanbulSözleşmesiniUygula, İstanbulSözleşmesindenVazgeçmiyoruz hashtags, etc. In total, 67,751 Turkish comments are gathered utilizing more than 25 hashtags between June 2011 and December 2020. However, not enough comments are allowed to be taken by TwitterScraper and Twitter API, we focus on Selenium crawler. Thanks to the Selenium crawler, the limitation problem about downloading and gathering Turkish tweets from Twitter is overcome.

After gathering the raw dataset from Twitter, preprocessing step is initialized in order to clean noise from the dataset. Another reason behind performing pre-processing stage is to obtain more precise results. For this purpose, stop word elimination, removing hashtags, removing URLs, punctuation mark cleaning, removing non-alphanumeric symbols, and facial expression cleaning (emojis) are conducted. In this study, the process of dividing words into their roots (stemming) is not employed as a pre-processing technique, because when the word is separated into its root, it can lead to a positive change in meaning or a negative loss of meaning. For example, when we think of the word "ölmessin" (do not die), which is very related to the subject, the root of the word is "öl" (die). However, the original of the word contains the meaning of negativity. Loss of meaning occurs when the word is separated from other suffixes. This, in turn, can be misleading when society's response to violence against women wants to be measured. Because of this reason, stemming is not included in the pre-processing procedure.

After the pre-processing stage, the document-term matrix is separately constructed by employing the term-frequency (tf) approach for both unigrams and bigrams. Thence, each term or component demonstrates the count of each unigram or bigram that occurs in each of the Twitter comments. In modelling stage, four different topic models namely, latent semantic analysis (LSA), latent Dirichlet allocation (LDA), nonnegative matrix factorization (NMF), hierarchical Dirichlet process (HDP) are evaluated in order to detect the perception of society on violence against women in Turkey. Especially since literature studies on violence against women mostly focus on LDA or LSA models, we make a comprehensive comparison by including other models in this study. We also investigate the impact of other topic models on determining the reaction of society to

violence against women in Turkey. In order to analyze the effect of topic modeling techniques, eight topics are assessed. To compare the performance of different models, topic coherence is evaluated as an evaluation metric. C<sub>v</sub> coherence measure is employed in the experiments to demonstrate coherence value between topics. Moreover, hyperparameter tuning is performed in order to get the best results when alpha is 0.01, beta is 0.9, and number of topics is set to 8. All experiments are performed with Python programming language using 3.6.8 version. In addition to comparing different topic models in terms of topic coherence value, we also analyze the effect of unigrams and bigrams on the best performed topic model. As a first step, each model is assessed on unigram model. After determining best topic model, the effect of bigram is investigated. A general flow chart of the proposed model is presented in Figure 1.

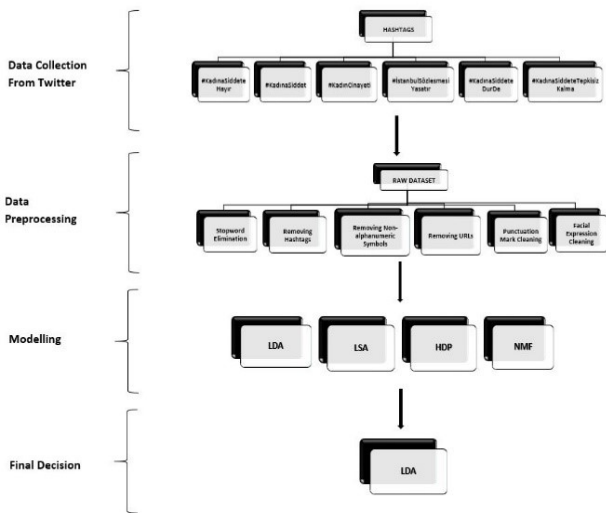


Figure 1. A general flow chart of the proposed model.

### 4. Experiment Results

In this section, we present the comprehensive experiment results. Our aim is to explore the conversations and discussions about violence against women in Turkey on Twitter. For this purpose, we utilize four different topic model techniques to analyze latent topics related to violence against women in a dataset of tweets. Especially, we aim to find answer several research questions with regard to Twitter postings that include violence against women.

- i) What are the most common terms in the whole dataset?
- ii) Are the terms about violence against women tend to comprise together?
- iii) What topics about violence against women arise most constantly?
- iv) On what topics does the whole data set center?

In this paper, we focus on eight topics to analyze the effect of topic modeling techniques. In order to compare the performance of different models, topic coherence is assessed as an evaluation criterion. Topic coherence estimates score a unique topic by assessing the degree of semantic similarity between high scoring terms in the matter. Thus, topic coherence value helps to allocate between those that are semantically interpretable ones and those that are outputs of statistical inference. C<sub>v</sub> coherence measure is employed in the experiments to demonstrate coherence value between topics. C<sub>v</sub> measure is based upon one-set partition of the top terms, a sliding window, and an implicit confirmation estimate that uses normalized pointwise mutual information (NPMI) and the cosine similarity.

In Figure 2, the topic coherence values for LSA model are presented. It is obviously seen that the coherence value of topic 4 is nearly 0.38. It is followed by topic 7, topic 5, topic 6, topic 8, topic 1, topic 3, and topic 2. However, topic 4 exhibits the best coherence value, it is not enough to demonstrate the degree of semantic similarity between high scoring terms in the topic. Topic 4 covers the following terms: “idam”, “kadınlar”, “ceza”, “ölmesin”, “müebbet”, “ağır”, “sözleşme”, “ölüm”, “cinayet”, “tecavüz”. Topic 2 includes “sözleşmesini”, “İstanbul”, “uygulayın”, “kadınların”, “koruyan”, “tbmm”, “adalet”, “sözleşmesi”, “uygulansın”, “bakanlık” terms. On the other hand, the poorest relation between terms in topic 2 is attracted the attention with 0.29 coherence value. This means that the topic 2 is not capable cover to distinguish topics in order to demonstrate semantically interpretable. When the meanings of the terms of topic 4 are analyzed compared to the terms of topic 2, it is not surprising that topic 4 has the highest coherence value. In Figure 3, word cloud representation of topic terms is also presented to observe the distribution of the terms by using LSA algorithm.

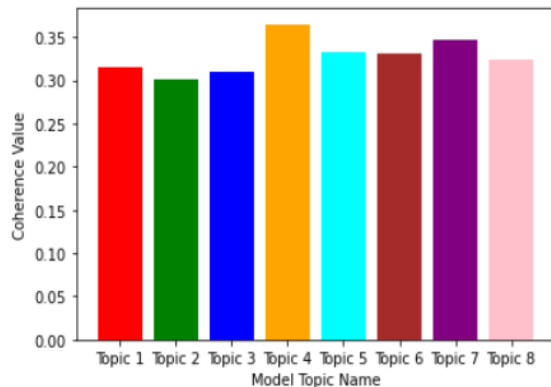
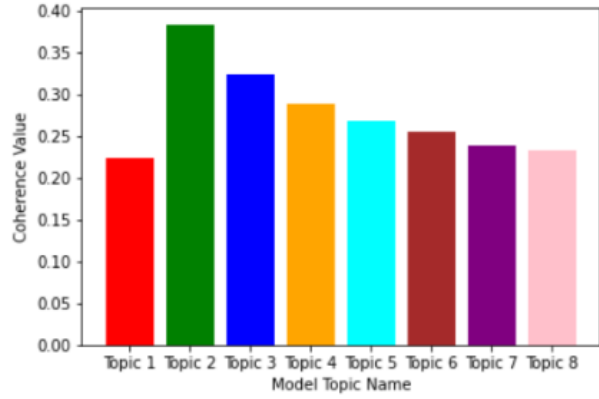


Figure 2. The chart of topic coherence values for LSA model.



**Figure 3.** The word cloud demonstration of topic terms for LSA model.

In Figure 4, the topic coherence results of HDP model are indicated. Although the coherence result of Topic 2 is superior compared to the other topics, HDP model is another poor method with roughly 0.38 coherence value when all topic models are considered. The HDP model performs like the LSA model in terms of coherence values. This means that the LSA and HDP model do not perform well enough semantically in terms of topics. Furthermore, HDP technique exhibits the poorest success when the performance of other topics is observed compared to LSA model. Topic 2 includes the following top ten words in terms of word scores: “uygulayın”, “koruyan”, “sözleşme”, “kadın”, “haksızlık”, “bakanlık”, “hadım”, “İstanbul”, “yaşamak”, “şiddetin”. Topic 2 is followed by topic 3, topic 4, topic 5, topic 6, topic 7, topic 8, and topic 1 in terms of coherence values. Topic 3 with nearly 0.33 coherence result includes the following terms: “anne”, “kadın”, “beyler”, “şiddetin”, “ölmesin”, “koruyan”, “sözleşmesi”, “adalet”, “uygulansın”, “imza”. When the terms are examined in topic 2, semantic similarity with words in topic 3 is observed, clearly. This is the indicator of high scoring words in both topics. Conversely, topic 1 demonstrates the worst coherence value result. When the terms are analyzed in topic 1, the semantic similarity between the terms is much lower than the other topics. These terms are “canı”, “kampanyaya”, “hak”, “bıktık”, “ıdam”, “küçük”, “şiddete”, “sessiz”, “artık”, “ölmek”. It is clearly seen that there is a low scoring words that mean the lower semantic similarity between terms located in topic 1 when the meanings of the words are assessed. In Figure 5, word cloud representation of topic terms is also presented to observe the distribution of the terms by using HDP technique.



**Figure 4.** The chart of topic coherence values for HDP model.

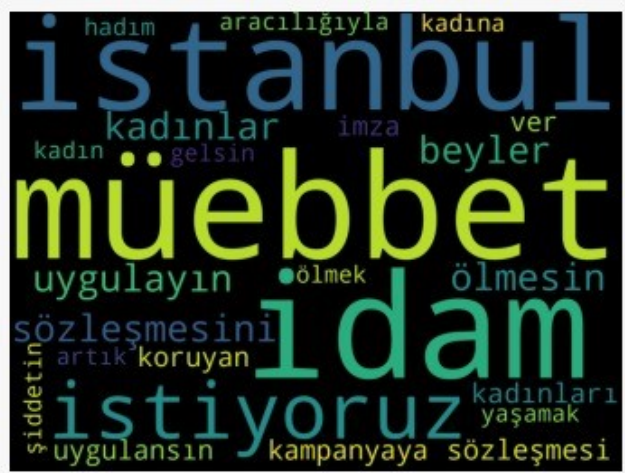


**Figure 5.** The word cloud demonstration of topic terms for HDP model.

In Figure 6, topic coherence results are demonstrated among eight topics with the usage of NMF model. NMF model is the second-best model with Topic 4 and nearly 0.50 score when coherence results are evaluated. Topic 4 is followed by Topic 5, Topic 6, Topic 7, Topic 3, Topic 8, Topic 2, Topic 1. NMF model ensures to separate semantically interpretable topics with the higher coherence value compared to the LSA and LDA for topic 4. NMF model is also competitive for topic 5, topic 6, topic 7, and topic 8 when LDA method is considered in terms of coherence values. When the performance of LSA and HDP is considered NMF is more suitable to evaluate of society response to violence against women in Turkey through Twitter in terms of both comparing coherence results and popular unigrams. The performance order of topic models can be summarized as when LDA is not considered yet: NMF> LSA> HDP. When the terms are analyzed in topic, semantic similarity with words in topic 3 is seen, obviously. This means that the high scoring words are presented in both topics. On the other hand, topic 1 shows the poorest coherence value. When the terms are analyzed in topic 1, the

semantic similarity between the terms is much lower than the other topics. These terms are “kampanya”, “pazarlık”, “sözleşme”, “madde”, “bugün”, “ağustos”, “ceza”, “herkesten”, “İstanbul”, “kuvayı”. It is clearly seen that there are low scoring terms that mean the lower semantic similarity between words presented in topic 1 when the meanings of the words are evaluated. In Figure 7, word cloud representation of the topic terms is also presented to observe the distribution of the terms by using NMF technique.

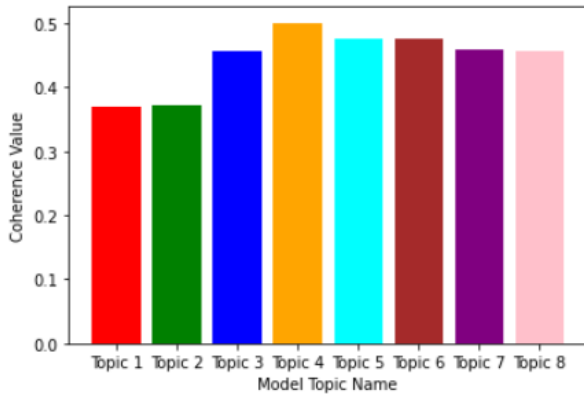


**Figure 6.** The chart of topic coherence values for NMF model.

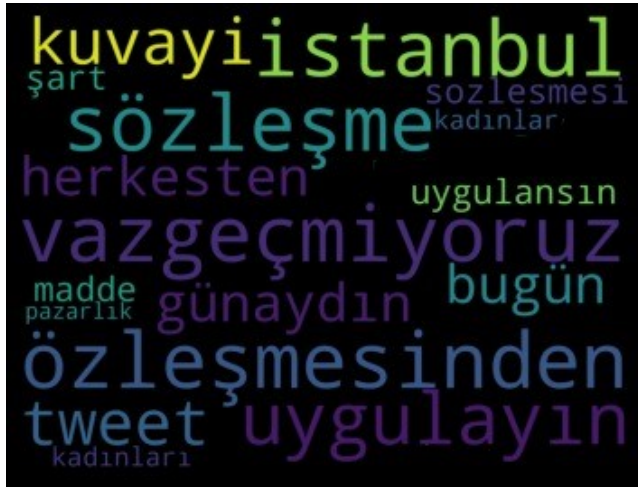


**Figure 7.** The word cloud demonstration of topic terms for NMF model.

The experimental results show that the LDA model, among other subject models, shows remarkable results in terms of reflecting the society's reaction to violence against women and public awareness in Turkey. In Figure 8, topic coherence results are represented among eight topics. As clearly observed from Figure 8, Topic 2 indicates approximately 0.53 coherence value that outperforms the performance of the other topics. This means that the LDA model provides semantically interpretable subjects with a higher coherence result compared to other subject models. Topic 2 contains the following terms: “ceza”, “idam”,

“müebbet”, “şiddet”, “ölüm”, “cinayetleri”, “kadınlar”, “sözleşmesi”, “uygulayın”, “İstanbul”. Topic 2 is followed by Topic 3 with 0.48 coherence value that is also competitive when the best results of LSA model is considered. Topic 3 covers the following terms: “şiddet”, “hayır”, “cinayet”, “uygula”, “kampanya”, “imza”, “adalet”, “istismar”, “müebbet”, “sözleşme”. When the words are analyzed in topic 3, semantic similarity with the terms in topic 2 attracts the attention that demonstrates high scoring terms in both topics. On the other hand, the poorest coherence value is exhibited by topic 1. When the terms are seen in topic 1, the semantic similarity between the words is much lower than the ones in the other topics. These words are “istiyoruz”, “kötü”, “hak”, “doğru”, “idam”, “beyler”, “gerek”, “kadın”, “yeter”, “basın”. It is obviously observed that there is a low scoring terms that reflects the lower semantic similarity between words located in topic 1 when the meanings of the terms are evaluated. When evaluating each topic modeling technique and coherence values between topics, it is seen that the LDA model mostly shows the best coherence value between topics except topic 4. It is followed by the NMF model for 5,6,7,8 topics and is highly competitive. This, in turn, shows that the semantic similarities of the words are greater in the topics involved in the NMF model, primarily after the LDA model. In this way, the topics extracted employing the LDA model and the words contained in it appear to be the model that mostly best reflects society's thoughts on violence against women in the Twitter environment.

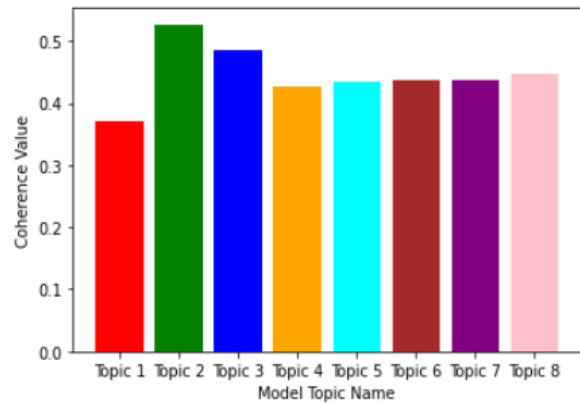


**Figure 8.** The chart of topic coherence values for LDA model.

Table 1 is presented to answer the question of what the most common terms in the entire data set are. In Table 1, the most significant five terms of related topics according to term scores with the usage of LDA model is represented. It is obviously seen that eight topics are comprised of similar contents. When topic 2 and topic 3 are considered, the terms located in the related topic are semantically more similar compared to the other topics. High scoring words in the topic through the level of semantic similarity also determine

the distribution of words in the topic as presented Table 1. In this way, the experimental results are consistent when considering the consistency values of each subject. Moreover, we introduce the most common words related to violence against women in the whole dataset. In addition to the search keyword “kadasiddet” (violence against women), the results indicate that popular unigrams for the LDA model are “müebbet”, “ölüm”, “ceza”, “şiddet”, “idam”, “İstanbul”, “kadın”, “sözleşme”, etc.

**Table 1.** Top five popular unigrams of related topics through LDA model.

Topics	Term1	Term2	Term3	Term4	Term5
1	kadın	istiyoruz	şiddet	yeter	erkek
2	idam	müebbet	ceza	kadın	adalet
3	şiddet	ölüm	cinayet	uygula	lanet
4	idam	şiddet	af	susma	istismar
5	İstanbul	uygula	sözleşme	çocuk	müebbet
6	istiyoruz	ölmesin	kadınlar	idam	yaşam
7	yeter	insanlık	kan	tutukla	ölüm
8	bela	ceza	Allah	lanet	idam

In Figure 9, word cloud representation of topic terms is also presented to show the distribution of the terms by using LDA algorithm.



**Figure 9.** The word cloud demonstration of topic terms for LDA model.

In order to find the solution of the question whether violence against women related terms tend to comprise together, we focus on bigrams (pair of terms/words) and observe the impact of it on LDA model because the LDA model is the best among the other topic models. When we consider that bigram only ensures two concessive terms, regardless of the grammar construction and semantic content, then, it will be seen that some bigrams that are not listed in Table 2 such as "uygulayın kadınlar", "artık

yaşamak" might not be self-explanatory. In Table 2, top ten popular and meaningful bigrams are listed in the data set. Top 10 common words with the highest percentage in all 16,672 bigrams are picked up. The remaining of the 16,672 bigrams constitute 76.32%. When the top ten popular bigrams are examined, most Turkish people express their opinion that violence against women should not go unpunished. We also observe that the idea of execution or life imprisonment outweighs it. Moreover, many users state that they want the contract to be valid for penalties. In this sense, our study clearly reveals the thoughts and reactions of the society on violence against women, which is the wound of many societies. LDA results express that many bigrams tend to comprise together among violence against women related tweets, such as “müebbet istiyoruz”, “İstanbul sözleşmesi”, “şiddete hayır”, etc. Furthermore, the co-occurring terms are in common topics. For example, bigram "müebbet istiyoruz" can be in both topic 1 and topic 3.

**Table 2.** Top ten popular bigrams

Popular bigrams	Dataset (%)
Müebbet istiyoruz	5.24%
İstanbul sözleşmesi	3.82%
İdam istiyoruz	3.65%
Kadına şiddet	1.14%
Şiddete hayır	0.86%
Sözleşmeyi uygulayın	0.81%
Yaşamak istiyoruz	0.75%
Yeter artık	0.52%
Adalet nerede	0.35%
Kadın dayanışması	0.29%

It is difficult to compare the performance of our results with the other studies because of the lack of works with similar datasets, different topic modeling techniques, and various evaluation metrics. Our study differs from aforementioned literature works in terms of analyzing violence against to women with various topic modeling techniques such as Latent Semantic Analysis (LSA), Latent Dirichlet Allocation (LDA), Hierarchical Dirichlet Process (HDP), Non-Negative Matrix Factorization (NMF) that provides the performance comparison. Moreover, this is the first attempt in terms of analyzing Turkish tweets related to violence against women and public awareness in Turkey by employing natural language processing techniques. Most of the literature studies on violence against someone [20,23] focus on to analyze the effect of only LDA model without comparing other methods which proves the contribution of the LDA model to extract the useful information from the

document collection about violence subject. In [20], Xue et. al assess the hidden pandemic of family violence during COVID-19 via Twitter by employing LDA model. Authors conclude the study [20] that the results significantly reflect the reason behind domestic violence and the COVID-19 pandemic while our study centers on to expose the reaction of society to violence against women and public awareness in Turkey. Both studies emphasize that the LDA model is successful, while our study also reveals that the NMF model is very competitive when compared to LDA technique.

In [23], Xue et. al center on domestic violence topics on Twitter with the help of LDA technique. Thus, authors present to investigate hidden subjects and thematic structures among domestic violence-related texts on Twitter platform. In order to analyze domestic violence topics, LDA approach is proposed. They conclude the study that the most common 20 pairs of words are “violence awareness,” “greg hardy,” “awareness month,” “victims domestic,” “stop domestic,” and “ronda rousey”. Similar to study [20], authors focus on only LDA method to analyze the domestic violence related topics while our study intends to explore society response to violence against women in Turkey in addition to determine violence against women-related topics similar to other studies [20,23]. Moreover, we also evaluate the effect of LSA, HDP, and NMF models on violence against women unlike other studies. Our study reveals that tweets released from Twitter are a powerful indicator in order to reflect the thoughts and expectations of the society. Moreover, given the messages posted on Twitter about violence against women, it is clear that people often complain that there is no deterrent sanction against violence against women. For this reason, in the content of the posted messages, they often use words related to the sanctions or regulations that they want to be put into action.

## 5. Discussion and Conclusion

In this work, we focus on topic modeling models in order to analyze people's perception on violence against women, which is growing a little bit more every day. Opinions shared by users about violence against women are gathered employing social media platform Twitter for the purpose of analyzing pulse of the society. After pre-processing stage, Turkish tweets are analyzed by using Latent Semantic Analysis (LSA), Latent Dirichlet Allocation (LDA), Hierarchical Dirichlet Process (HDP), Non-Negative Matrix Factorization (NMF) techniques. In order to analyze aforementioned models, unigrams are evaluated. Experiment results demonstrate that LDA model maintains to allocate semantically explicable topics with the higher coherence result compared to the other topic models for unigrams. After determining the most suitable model for

unigrams, we also investigate the impact of bigrams in order to assess the pulse of the society in terms of violence against women in Turkey. In order to demonstrate the effect of bigrams, LDA model is implemented. Experiment results demonstrate that LDA technique remarkably shows the pulse of the society to violence against to women and public awareness in Turkey for the usage of both unigrams and bigrams.

As a feature study, we aim to analyze the effect of bigrams in more detail and expand the study by evaluating trigrams.

## Declaration of Ethical Standards

The authors of this article declare that the materials and methods used in this study do not require ethical committee permission and/or legal-special permission.

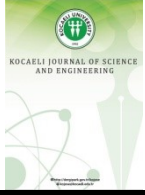
## Conflict of Interest

The authors declare that they have no known competing financial interests or personal relationships that could have appeared to influence the work reported in this paper.

## References

- [1] Gencer M.Z., Ağırman E., Arıca S, 2019. İstanbul ilinde kadına yönelik şiddet sıklığı ve kadınların şiddet algısı. *Ahi Evran Tıp Dergisi*, **3**(1), pp. 18-25.
- [2] Özkan G, 2017. Kadına yönelik şiddet-aile içi şiddet ve konuya ilişkin uluslararası metinler üzerine bir inceleme. *Hacettepe Hukuk Fakültesi Dergisi*, **7**(1), pp. 533-564.
- [3] World Health Organization Global and Regional Estimates of Violence Against Women: Prevalence and Health Effects of Intimate Partner Violence and Non-Partner Sexual Violence 2013. <http://apps.who.int/iris/bitstream/handle/10665/85239/?sequence=1>. (Access date: 08 March 2021).
- [4] World Health Organization. World Report on Violence and Health 2002. [https://www.who.int/violence\\_injury\\_prevention/violence/world\\_report/en/summary\\_en.pdf](https://www.who.int/violence_injury_prevention/violence/world_report/en/summary_en.pdf) (Access date: 08 March 2021).
- [5] Okazaki M., Matsuo Y., 2008. Semantic Twitter: Analyzing tweets for real-time event notification. Paper presented at International Conference on Social Software, Cork, Ireland, 3–4 March, pp. 63–74.
- [6] Pang B., Lee L., 2008. Opinion mining and sentiment analysis. *Foundations and Trends in Information*

- Retrieval, **2**, pp. 1–135.
- [7] Landauer T.K., Foltz P.W., Laham D., 1998. An introduction to latent semantic analysis. *Discourse Processes*, **25**(2-3), pp. 259-284.
- [8] Dumais S.T., 2004. Latent semantic analysis. *Annual Review of Information Science and Technology*, **38**(1), pp. 188-230.
- [9] Landauer T.K., McNamara D.S., Dennis S., Kintsch W., 2013. *Handbook of Latent Semantic Analysis*, 2<sup>nd</sup> ed. Psychology Press, New York, USA.
- [10] Blei D.M., Ng A.Y., Jordan M.I., 2003. Latent Dirichlet allocation. *The Journal of Machine Learning Research*, **3**, pp. 993-1022.
- [11] Hoffman M., Bach F.R., Blei D.M., 2010. Online learning for latent dirichlet allocation. *Advances in Neural Information Processing Systems*, **23**, pp. 856-864.
- [12] Wang X., Grimson E., 2007. Spatial latent Dirichlet allocation. Paper presented at Annual Conference on Neural Information Processing Systems, Vancouver, Canada, 3-6 December, pp. 1577-1584.
- [13] Teh Y.W., Jordan M.I., Beal M.J., Blei D.M., 2006. Hierarchical Dirichlet processes. *Journal of the American Statistical Association*, **101**(476), pp. 1566-1581.
- [14] Wang C., Paisley J., Blei D.M., 2011. Online variational inference for the hierarchical Dirichlet process. Paper presented at International Conference on Artificial Intelligence and Statistics, Lauderdale, FL, USA, 11-13 April, pp. 752-760.
- [15] Paisley J., Wang C., Blei D.M., Jordan M.I., 2014. Nested hierarchical Dirichlet processes. *IEEE Transactions on Pattern Analysis and Machine Intelligence*, **37**(2), pp. 256-270.
- [16] Lee D.D., Seung H.S., 1999. Learning the parts of objects by non-negative matrix factorization. *Nature*, **401**(6755), pp. 788-791.
- [17] Xu W., Liu X., Gong Y., 2003. Document clustering based on non-negative matrix factorization. Paper presented at International ACM SIGIR Conference on Research and Development in Information Retrieval, Toronto, Canada, 28 July- 1 August, pp. 267-273.
- [18] Hoyer P.O., 2004. Non-negative matrix factorization with sparseness constraints. *Journal of Machine Learning Research*, **5**(9), pp. 1457–1469.
- [19] Rodríguez-Rodríguez I., Rodríguez J.V., Pardo-Quiles D.J., Heras-González P., Chatzigiannakis I., 2020. Modeling and forecasting gender-based violence through machine learning techniques. *Applied Sciences*, **10**(22), pp. 1-22.
- [20] Xue J., Chen J., Chen C., Hu R., Zhu T., 2020. The hidden pandemic of family violence during COVID-19: Unsupervised learning of tweets. *Journal of Medical Internet Research*, **22**(11), pp. 1-11.
- [21] Bello H.J., Palomar N., Gallego E., Navascués L.J., Lozano C., 2020. Machine learning to study the impact of gender-based violence in the news media. *arXiv preprint arXiv:2012.07490*, pp. 1-17.
- [22] Amusa L.B., Bengesai A.V., Khan H.T., 2020. Predicting the vulnerability of women to intimate partner violence in South Africa: Evidence from tree-based machine learning techniques. *Journal of Interpersonal Violence*, **2020**, pp. 1-18.
- [23] Xue J., Chen J., Gelles R., 2019. Using data mining techniques to examine domestic violence topics on Twitter. *Violence and Gender*, **6**(2), pp. 105-114.
- [24] Frenda S., Ghanem B., Montes-y-Gómez M., Rosso P., 2019. Online hate speech against women: Automatic identification of misogyny and sexism on twitter. *Journal of Intelligent and Fuzzy Systems*, **36**(5), pp. 4743-4752.



# Conducting Polymer Based Enzyme Electrodes Fabricated by Invertase and Polyphenol Oxidase

Elif DOĞAN<sup>1</sup> , Ayşe Elif BÜYÜKBAYRAM<sup>2,\*</sup> 

<sup>1</sup> Department of Chemistry, Karabük University, Karabük, 78050, Turkey, **ORCID:** 0000-0002-3681-1345

<sup>2</sup> Department of Chemistry, Karabük University, Karabük, 78050, Turkey, **ORCID:** 0000-0002-9085-6042

## Article Info

### Research paper

Received : September 04, 2020

Accepted : June 12, 2021

### Keywords

Carbon Fiber Electrode  
Conducting Polymer  
Enzyme Immobilization  
Polyphenol Oxidase

## Abstract

Novel carbon fiber enzyme electrodes were constructed and evaluated. Fabrication of electrodes was performed via electrochemical deposition of a conducting matrix composed of polythiophene and polypyrrole (PTH-PPy) onto carbon fiber substrates. The enzyme was entrapped into the matrix during electropolymerization. Resultant biosensors represented higher kinetic parameters,  $V_{max}$  and  $K_m$ , in comparison to PPy matrix, which are  $2.471 \pm 0.150 \mu\text{mol min}^{-1} \text{electrode}^{-1}$  and  $30.60 \pm 5.30 \text{ mM}$  for invertase,  $0.056 \pm 0.012 \mu\text{mol min}^{-1} \text{electrode}^{-1}$  and  $842.00 \pm 37.50 \text{ mM}$  for polyphenol oxidase respectively. Optimum pH and temperature of the immobilized enzyme within PTH-PPy composite indicates that this matrix provides a more protective environment. The detection limit (LOD) of polyphenols was obtained as  $0.037 \text{ mg mL}^{-1}$ . Polyphenol oxidase enzyme electrodes were proved to be used for the determination of polyphenolic substances in real samples and the results were confirmed by the Folin-Ciocalteu method.

## 1. Introduction

Carbon fiber (CF) microelectrodes are considered useful substrates since they are inexpensive, possess high biocompatibility, and can be employed with a variety of surface modifications [1,2]. As an inorganic material, it possesses inertness against humidity, weak base, and acid at room temperature. In biosensor applications, its porous and high-surface-area microstructure allows CF to be loaded by large quantities of biomaterials, which makes the sensitivity of the resulting sensor enhances. Since their dimension is in micro and nano levels, they serve as a convenient tool for micro sample measurements (single droplet or single cell) [3,4]. They have been utilized in the construction of enzymatic biosensors, which involve studies on particularly glucose oxidase and polyphenol oxidase (tyrosinase) [1,5,6]. Here, polymer-modified CF substrates were selected to be used for the fabrication of

enzymatic biosensors.

The use of immobilized enzymes has advantages over the use of free enzymes. Since the use of free enzymes makes the industrial processes expensive, there is a demand for more economical ways on the enzymatic applications in the industrial scale. Concerning this problem, the immobilization of the enzyme into a suitable supporting material provides the possibility of multiple uses of the enzyme and consequently reduces the cost of the enzymatic processes. Enzymes are sensitive biomolecules that can be denatured easily by external conditions. Immobilization in a matrix usually offers a protective environment for enzymes and it becomes more resistive to changes in the conditions. Besides, the reaction between enzyme and substrate can be easily stopped by removing the enzyme immobilized matrix from the reaction medium. The reaction medium is not contaminated with the enzyme and a clean product is obtained [7].

Conducting polymers are frequently used in biosensors and many studies have been devoted to the immobilization of enzymes to these matrices [8-10].

\* Corresponding Author: [aebuyukbayram@karabuk.edu.tr](mailto:aebuyukbayram@karabuk.edu.tr)





Here, a composite material that consisted of polypyrrole and polythiophene (PTh-PPy) was used for enzyme immobilization because of the remarkable stability of these two polymers. PPy gains most of the interest because of its unique properties such as low oxidation potential, solubility in water rendering the polymerization possible in aqueous solutions, and long-lasting stability in room conditions [11]. In this study, entrapment of enzyme into a composite film is based on the codeposition during polymerization of PPy on previously PTh coated CF substrate in an aqueous enzyme solution containing supporting electrolyte. Among the immobilization methods, electrochemical polymerization offers a simple and rapid, one-step fabrication of enzyme electrodes [12].

One of the enzymes studied in this work is invertase (INV), an enzyme that is used as a model enzyme in immobilization studies, to have an idea about the performance of electrodes. The other enzyme, polyphenol oxidase (PPO) catalyzes hydroxylation and oxidation of monophenols and diphenols to corresponding *o*-quinones. Its substrate is polyphenolic substances; a large family of natural compounds which play a major role in the growth and reproduction of fruits and vegetables and supply protection against pathogens [13]. Phenolic compounds have a wide range of beneficial properties to health with their antioxidant activity [14,15]. Due to the large demand for antioxidants nowadays in city life, the phenolic content of foods acquires considerable importance. On the other hand, polyphenolics in natural waters are organic pollutants that have a detrimental influence on humans and animals. Phenolic derivatives are widely used chemicals in the manufacturing of industrial products. They are released to environmental waters through the wastewater of the production plants and have a hazardous effect on aquatic life. Phenolics are considered one of the priority pollutants by the American Environmental Protection Agency. Since they are toxic and persistent in the environment, their determination in natural waters is of great importance.

The study aimed to develop an alternative method to the reported biosensors for the quantification of polyphenolic compounds. CF substrates were used to construct micro-level electrodes for micro samples. The enzyme was immobilized to have a multiple-use tool to reduce the cost of the enzymatic applications. Immobilization was performed by using a conducting polymer composite to provide a protective microenvironment for the enzyme. After the fabrication, enzymatic microelectrodes were characterized by the investigation of the optimized conditions, and the kinetic parameters [16].

## 2. Materials and Methods

### 2.1. Materials

INV (E.C.3.2.1.26) Type V and Tyrosinase from mushroom (E.C.1.14.18.1) were purchased from Sigma. Pyrrole and sodium dodecyl sulfate (SDS) were supplied from Merck. Nelson's reagents constituents were of analytical grade, ammonium heptamolybdate tetrahydrate ( $(\text{NH}_4)_6\text{Mo}_7\text{O}_{24}\cdot 4\text{H}_2\text{O}$ ) and sodium arsenate di-basic-7-hydrate ( $\text{Na}_2\text{HAsO}_4\cdot 7\text{H}_2\text{O}$ ) were provided from Aldrich. 3-Methyl-2-benzothiazolinone hydrazone hydrochloride hydrate ( $\text{C}_8\text{H}_9\text{N}_3\text{S}\cdot \text{HCl}\cdot \text{H}_2\text{O}$ , MBTH) was bought from Aldrich and catechol from Sigma-Aldrich. GAMRY Instruments Interface 1000 Potentiostat/Galvanostat/ZRA and Wenking POS-88 potentiostats, Shimadzu UV-1201-V model spectrophotometer, and Carl ZEISS ULTRA PLUS GEMINI FESEM scanning electron microscope (SEM) were used for characterization.

### 2.2. Preparation of Enzyme Electrodes

CF was attached to a steel wire with Teflon tape. It was inserted into a tapered micropipette tip, fixed in place by an epoxy resin. A glass tube was placed around the wire. Prepared CF electrode was used as working electrode in a typical three-electrode cell in which electropolymerization was performed, containing also 0.5 cm<sup>2</sup> Pt foil as counter electrode and an Ag wire as a reference electrode. PTh was synthesized in acetonitrile containing 0.05 M tetrabutylammonium tetrafluoroborate and 6.5 μL/mL thiophene. Immobilization of enzyme was achieved via electropolymerization of PPy on previously PTh coated CF electrodes in a 10 mL buffer solution. Acetate buffer (pH 5.0) including 0.6 mg/mL SDS (as supporting electrolyte), 5.0 μL/mL pyrrole, 0.6 mg/mL INV and citrate buffer (pH 7.0) containing 1.0 mg/mL SDS, 5.0 μL/mL pyrrole and 0.4 mg/mL PPO (2687 U/mg solid) were used for INV and PPO immobilization respectively. It was carried out by cyclic voltammetry at a potential interval of 0.0 V – 2.4 V for PTh and -1.2 V – 0.6 V for PPy at room temperature. During electrochemical deposition, the enzyme was entrapped within the matrix. After construction, enzyme electrodes were kept at 4 °C in a buffer solution.

### 2.3. Enzyme Activity Assays and Kinetic Characterization

Immobilized INV activities were determined using the Somogyi-Nelson method [17] in which different

concentrations of sucrose were prepared, after immersing enzyme electrodes at certain times, Nelson's and arsenomolibdate reagents were added to form a complex compound with the enzymatic reaction product. Activities of immobilized PPO were obtained by Besthorn's Hydrazone method [18]. Different concentrations of catechol were prepared, after adding MBTH reagent, the enzyme electrode was immersed at certain times. Quinone products react with MBTH to form a complex compound. Enzyme activities were calculated by reaction rates of enzymatic reaction. Kinetic parameters of enzyme electrodes; maximum enzyme activity,  $V_{max}$  and Michaelis-Menten constant,  $K_m$  were obtained at optimum pH and 25 °C by using the Michaelis-Menten method and Lineweaver-Burk graphics [19].

#### 2.4. Optimizations and Stability Studies

To find out optimum pH and temperature, electrode activities were measured by changing pH between 2 and 12 for INV, between 4 and 9 for PPO, and changing incubation temperature between 10 °C and 80 °C. The stability of enzyme electrodes was investigated by sequential 40 and 20 activity measurements for INV and PPO respectively. Measurements were performed at a substrate concentration of 5  $K_m$ .

#### 2.5. Determination of Polyphenols in Tea Extracts

Tea extracts were prepared as follows: 5.0 g tea leaves or 5.0 g tea bag was put in a beaker, 200 mL boiling water was poured and the mixture was placed into a 70 °C water bath for 10, 20, 30, and 40 min. infusion time. A sample of 5 mL extract was drawn at each infusion time, diluted by 1:3, and the enzyme activity procedure was applied. The calibration curve was drawn by applying the same procedure to catechol standards. The concentration of total polyphenolics in tea extracts was expressed as mg/mL catechol equivalent. Folin Ciocalteu method was used as a control method [20]. The method was adapted to catechol and the calibration curve was prepared by catechol standards having concentrations between 0.1 and 2.0 mg/mL. First, 40  $\mu$ L of the standard solution was drawn, 3.16 mL water, and 200  $\mu$ L Folin-Ciocalteu reagent were added. Then, the solution was mixed and 600  $\mu$ L 20%  $\text{Na}_2\text{CO}_3$  solution was added. After mixing and waiting for 2 hrs, absorbances were measured at 765 nm to form the calibration curve. The same procedure was applied to 40  $\mu$ L tea extract samples and the total amount of

polyphenolics was represented as mg/mL catechol equivalent.

### 3. Results and Discussion

CF electrodes SEM photos are shown in Figure 1. The diameters of bare and composite polymer-coated CFs are 8.22  $\mu$ m and 55.35  $\mu$ m respectively. The upper two photos belong to bare CF and the middle two belong to coated CF which has a typical cauliflower morphology. The lower micrograph shows the enzyme immobilized biosensor.

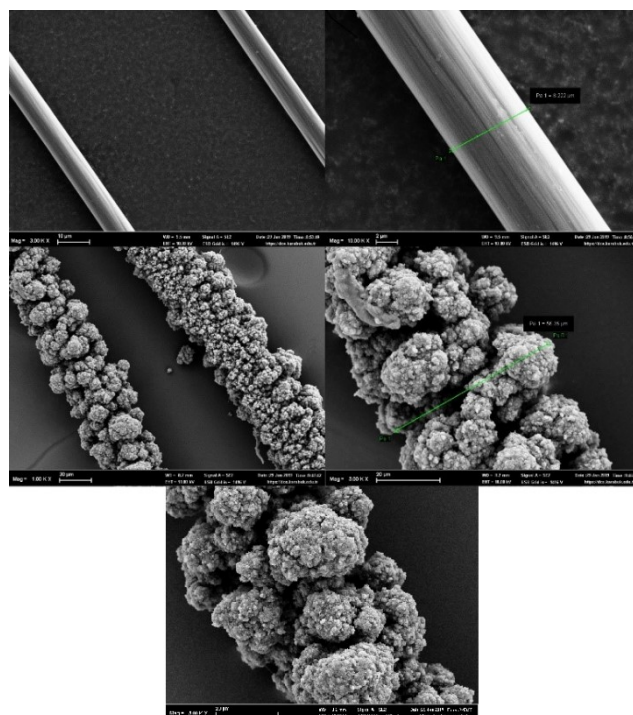


**Figure 1.** SEM micrographs of bare CF, coated CF, and the electrode with the immobilized enzyme.

Kinetic characterization of INV and PPO electrodes prepared by composite material (CF/PTh-PPy/INV and CF/PTh-PPy/PPO) was performed by Lineweaver-Burk graphics presented in Figures 2 and 3 and related kinetic parameters are given in Table 1. CF/PPy/INV and CF/PPy/PPO are the electrodes where the enzyme is immobilized to the PPy matrix [21] and their data was added to Table 1 for comparison.

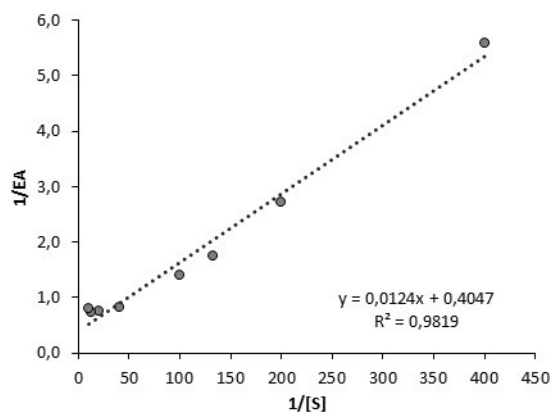


**Figure 2.** Lineweaver-Burk plot of CF/PTh-PPy/INV Electrode.

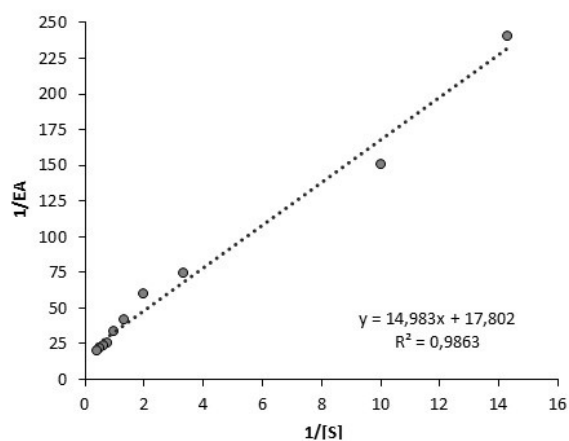


**Figure 3.** Lineweaver-Burk plot of CF/PTh-PPy/PPO electrode.

As shown in Table 1, the maximum activity of the immobilized enzyme,  $V_{max}$  is much lower than the  $V_{max}$  of the free enzyme as expected. This is a general trend for immobilized enzymes arising from a substrate diffusion barrier created by immobilizing matrix. In the comparison of the PPy matrix which was studied in our previous work and PTh-PPy composite material, it is observed that  $V_{max}$  of immobilized enzyme in composite material is three times higher than  $V_{max}$  of immobilized enzyme in PPy matrix that is related with the polymers specific surface area and porosity. When Michaelis-Menten constants are compared to each other, it is seen that  $K_m$  of immobilized enzyme is higher than  $K_m$  of free enzyme.  $K_m$  shows affinity and lower  $K_m$  means higher affinity between enzyme and its substrate. The free enzymes can meet with the substrate molecules easily when they both exist freely in the solution. An increase in  $K_m$  for immobilized enzyme means that the enzyme and its substrate have difficulty at becoming together and the extent of increase is directly related to the

microenvironment where the enzymatic reaction takes place. Immobilized enzyme generally exhibits larger  $K_m$  values compared to the free enzyme, which points that there is tardiness in the diffusion of the substrate into the reaction space when the enzyme is immobilized into a matrix. On the other hand, in comparison PPy and PTh-PPy composite matrices, it is noticed that the  $K_m$  value of immobilized enzyme into PTh-PPy is higher than that of PPy matrix [21-24].

**Table 1.** Kinetic parameters, optimum pH and the temperature of free and immobilized INV and PPO.

	$V_{max}$	$K_m$ (mM)	Opt. pH	Opt. Temp.
Free INV <sup>a</sup>	82,30 $\mu\text{mol}/\text{min.mL}$	24,30	4.6	50 °C
CF/PPy/INV electrode <sup>b</sup>	0,779 $\pm$ 0,120 $\mu\text{mol}/\text{min.electrode}$	27,20 $\pm$ 6,70	6.0	40 °C
CF/PTh-PPy/INV electrode	2,471 $\pm$ 0,150 $\mu\text{mol}/\text{min.electrode}$	30,60 $\pm$ 5,30	5.0	60 °C
Free PPO <sup>c</sup>	0,073 $\mu\text{mol}/\text{min.mL}$	4,00	5.0	40 °C
CF/PPy/PPO electrode <sup>d</sup>	0,017 $\pm$ 0,004 $\mu\text{mol}/\text{min.electrode}$	176,00 $\pm$ 26,60	7.0	60 °C
CF/PTh-PPy/PPO electrode	0,056 $\pm$ 0,090 $\mu\text{mol}/\text{min.electrode}$	842,00 $\pm$ 32,03	8.0	-

<sup>a</sup>[22], <sup>b</sup>[20], <sup>c</sup>[21,23], <sup>d</sup>[20]

The effect of pH on the activity of immobilized INV into PTh-PPy composite matrix is illustrated in Figure 4. In a previous study, the pH at which maximum activity was observed for the free enzyme was found to be 4.6 [23]. The immobilized enzyme within PTh-PPy composite matrix revealed a maximum activity at pH 5.0, a very close value to the free enzyme. pH 5.0 was used throughout the optimization and characterization studies of the CF/PTh-PPy/INV electrode.

The temperature influence on enzyme activity of immobilized INV within the PTh-PPy composite matrix was investigated and the maximum activity was observed at 60 °C. Enzyme activity rises slightly up, reaches a maximum, then declines sharply. Enzyme loses its activity completely at 70 °C as a result of temperature-induced denaturation of protein structure. The temperature of maximum activity of free INV was given as 50 °C by Alkan et al. [23] and that of PPy immobilized INV was found as 40 °C in our previous study [21]. Optimum temperature higher than free and PPy immobilized INV indicates a more protective structure of PTh-PPy composite material than PPy matrix concerning temperature stability.

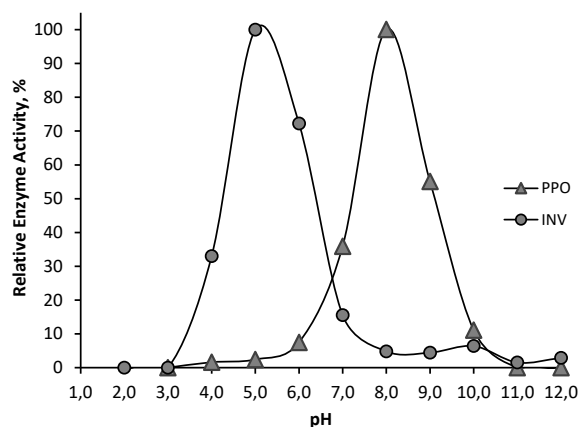


**Figure 4.** pH effect on CF/PTh-PPy/INV and CF/PTh-PPy/PPO electrodes activity.

According to the study performed by Kiralp et al., free PPO revealed a maximum activity at pH 5.0 [24]. The pH influence on enzyme activity of PPO immobilized within the PTh-PPy composite matrix is represented in Figure 4 and maximum activity is exhibited at a pH of 8.0. In our previous study, the maximum activity of immobilized PPO within the PPy matrix was given as 7.0 [21]. Results indicate a significant enhancement in enzyme stability towards the basic pHs upon immobilization. The reason for that, as explained by Erginer et al., could be the effect of charge distribution on the enzyme in the microenvironments of the composite matrix [25]. Throughout the studies, pH 7.0 was used for CF/PTh-PPy/PPO electrode.

Stability studies of enzyme electrodes show that immobilized INV is quite stable until the 40<sup>th</sup> measurement as shown in Figure 5a. On the other hand, immobilized PPO shows a rather alternating behavior as compared to INV that activity is relatively stable between 80 % and 100 % as seen in Figure 5b.

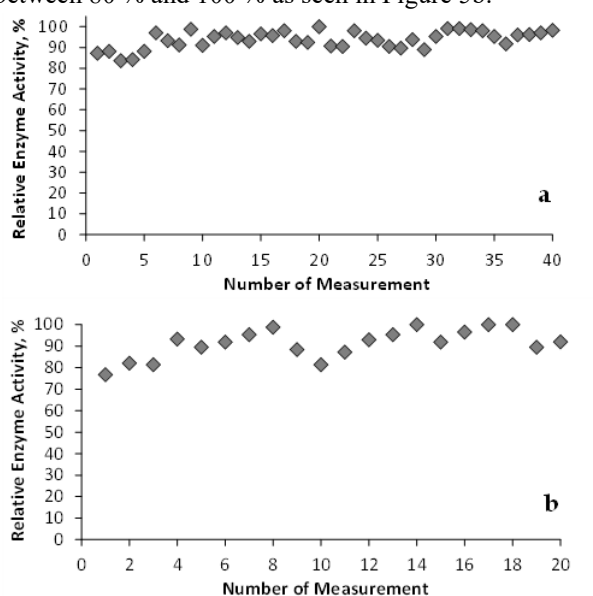


**Figure 5.** Operational stability of CF/PTh-PPy/INV (a) and CF/PTh-PPy/PPO (b) electrodes.

CF/PTh-PPy/PPO electrode was applied to the analysis of polyphenolic substances in tea extracts by using a calibration curve ( $y=0.3265x+0.0202$ ,  $R^2=0.9930$ ) prepared with catechol standards in concentration between 0.007 and 1.600 mg/mL. LOD was found as 0.037 mg/mL. The results with changing brewing times are given in Table 2.

The amount of polyphenolic substance infused into the water increases between 10 and 20 minutes. However, it stays constant at 30 min and 40 min infusion times. Therefore, 20 min is sufficient infusion time to obtain the maximum amount of phenolics in the extraction solvent, which are 0.641 mg/mL and 1.450 mg/mL for tea leaves and tea bags respectively.

The results were confirmed by the Folin Ciocalteu method of analysis. A calibration curve was drawn by different catechol standards ( $y=1.0998x+0.0704$ ,  $R^2=0.9944$ ). The results obtained in different brewing times are shown in Table 2.

**Table 2.** Total polyphenolics determined by CF/PTh-PPy/PPO electrode and the Folin Ciocalteu method as mg/mL catechol equivalent.

	Samples Brewing Time (min)				
	10	20	30	40	
					Analysis by
<b>Total Polyphenols</b>	0.053	0.641	0.614	0.669	Enzyme Electrode
<b>(mg/mL), Tea Leaves</b>	0.515	0.702	0.627	0.740	Analysis by Folin
					Ciocalteu Method
					Analysis by
<b>Total Polyphenols</b>	1.156	1.450	1.468	1.533	Enzyme Electrode
<b>(mg/mL), Tea Bag</b>	0.562	1.148	1.055	1.180	Analysis by Folin
					Ciocalteu Method

The optimum extraction time is 20 min similar to previous results obtained by CF/PTh-PPy/PPO electrode. There is no increase in the number of polyphenolics with increasing brewing time after 20 min. 0.702 mg/mL and 1.148 mg/mL are the maximum amounts of phenolic substances extracted from tea leaves and tea bags with 20 min infusion time.

#### 4. Conclusion

Construction of novel CF enzyme electrodes modified with conducting PTh-PPy composite was achieved via electrochemical polymerization. Produced biosensors were characterized in terms of kinetic parameters. Composite-based CF enzyme electrodes revealed higher  $V_{max}$  and  $K_m$  values compared to PPy based CF enzyme electrodes due to the morphological differences. An increase in the maximum enzyme activity

means more enzymes immobilized in that matrix, which indicates that composite material has a more porous structure than the PPy matrix and holds more enzymes. Higher  $K_m$  means that cavities on the PTh-PPy surface are deeper than that on the PPy surface, which makes it less easy to meet enzyme and substrate on the PTh-PPy matrix. This situation is observed for both INV and PPO enzymes. Regarding the optimization studies, composite-based INV electrodes exhibited an optimum pH almost the same as a free enzyme which means that PTh-PPy matrix does probably not affect the charge distribution significantly on immobilized INV enzyme. CF/PTh-PPy/PPO electrodes optimum pH value is much higher than optimum pH of free enzyme. During oxidative electropolymerization, negatively charged dopant ions are received into the polymer structure. In micro spaces within the matrix, these dopant ions make the protons accumulate around the enzymes and protect them against hydroxide ions. This situation may cause a difference between the pH around the immobilized enzyme and the pH of the bulk. The increase in optimum temperature upon immobilization into PTh-PPy implies the protective environment supplied by PTh-PPy composite matrix against higher temperatures. With these advantages, CF/PTh-PPy/PPO electrode offers a cheaper and more practical alternative to conventional methods. As a conclusion, it is proposed to be used for the determination of phenolic substances, particularly in food samples and environmental waters.

### Acknowledgments

The authors gratefully thank Prof. Dr. Sadi Sen for his valuable contribution to this study and acknowledge Karabuk University Scientific Research Funds for the financial support with the project number KBUBAP-13/2-YL-034.

### Declaration of Ethical Standards

The authors of this article declare that the materials and methods used in this study do not require ethical committee permission and/or legal-special permission.

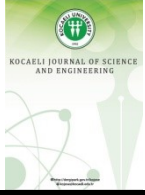
### Conflict of Interest

The authors declare that they have no known competing financial interests or personal relationships that could have appeared to influence the work reported in this paper.

### References

- [1] Fei J., Wu K., Wang F., Hu S., 2005. Glucose nanosensors based on redox polymer/glucose oxidase modified carbon fiber nanoelectrodes. *Talanta*, **65**, pp. 918-924.
- [2] Taylor I.M., Robbins E.M., Catt K.A., Cody P.A., Happe C.L., Cui X.T., 2017. Enhanced dopamine detection sensitivity by PEDOT/graphene oxide coating on in vivo carbon fiber electrodes. *Biosensors and Bioelectronics*, **89**, pp. 400-410.
- [3] Salazar P., Martin M., O'Neill R.D., Gonzalez-Mora J.L., 2016. Glutamate microbiosensors based on Prussian Blue modified carbon fiber electrodes for neuroscience applications: In vitro characterization. *Sensors and Actuators B: Chemical*, **235**, pp. 117-125.
- [4] Ferreira N.R., Ledo A., Laranjinha J., Gerhardt G.A., Barbosa R.M., 2018. Simultaneous measurements of ascorbate and glutamate in vivo in the rat brain using carbon fiber nanocomposite sensors and microbiosensor arrays. *Bioelectrochemistry*, **121**, pp. 142-150.
- [5] Kim J.H., Cho S., Bae T.S., Lee Y.S., 2014. Enzyme biosensor based on an N-doped activated carbon fiber electrode prepared by a thermal solid-state reaction. *Sensors and Actuators B: Chemical*, **197**, pp. 20-27.
- [6] Yuan C.J., Wang C.L., Wu T.Y., Hwang K.C., Chao W.C., 2011. Fabrication of a carbon fiber paper as the electrode and its application toward developing a sensitive unmediated amperometric biosensor. *Biosensors and Bioelectronics*, **26**, pp. 2858-2863.
- [7] Nadaroglu H., Mosber G., Alayli Gungor A., Adiguzel G., 2019. Biodegradation of some azo dyes from wastewater with laccase from *Weissella viridescens* LB37 immobilized on magnetic chitosan nanoparticles. *Journal of Water Process Engineering*, **31**, 100866.
- [8] Nambiar S., Yeow J.T.W., 2011. Conductive polymer-based sensors for biomedical applications. *Biosensors and Bioelectronics*, **26**, pp. 1825-1832.
- [9] Park C.S., Lee C., Kwon O.S., 2016. Conducting polymer based nanobiosensors. *Polymers*, **8**, 249, pp. 1-18.
- [10] Sarma A.K., Vatsyayan P., Goswami P., Minter S.D., 2009. Recent advances in material science for developing enzyme electrodes. *Biosensors and Bioelectronics*, **24**, pp. 2313-2322.
- [11] Adeloju S.B., Moline A.N., 2001. Fabrication of

- ultra-thin polypyrrole-glucose oxidase film from supporting electrolyte-free monomer solution for potentiometric biosensing of glucose. *Biosensors and Bioelectronics*, **16**, pp. 133-139.
- [12] Besombes J.L., Cosnier S., Labbe P., 1997. Improvement of poly(amphiphilic pyrrole) enzyme electrodes via the incorporation of synthetic laponite-clay-nanoparticles. *Talanta*, **44**, pp. 2209-2215.
- [13] Borochoy-Neori H., Judeinstein S., Tripler F., Harari M., Greenberg A., Shomer I., Holland D., 2009. Seasonal and cultivar variations in antioxidant and sensory quality of pomegranate (*Punica granatum L.*) fruit. *Journal of Food Composition and Analysis*, **22**, pp. 189-195.
- [14] Tagliazucchi V., Verzelloni E., Bertolini D., Angela C., 2010. In vitro bio-accessibility and antioxidant activity of grape polyphenols. *Food Chemistry*, **120**, pp. 599-606.
- [15] Del Rio D., Costa L.G., Lean M.E.G., Crozier A., 2010. Polyphenols and health: What compounds are involved? *Nutrition, Metabolism and Cardiovascular Diseases*, **20**, pp. 1-6.
- [16] Apetrei C., Rodriguez-Mendez M.L., De Saja J.A., 2011. Amperometric tyrosinase based biosensor using an electropolymerized phosphate-doped polypyrrole film as an immobilization support. Application for detection of phenolic compounds. *Electrochimica Acta*, **56**, pp. 8919- 8925.
- [17] Nelson N., 1944. A photometric adaptation of Somogyi method for the determination of glucose. *Journal of Biological Chemistry*, **153**, pp. 375-380.
- [18] Pifferi P.G., Baldassari L., 1973. A spectrophotometric method for the determination of catecholase activity of tyrosinase by Besthorn's hydrazone. *Analytical Biochemistry*, **52**, pp. 325-335.
- [19] Lineweaver H., Burk D., 1934. The determination of enzyme dissociation constants. *Journal of the American Chemical Society*, **56**, pp. 658-666.
- [20] Singleton V.L., Orthofer R., Lamuela-Raventos R., 1999. Analysis of total phenols and other oxidation substrates and antioxidants by means of Folin-Ciocalteu reagent. *Oxidants and Antioxidants Part A Book Series: Methods in Enzymology*, Volume 299, 152-178, 1<sup>st</sup> ed. Academic Press, United States.
- [21] Karabacak G., 2019. İnvertaz ve polifenol oksidaz enzimleriyle oluşturulan karbon fiber enzim elektrotları. MSc Thesis, Graduate Enstitute, Karabük University, Karabük.
- [22] Büyükbayram A.E., Kıralp S., Toppare L., Yağcı Y., 2006. Preparation of biosensors by immobilization of polyphenol oxidase in conducting copolymers and their use in determination of phenolic compounds in red wine. *Bioelectrochemistry*, **69**, pp. 164-171.
- [23] Alkan S., Toppare L., Yağcı Y., Hepuzer Y., 1999. Immobilization of invertase in conducting thiophene-capped poly(methyl methacrylate)/polypyrrole matrices. *Journal of Biomaterials Science, Polymer Edition*, **10**, pp. 1223-1235.
- [24] Kıralp S., Toppare L., Yagci Y., 2003. Immobilization of polyphenol oxidase in conducting copolymers and determination of phenolic compounds in wines with enzyme electrodes. *International Journal of Biological Macromolecules*, **33**, pp. 37-41.
- [25] Erginer R., Toppare L., Alkan S., Bakır U., 2000. Immobilization of invertase in functionalized copolymer matrices. *Reactive and Functional Polymers*, **45**, pp. 227-233.



## Effect of Pylon Shapes on Seismic Response of a Long-Span Steel Box-Girder Cable-Stayed Bridge

N.Sonjoh CHEBELEM<sup>1</sup> , Hakan ERDOĞAN<sup>2,\*</sup> 

<sup>1</sup> Department of Civil Engineering, Kocaeli University, Kocaeli, 41001, Turkey, **ORCID:** 0000-0002-1739-3774

<sup>2</sup> Department of Civil Engineering, Kocaeli University, Kocaeli, 41001, Turkey, **ORCID:** 0000-0002-7241-7652

### Abstract

#### Article Info

#### Research paper

Received : April 04, 2021

Accepted : June 22, 2021

#### Keywords

Cable-Stayed Bridge  
Pylon Type  
Time-History Analysis  
Seismic Response  
Steel Box-Girder

In recent decades, the demand for complex and economical engineering structures with great aesthetics has been on the rise and the cable stayed bridges also take their share of this interest. Besides many advantages cable-stayed bridges are quite flexible, hence susceptible mainly to dynamic actions such as impact loads, wind effects and seismic excitations. In this context, this study focused on the effect of A and H shape reinforced concrete pylons on the seismic behavior of a long span steel triple box-girder cable-stayed bridge that was presumed to be located in an earthquake-prone region in Turkey. The 3D models of the bridge were constructed using SAP2000 software and the time history analysis have been carried out considering cable sag, large displacement effects. The seismic responses of the bridges are compared in terms of axial force on cables, deflections on the pylons and the deck.

### 1. Introduction

Cable-stayed bridges have become more popular especially in seismic prone areas over the past decades. This popularity is directly related to the massive improvement in technological know-how in terms of material quality, powerful computation tools and construction strategies. The use of cable-stayed bridges dates back to 16<sup>th</sup> century. But, after the Second World War, cable-stayed bridges gained more prominence with the first modern steel cable-stayed bridge of 183 m main span constructed in Sweden in 1955. Evolution of this form of bridge over the years has been tremendous. Today, the main span length of cable-stayed bridges exceeded 1000 meters. The Russky Bridge in Vladivosstok has the longest main span length (1104m) in the world. Cable-stayed bridges are generally compared with suspension bridges. Though very similar, cable-stayed bridges have a

major distinctive difference from suspension bridges. The stay-cables in the cable-stayed bridges travel directly from the tower to the anchorage point on the deck girder at an angle less than 90° (between 20°-60°) creating a fan-like or harp-like cable pattern. Meanwhile, for the suspension bridge cables, they generally run vertically on the deck attached to a main cable placed horizontally from tower to tower through the bridge structure. The main advantages of the cable-stayed form over suspension bridges can be listed as the increased rigidity, lower deformation and rapid construction. On the other hand, cables are the primary load-bearing members in cable-stayed bridges and extra strain induced on the cables deserves special care during the design stage especially under dynamic excitations such as wind load and seismic actions.

Several studies were conducted on the seismic behavior of cable-stayed bridges over the last decades [1-26]. These studies revealed that the flexibility and susceptibility of the bridge is dependent on many factors such as the main span of the bridge, the cable pattern, the support conditions at the piers, the damping type, material

\* Corresponding Author: [hakan.erdogan@kocaeli.edu.tr](mailto:hakan.erdogan@kocaeli.edu.tr)



properties, soil-structure interaction, etc. The shape of the pylons are assumed to be an aesthetic feature as the effects of pylon shapes are not so prominent for structural design of short span cable-stayed bridges. However, it is imperative to use certain pylon shapes in case of long span cable-stayed bridges in order to satisfy structural safety [27-30]. Accordingly, this study examined the effect of two different pylon shapes of a long span cable-stayed bridge that is postulated to span the Izmit Bay in Kocaeli, Turkey.



**Figure 1.** Location of the Cable-Stayed Bridge (Google Earth ©2020 Google, ©2020 Basarsoft, Image©2020 Maxar Technologies)

## 2. Materials and Method

### 2.1. Description of the Bridge

Cable-stayed bridges are generally made of three

major parts which are cables, pylon and deck. The proposed cable-stayed bridge was assumed to be spanning the Izmit Bay and linking the Derince District to Gölcük District (Figure 1). The location of the bridge was decided considering the shorter route between both districts. It should be noted that this region is densely occupied by industrial facilities along the banks of İzmit Bay on both sides. Hence, the bridge will serve to decongest the traffic and create ease of interaction between these two districts. Also, along this route the deepest point below sea level is approximately 50 m with an average gradient of 4% from shore to deepest point which creates a quiet shallow and short route linking both districts [31]. Nevertheless, Izmit Bay, which is situated along an urbanized and industrialized coastal line of the Marmara Sea, lies on the Northern Anatolian fault (Strike Slip fault) which suffered a major rupture lastly on August 17th, 1999 with a registered magnitude of  $M_w = 7.4$

The overall span length of the bridge is 2000 m consisting of a main span of 1200 m, side spans of 400 m and two pylons with 78 stay cables on each side of a pylon. Intermediary piers are placed 80 m away from each other at the side span. The heights of the pylons vary due to the inclination of the bridge deck (Figure 2). The deck of the bridge is inclined along the longitudinal direction with a slope of 2.5% to compensate for the sag effect of the cables and the mid-span moment of the deck due to self-weight. In addition, this inclination allows a clear passage for sea vessels such as ships envisaged to go under the structure.

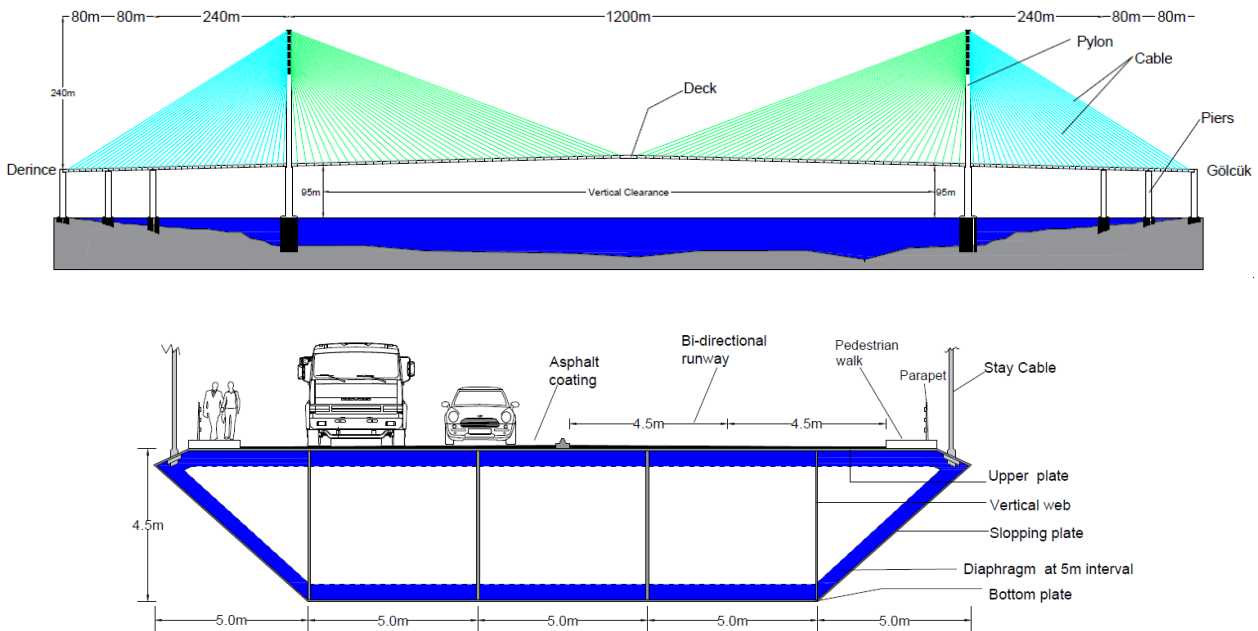


**Figure 2.** Side view of the bridge and the cross-section details of the bridge deck.



The deck is connected to the pylons by 0.15 m diameter galvanized high tension steel cables spaced at 10 m for side span and 15 m for main span from each other (Figure 2)

The deck of the bridge is a trapezoidal triple box steel girder with a maximum height of 4.50 m as shown in Figure 2. The deck width was decided to be 25 m for two bi-directional lanes with pedestrian walks on both sides. The height to span ratio of the bridge is relatively high compared to the other examples in the literature. The equivalent thickness of upper and lower orthotropic steel plates and the sloping base plates of the deck were assumed to be 20 mm considering the trapezoidal stiffeners. The equivalent thickness of the web is 30 mm including the trapezoidal stiffeners. Transversal steel cross beams were provided to restrict distortional effects in every 5 meters along the deck.

Even though other parameters such as the deck and pylon cross-section, deck-pier connection type, pylon – deck connection type etc. may affect the behavior of the cable-stayed bridge, an illustration of the dynamic response of a long span cable-stayed bridge was predominantly demonstrated through the variation of the pylon shape. The emphasis was laid on the shape of the pylon as the other aspects were assumed to be identical for the sake of accurate comparison.

The commonly used A and H shaped pylons were taken into consideration in the scope of this study (Figure 3). The pylon cross sectional dimensions were determined considering a preliminary design procedure prescribed in the literature [20].

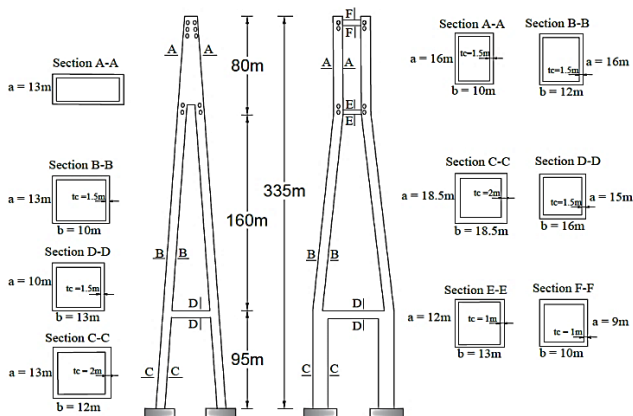


Figure 3. Dimensions of the A and H shape reinforced concrete pylons.

## 2.2. Material Properties

Self-compacting concrete with compressive strength of 80 MPa was preferred in the design of pylons and piers. The cable strands were galvanized and provide

higher tensile strength with respect to regular steel. These strands with a nominal diameter of 15.7 mm, consist of seven helical wires. The characteristic tensile strength of strands is 1860 MPa. Material nonlinearity has not been taken into consideration throughout the analysis; all the components were assumed to behave in a linear-elastic manner.

## 2.3. Finite Element Model of the Bridge

Structural analysis software SAP2000 [32] was used to create the finite element model of the bridge. Pylons and piers were considered as fixed at the bottom, deck-pylon connection considered as partially fixed with movement predominantly in the horizontal x-direction linked by viscous dampers and elastomeric bearings in order to mimic the actual behavior. The cable element uses an elastic catenary formulation to represent the behavior of a slender member under self-weight. This catenary cable element is highly nonlinear and inherently accounts for P-Δ effect and large displacement. The deck was modelled using shell elements. Frame elements were used to define pylons, struts and transverse cross-beams. 3-D finite element model of cable-stayed bridge with A-shape pylon is shown in Figure 4.

## 2.4. Dynamic Characteristics of Bridges

The modal behavior of the cable stayed bridges should be evaluated in detail to study seismic behavior of such structures. For this purpose, an initial dead load analysis was performed considering the geometric nonlinearity. Then, pretension was applied to the cables considering the deflected shape under dead load. Finally, Ritz vectors modal analysis was carried out to investigate the dynamic characteristics of the bridge. First six vibration modes and corresponding natural periods for bridges with A and H shape pylons are listed in Table 1 and mode shapes are displayed in Figure 5 for comparison purposes.

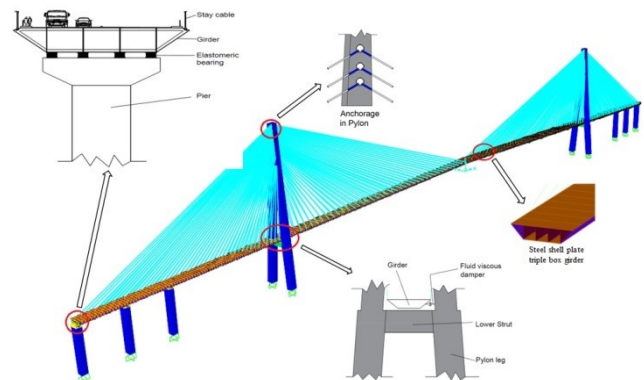
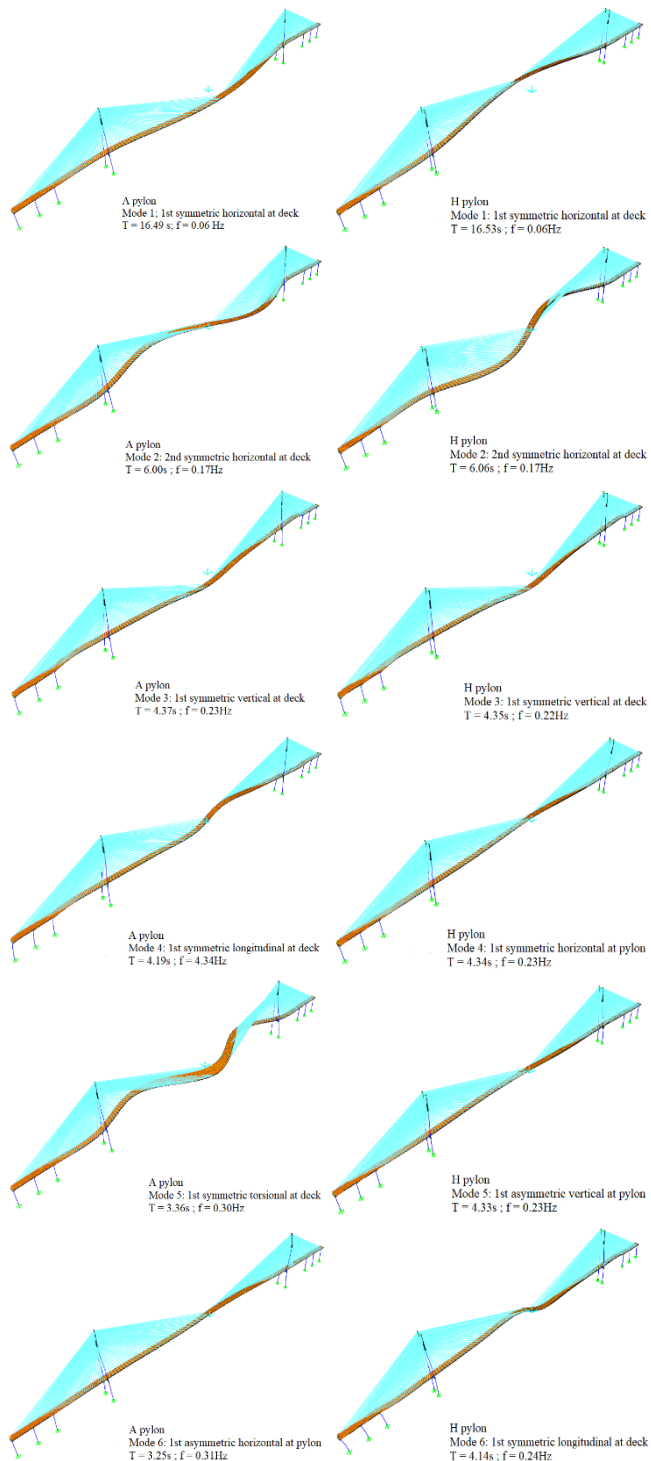


Figure 4. 3-D finite element model of the bridge with A-shape pylon



**Figure 5.** First six fundamental modal shapes of the bridge models

First three fundamental vibration modes are identical for both pylon types and vibration periods are very close to each other. The tower vibration become dominant at 4<sup>th</sup> fundamental mode for H-shape pylon which is relatively earlier with respect to A-shape pylon. There is a difference in the number of vibration modes to attain a 95% mass participation ratio for two models. This difference can be attributed to the type of pylon

shape. The variation of cumulative modal mass participation factor with respect to number of modes is shown in Figure 6.

**Table 1.** Comparison of natural periods and mode shapes

Mode No	A-Shape Pylon		H-Shape Pylon	
	Period (sec)	Mode Shape	Period (sec)	Mode Shape
1	16.49	1 <sup>st</sup> S-H Deck	16.54	1 <sup>st</sup> S-H Deck
2	6.00	2 <sup>nd</sup> S-H Deck	6.06	2 <sup>nd</sup> S-H Deck
3	4.37	1 <sup>st</sup> S-V Deck	4.35	1 <sup>st</sup> S-V Deck
4	4.19	1 <sup>st</sup> S-L Deck	4.34	1 <sup>st</sup> S-H Pylon
5	3.36	1 <sup>st</sup> S-T Deck	4.33	1 <sup>st</sup> A-H Pylon
6	3.25	1 <sup>st</sup> A-H Pylon	4.14	1 <sup>st</sup> S-L Deck

S: symmetric, A: asymmetric, H: horizontal, V: vertical, L: longitudinal T: torsional

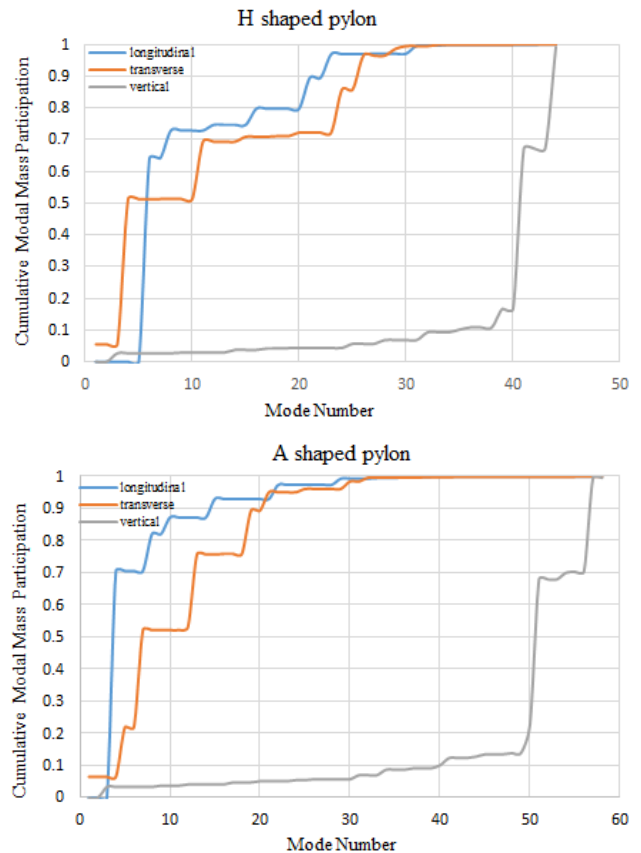


**Figure 6.** Modal mass participation ratio vs. number of modes in three principal directions for both pylon types

### 2.5. Time History Analysis of Bridge Models

Time history analysis was carried out to investigate the seismic response of the bridge models with different pylon shapes. Two types of geometric nonlinearity, namely p-delta effects and nonlinearity due to cable sag were considered. Kocaeli Earthquake in 1999 was the major earthquake of the near past in the neighborhood of the bridge location. Therefore, all three components (North-South, East-West and Vertical) of the Kocaeli Earthquake record from the closest station (Yarimca YPT) were used for the time-history analysis. Figure 7 shows the acceleration response spectra of the 1999 Kocaeli Earthquake.

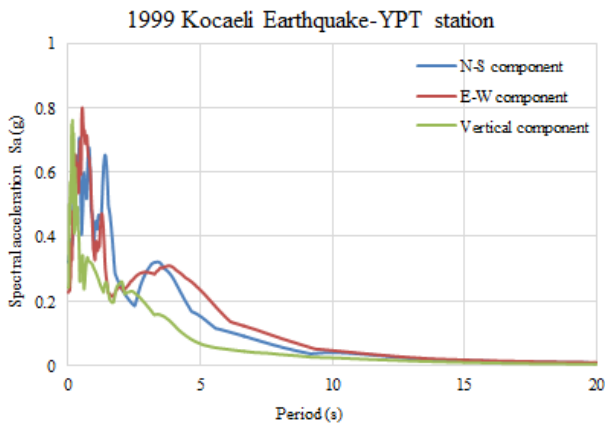


**Figure 7.** Spectral acceleration of 1999 Kocaeli earthquake in the three orthogonal directions

The direct-integration method was employed in the nonlinear time history analysis due to its capability to perform nonlinear direct-integration time-history analysis. In SAP2000 [32], different numerical solution algorithms are available for performing the nonlinear direct-integration time-history analysis. The "Hilber-Hughes-Taylor alpha" (HHT) method was utilized in this study to conduct the nonlinear time history analysis. The time interval employed for this numerical simulation is 0.01 second. The damping of structure was idealized by Rayleigh damping model. The effective viscous damping of the overall system was assumed to be 2% at period values of 0.11 second and 16.5 second considering the higher modes. Gravity load from the self-weight of the bridge was initially applied prior to time history analysis to simulate the actual behavior.

### 3. Results and Discussion

The seismic responses of the bridges are compared in terms of axial force on cables, deflections on the pylons and the deck. Figure 8 shows the axial load variation in the heavily loaded cables for different pylon

shapes. The maximum axial force was observed for the bridge with H-shape pylon. However, the effect of pylon type on the maximum cable force is not very significant for the current study.

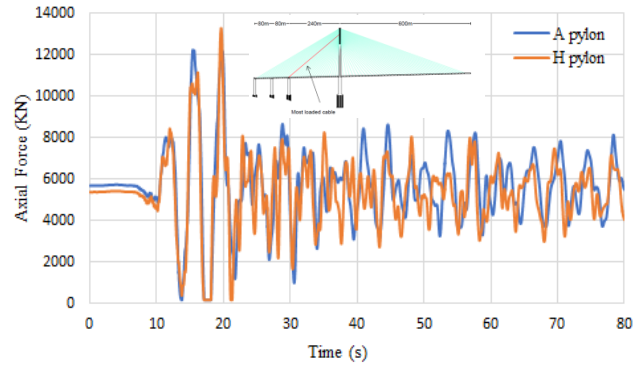


**Figure 8.** Axial force variation for the critical cable

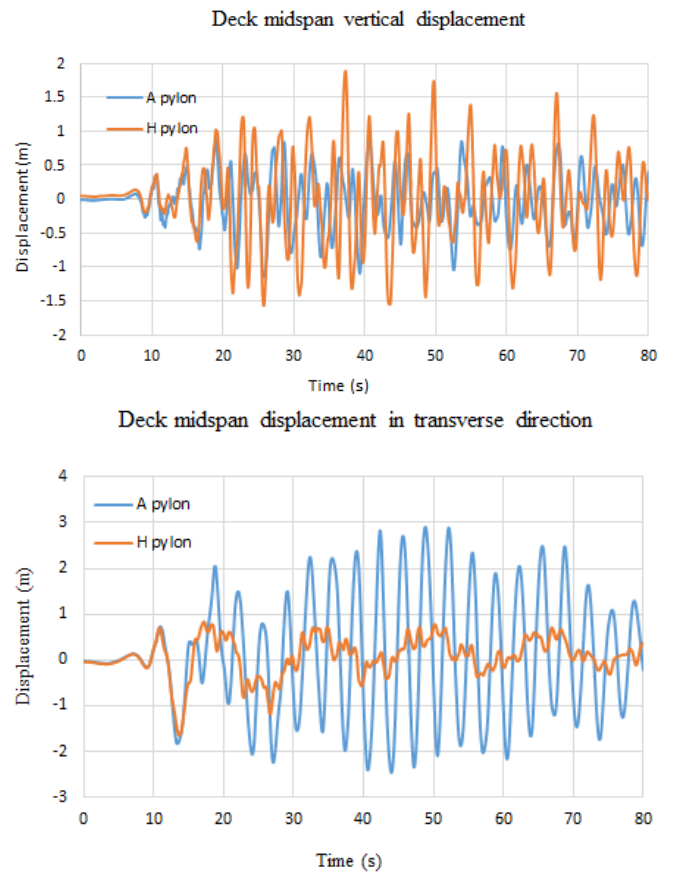


**Figure 9.** Comparison of Deck Midspan Displacement

The deck midspan displacement in vertical and transverse direction are presented in Figure 9 for two different bridge models. The analysis results indicated that midspan vertical displacement is relatively greater in bridge with H-shape than bridge with A-shape pylon. On the other hand, significant difference was observed in terms of deck midspan deflection response in the transverse direction. The amplitude of transverse

midspan displacement is almost equal to 3 meters for the cable-stayed bridge with A-shape pylon.

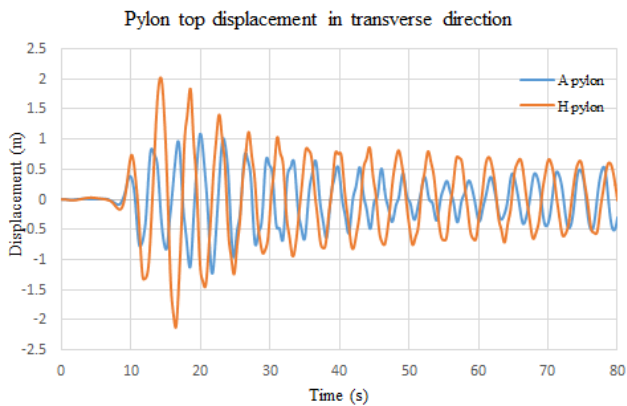


**Figure 10.** Pylon Top Displacement in Transverse Direction

Figure 10 displays the effect of pylon shape on the pylon top displacement in transverse direction. The analysis results revealed that the maximum transverse displacement of the H-shape pylon top is almost two times greater than that of the A-shape pylon.

#### 4. Conclusions

In this study, the effect of A and H-shape pylons on the seismic behavior of a long span steel triple box-girder cable-stayed bridge that was assumed to be located in an earthquake prone region was investigated. Only geometric nonlinearities were taken into account throughout the analysis and the bridge models were analyzed considering the effect of dead loads, cable pretension forces and seismic excitation. The cross-section dimensions of the reinforced concrete pylons were decided considering a preliminary design procedure prescribed in the literature. The pylon vibration become dominant in the earlier modes for H-shape pylon with respect to A-shape pylon. This behavior possibly led to almost two-fold difference among the maximum pylon top transverse displacements of the two different pylons, namely H-shape pylon experienced greater displacement. On the contrary, the maximum deck midspan transverse displacement was observed in cable-stayed bridge model with A-shape pylon. It should also be emphasized that the pylon shape has almost no significant effect on the axial load variation on the most critical cable for the current study.

#### Declaration of Ethical Standards

The author(s) of this article declare that the materials and methods used in this study do not require

ethical committee permission and/or legal-special permission.

#### Conflict of Interest

The authors declare that they have no known competing financial interests or personal relationships that could have appeared to influence the work reported in this paper.

#### References

- [1] Fleming J.F., Egeseli E.A., 1980. Dynamic Behaviour of a Cable-Stayed Bridge. *Earthquake Engineering and Structural Dynamics*, **8**, pp. 1-16.
- [2] Nazmy A.S., Abdel-Ghaffar A.M., 1990. Non-linear Earthquake-Response Analysis of Long-Span Cable-Stayed Bridges: Theory. *Earthquake Engineering & Structural Dynamics*, **19**(1), pp. 45-62.
- [3] Wilson, J.C., Gravelle W., 1991. Modelling of a Cable-Stayed Bridge for Dynamic Analysis. *Earthquake Engineering and Structural Dynamics*, **20**, pp. 707-721.
- [4] Nazmy A.S., Abdel-Ghaffar A., 1992. Effects of Ground Motion Spatial Variability on the Response of Cable-Stayed Bridges. *Earthquake Engineering and Structural Dynamics*, **21**(1), pp. 1-20.
- [5] Betti R., Abdel-Ghaffar A., Niazzy A., 1993. Kinematic Soil-Structure Interaction for Long-Span Cable Supported Bridges. *Earthquake Engineering and Structural Dynamics*. 1993, **22**, pp. 415-430.
- [6] Filiatrault A., Tinawi R., Massicotte B., 1993. Damage to Cable-Stayed Bridge During 1988 Saguenay Earthquake. I: Pseudostatic Analysis. *Journal of Structural Engineering*, **119**(5), pp. 1432-1449.
- [7] Ali H., Ghaffar A., 1995. Seismic passive control of cable-stayed bridges. *Journal of Shock and Vibration*, **2**(4), pp. 259-272.
- [8] Zheng J., Takeda T., 1995. Effects of Soil-Structure Interaction on Seismic Response of PC Cable-Stayed Bridge. *Soil Dynamics and Earthquake Engineering*, **14**(6), pp. 427-437.
- [9] Tuladhar R., Dilger W., Elbadry M., 1995. Influence of Cable Vibration on Seismic Response of Cable - Stayed Bridges. *Canadian Journal of Civil Engineering*. **22**(5), pp. 1001-1020.
- [10] Ren W., Obata M., 1999. Elastic-Plastic Seismic Behaviour of Long-Span Cable-Stayed Bridges. *Journal of Bridge Engineering*, **4**(3), pp. 194-203.

- [11] Tuladhar R., Dilger W., 1999. Effect of Support Conditions on Seismic Response of Cable – Stayed bridges. *Canadian Journal of Civil Engineering*, **26**(5), pp. 631–645.
- [12] Raheem S.E.A., Hayashikawa T., 2003. Parametric Study on Steel Tower Seismic Response of Cable-Stayed Bridges under Great Earthquake Ground Motion. *Structural Engineering / Earthquake Engineering*, **20**(1), pp. 25–41.
- [13] Soneji B.B., Jangid R., 2008. Influence of Soil–Structure Interaction on the Response of Seismically Isolated Cable–Stayed Bridge. *Soil Dynamics and Earthquake Engineering*, 2008, **28**(4), pp.245–257.
- [14] Zhang L., Luo W., Li F., Chang Z., 2011. Seismic Response Analysis of Cable-Stayed Bridge Considering the Interaction of the Soil-Pile Superstructure. *American Society of Civil Engineers, Third International Conference on Transportation Engineering (ICTE)*, Chengdu, China, 23-25 July, pp. 1957-1962.
- [15] Çetindemir O., Akbaş B., Fahjan Y.M., Shen J., 2011. Nonlinear Dynamic Analysis of Long-Span Cable-Stayed Bridges and Modeling Issues,” 2nd Symposium on Bridges and Viaducts, Eskişehir, Turkey, 28-30 September.
- [16] Camara A., Astiz M., 2012. Pushover Analysis for the Seismic Response Prediction of Cable–Stayed Bridges under Multi–Directional Excitation. *Engineering Structures*, **41**, pp. 444–455.
- [17] Soyuluk K., Sicacik E., 2012. Soil–Structure Interaction Analysis of Cable–Stayed Bridges for Spatially Varying Ground Motion components. *Soil Dynamics and Earthquake Engineering*, **35**, pp. 80–90.
- [18] Valdebenito G.E., Aparicio A.C., Alvarez J.J., 2012. Seismic Response of Cable-Stayed Bridges for Different Layout Conditions: A Comparative Analysis. *Proceedings of 15th World Conference on Earthquake Engineering*. Lisboa, Portugal 24-28 September, pp. 10020-10029.
- [19] Camara A., Astiz M., Ye A.J., 2014. Fundamental Mode Estimation for Modern Cable–Stayed Bridges Considering the Tower Flexibility. *Journal of Bridge Engineering*, **19**(6), 04014015.
- [20] Camara A., Astiz M., 2014. Analysis and Control of Cable–Stayed Bridges Subject to Seismic Action. *Structural Engineering International*, **24**(1), pp. 27–36.
- [21] Camara A., Efthymiou E., 2016. Deck–tower Interaction in the Transverse Seismic Response of Cable–Stayed Bridges and Optimum Configurations. *Engineering Structures*, **124**, pp. 494–506.
- [22] Naderian H., Cheung M.S., Shen Z.Y., Dragomirescu E., 2016. Seismic Analysis of Long-Span Cable-Stayed Bridges by an Integrated Finite Strip Method. *Journal of Bridge Engineering*, **21**(3), 04015068.
- [23] Zhong J., Jeon J., Ren W., 2018. Risk assessment for a Long-Span Cable-Stayed Bridge Subjected to Multiple Support Excitations. *Engineering Structures*, **176**, pp. 220-230.
- [24] Wang X., Fang J., Zhou L., Ye A., 2019. Transverse Seismic Failure Mechanism and Ductility of Reinforced Concrete Pylon for Long Span Cable-Stayed Bridges: Model Test and Numerical Analysis, *Engineering Structures*, **189**, pp. 206-221.
- [25] Martins A.M.B., Simões L.M.C., João H.J.O., Negrão, 2019. Optimization of Concrete Cable-Stayed Bridges under Seismic Action, *Computers & Structures*, **222**, pp. 36-47.
- [26] Xie W., Sun L., 2021. Transverse Seismic Response and Failure Mode of Towers of a Cable-Stayed Bridge Full-Model: Tests and Simulations, *Engineering Failure Analysis*, **122**, 105224.
- [27] Shah S.G., Desai. J.A., Solanki. C.H., 2010. Effect of Pylon Shape on Seismic Response of Cable Stayed Bridge with Soil Structure Interaction. *International Journal of Civil and Structural Engineering*, **1**(3), pp. 667-682.
- [28] Shah N.D., Desai J.A., Patil H.S., 2011. Effect of Pylon Shape on Analysis of Cable-Stayed Bridges. *Journal of Engineering Research and Studies*, **2**(1), pp. 104-109.
- [29] Sharath R., Ingle R.K., 2019. Pylon Shape Analysis of Cable-Stayed Bridges. In: Rao A., Ramanjaneyulu K. (eds) *Recent Advances in Structural Engineering*, Volume 1. *Lecture Notes in Civil Engineering*, **11**. Springer, Singapore.
- [30] Polepally G., Pasupuleti V.D.K., Dongre A., 2020. Comparison of Different Types of Pylon Shapes on Seismic Behaviour of Cable-Stayed Bridges. In: Babu K., Rao H., Amarnath Y. (eds) *Emerging Trends in Civil Engineering*. *Lecture Notes in Civil Engineering*, 61. Springer, Singapore.
- [31] Okyar M., Pinar A., Tezcan D., Kamaci, Z., 2008. Late Quaternary Seismic Stratigraphy and Active Faults of the Gulf of Izmit (NE Marmara Sea). *Marine Geophysical Research*, **29**, pp. 89-107.

- [32] CSI, SAP2000 Integrated Software for Structural Analysis and Design, Computers and Structures Inc., Berkeley, California.



## Fabrication and Characterization of Persea Gratissima Oil Loaded Chitosan Nanoparticles and Investigation of Its Neuroprotective Effects

Serap YEŞİLKIR BAYDAR<sup>1,2,\*</sup> , Rabia ÇAKIR KOÇ<sup>3</sup> , Yasemin BUDAMA KILINÇ<sup>4</sup> ,  
Burak ÖZDEMİR<sup>5</sup> , Zeynep KARAVELİOĞLU<sup>6</sup> 

<sup>1</sup> Department of Biomedical Engineering, Istanbul Gelisim University, Istanbul, 34310, Turkey, **ORCID:** 0000-0001-6311-4302

<sup>2</sup> Life Sciences and Biomedical Engineering Research and Application Centre, Istanbul Gelisim University, Istanbul, 34310, Turkey

<sup>3</sup> Department of Bioengineering, Yildiz Technical University, Istanbul, 34230, Turkey, **ORCID:** 0000-0002-8545-9878

<sup>4</sup> Department of Bioengineering, Yildiz Technical University, Istanbul, 34230, Turkey, **ORCID:** 0000-0003-0601-3091

<sup>5</sup> Department of Bioengineering, Yildiz Technical University, Istanbul, 34230, Turkey, **ORCID:** 0000-0003-0157-5052

<sup>6</sup> Department of Bioengineering, Yildiz Technical University, Istanbul, 34230, Turkey, **ORCID:** 0000-0002-8665-2178

### Article Info

#### Research paper

Received : December 27, 2020

Accepted : June 29, 2021

#### Keywords

Chitosan  
Encapsulation  
Persea gratissima  
Nanoparticles  
Neuroprotection

### Abstract

*Persea gratissima* known as avocado is a valuable plant. *P. gratissima* (PgO) oil is used in traditional medicine to treat several health problems because of its numerous biological properties. *P. gratissima* is a source of phytosterols and has effects as antimicrobial, anti-inflammatory, anti-oxidant and neuroprotective activities for *in vitro* and *in vivo* models. The aim of this study is to synthesize and characterize the PgO loaded chitosan nanoparticles and investigate the neuroprotective effects *in vitro*. According to neuroprotective effects, we prepared nanocapsulation of *P. gratissima* with chitosan using by ionic gelation method. Mitochondrial activity of *P. gratissima*, chitosan nanoparticles and PgO loaded chitosan nanoparticles were investigated by XTT method on SH-SY5Y and L929 cell lines comparatively. Obtained results showed that PgO loaded chitosan nanoparticles have a proliferative effect for SH-SY5Y cell line as a neuroprotective agent and no side effect for both SH-SY5Y and L929 cell lines. In conclusion PgO loaded chitosan nanoparticles are promising for neural regeneration and candidate for further *in vitro* and *in vivo* evaluation as a potential neurodegenerative disease drug formula.

## 1. Introduction

*Persea* sp. are in *Lauraceae* family which are evergreen trees, distributed in tropical and subtropical regions around the world. *P. gratissima* is a valuable kind of genus, and its fruit known as avocado has numerous biological activities such as antimicrobial [1-4] and anti-oxidant properties [5, 6]. The biological activities of *P. gratissima* are due to the existence of various classes of natural products mentioned in Table 1 [7]. It has a high potential for phytochemicals such as phytosterols and their analogues [8]. *P. gratissima* and its derivatives have been used by many communities for local medicine to treat several health problems [9] and many investigations

highlight the effectiveness of this fruit as an antifungal [1], antibacterial [2, 3], antiviral [4], analgesic, anti-inflammatory, anti-haemolytic, hepatoprotective [10], and especially anti-oxidant activities [11]. Anti-oxidant properties of plants are due to their high potential for phytochemicals such as phytosterols and their analogues [8]. It is known for several decades that chemicals obtained from plants, such as vegetables, herbs and fruits, are known to treat potential in several traditional local medicines [12, 13]. Another potential to treat is PgO and it is declared as a source of phytosterols (analogues of cholesterol and  $\beta$ -sitosterole) [14] and these compounds have been associated with different pharmacological activities such as anti-inflammatory, antioxidant, and anti-apoptotic [10, 15]. The  $\beta$ -sitosterole in *P. gratissima* has a special effect on neuroprotection, contributing to the treatment of neurodegenerative diseases such as Alzheimer disease. In relation to neuroprotection, it works as a

\* Corresponding Author: syesilkir@gelisim.edu.tr



chemoprotection agent [13, 15-17]. Also, the promise of this compound for the treatment of various diseases defines it as one of the notable components of the future, making it the major drug of the future [15].

**Table 1.** Bioactive compounds present in PgO [5].

Class of Natural Product	Name of the Composition
Temperature	Linoleic acid
	Oleic acid
	Palmitic acid
	Palmitoleic acid
Phytosterols	Compesterol
	$\beta$ -sitosterol
	Stigmasterol
	$\Delta^5$ -avenasterol
	$\Delta^7$ -avenasterol
Tocopherols	$\alpha$ -tocopherol
	$\gamma$ -tocopherol
	Vitamin E

While determining the effects of active substances on diseases, on the other hand, scientists has started to be applied an advantageous method for herbal pharmaceuticals called micro/nanocapsulation. This method is a process of enclosing a substance as the core material inside a membrane to protect against environmental factors. Encapsulation is a widely used technique in many fields such as textile and food industries, medical areas for cell immobilisation, cell transplantation, fermentation, drug delivery and many other fields [18]. The structure of the nanoparticles is composed of the core and the wall. The core is the active part and the covering material of capsules is also known as membrane, carrier or shell [19]. There are several synthetic and natural polymers and also organic materials used as wall in micro/nanoparticles. The selection of wall material is very important and related to the physical properties of the core material, correspondingly a hydrophilic polymer wall is necessary for a lipophilic core and an aqueous core needs an insoluble polymer wall [18]. A wide range of polymers and various polymer combinations are suitable for the encapsulation of nanostructures. Chitosan is commonly used as a wall material polymer because it does not show toxicity. Further advantages of chitosan are its biocompatibility, due to its physical and chemical properties, biodegradability, and stability in micro- and nano-sized particles, and under high-temperature conditions. For these reasons, Cht-NPs have great importance in controlled drug delivery systems [20]. In the literature, there are several encapsulation methods for several herbal oils (electrospraying for Peppermint oil

[21], phase separation for Rosemary oil [22], emulsify-solvent diffusion for Lavender oil and spray-drying for Chia essential oil [23] are documented. Nevertheless, there is restricted knowledge about PgO encapsulation. On the other hand, there is also less study about PgO-Cht-NPs' *in vitro* investigation that comes into prominence with its antioxidant, anti-apoptotic [13], and improvement of mitochondrial function [24] properties, especially for neuroprotection.

Therefore, the aim of this study is the preparation and characterization of nanoformulations of PgO, and the investigation of neuroprotective effects of these nanoparticles.

In this study, PgO-Cht-NPs were applied and cell proliferation effects of PgO, blank Cht-NPs and PgO-Cht-NPs, were searched on SH-SY5Y neural cell line for neuroprotective observation and L929 fibroblast cell line for control, individually and comparatively, for the first time in this study.

## 2. Materials and Methods

### 2.1. Preparation of Chemicals

Chitosan (Low Molecular Weight; 50.000-190.000 kDa) and polyvinyl alcohol (PVA) (Mw = 31.000-50.000, 87-89%) were purchased from Sigma-Aldrich USA (2.5% w: v CAS# 9012-76-4). 2,3-bis-(2-methoxy-4-nitro-5-sulfophenyl)-2H-tetrazolium-5-carboxanilide (XTT) was obtained from Merck (Darmstadt, Germany). All the chemicals and solvents were of analytical grade and inspired by the study of Cakir-Koc et. al (2018) [25]. *P. gratissima* oil (*Persea gratissima* - CAS# 8024-32-6, Talya herbal, Antalya, Turkey) was purchased from a pharmacy in Istanbul. Product certificate of analysis is obtained from the company. Ultrapure water from Millipore Milli-Q Gradient System was used to prepare the solutions.

#### 2.1.1. Synthesis of Cht-NPs

Cht-NPs were prepared using a modified version of the ionic gelation method [26]. Chitosan was added to 1% (v: v) acetic acid solution and mixed on a magnetic stirrer until a homogeneous solution was obtained. The pH of the solution was adjusted to 4.6–4.8. Next, Tween 80 (CAS# 9005-65-6, Sigma-Aldrich) mixture (1:1, v: v) was combined with a solution of chitosan. In order to obtain a homogeneous solution, the mixture was stirred at room temperature for 2 h. Next, sodium tripolyphosphate (TPP, CAS# 7758-29-4, Sigma-Aldrich) was dissolved in distilled water (0.05%, w: v) and then added drop-wise.



The solution was agitated on a magnetic stirrer for 45 min, and finally, ultra-sonication was applied. The samples were filtered with a 22µm pore-sized regenerated cellulose membrane before characterization.

### 2.1.2. Synthesis of PgO-Cht-NPs

PgO-Cht-NPs were prepared as mentioned above. And next, PgO and Tween 80 mixture (1:1 v: v) were combined with a solution of chitosan. In order to obtain a homogeneous solution, the mixture was stirred at room temperature for 2 h. Next, TPP was dissolved in distilled water (0.05%, w: v) and then added drop-wise. The solution was agitated on a magnetic stirrer for 45 min, and finally, ultra-sonication was applied. The samples were filtered with a 22 µm pore-sized regenerated cellulose membrane before characterization each sample was filtered through a 0.2 µm regenerated cellulose membrane (Sartorius, Germany) to remove any impurities from the solutions.

## 2.2. Characterization of Nanoparticles

### 2.2.1. Dynamic Light Scattering Analysis

In order to analyze of average particle size, polydispersity index, and zeta potential of PgO-Cht-NPs, a Zeta-sizer Nano ZS (Malvern Instruments, UK) instrument equipped with a 4.0 mV He-Ne laser (633 nm) was used. Every electrophoretic light scattering measurement was performed at 25°C and each sample was prepared with phosphate-buffered saline (PBS) before filtering with 0.45 µm Polyethersulfone (PES) membrane.

### 2.2.2. Preparation of Standard Curve of PgO

The standard curve of PgO was prepared using a UV-Vis spectrometer (Shimadzu, Japan) at 230 nm. The encapsulation and loading efficiency of PgO-Cht-NPs were determined by using the standard curve.

### 2.2.3. Encapsulation Efficiency and Loading Capacity of the PgO-Cht-NPs

To determine the efficiency of the encapsulation, the free PgO concentration in the supernatant taken after centrifugation was determined by using the calibration curve. After the amount of free PgO was found, the encapsulation efficiency was calculated using the following formula Eq. (1).

$$\text{Encapsulation Efficiency (\%)} = \frac{(\text{Total drug amount} - \text{Free drug amount})}{\text{Total drug amount}} \times 100 \quad (1)$$

Loading capacity was calculated by following the formula Eq. (2).

$$\text{Loading Capacity} = \frac{\text{Encapsulated PgO}}{\text{Total Cht-NPs weight}} \quad (2)$$

### 2.2.4. In Vitro Release Test

1 mL of nanoparticles were placed in dialysis capsules. Once these dialysis capsules were disposed into beakers containing PBS (pH: 7.4), the beakers were placed in a 37°C water bath under gentle agitation. A time-dependent release study was carried out at time intervals of 0; 0.5; 1; 2; 3; 6; 7; 9; 10; 24; 72; 96; 120; 144; 168; 192 and 216 h. At proper time intervals, the intake amounts of PgO-Cht-NPs were first extracted in PBS and then quantified spectrophotometric at 230 nm. These amounts of released PgO values were obtained from the calibration curve. The release of PgO was determined as per the following equation (3).

$$\text{Release (\%)} = \frac{\text{Released PgO}}{\text{Total PgO}} \times 100 \quad (3)$$

## 2.3. Cell Culture Experiments

### 2.3.1. SH-SY5Y and L929 Cell Lines' Culture

SH-SY5Y is a twice-subcloned cell line derived from the SK-N-SH neuroblastoma cell line. L929 is a mouse-derived dermal fibroblast cell line. Both of these cell lines were individually thawed and transferred into a 10% foetal bovine serum (FBS) containing DMEM/F-12 (supplemented with 0,05% penicillin-streptomycin) maintaining media. Cells were cultured in a humidified atmosphere at 37°C and 5% CO<sub>2</sub>.

### 2.3.2. Cytotoxicity Experiments

Both cell lines that are commercially available from ATCC, was used for the cytotoxicity studies. Fibroblast cultures are commonly used to understand the dermal response against new products. Cells were cultured as mentioned above. The plates were incubated at 37 °C for 3 days in a 5% CO<sub>2</sub> incubator until 80% confluence was attained. A trypsinization process was applied to the cells, and the detached cells were obtained by centrifugation. Then, both cell lines were seeded (10,000 cells/well) in 96-well flat-bottom microplates with 100 µL of the medium. The plates were incubated at 37 °C for 24 h, for attachment

to the good bottoms. Various concentrations (1, 5, 10, 20, 50 and 100 µg/mL) of the Cht-NPs and PgO-Cht-NPs were added, respectively, and incubated for another 24 h. The media containing chitosan or nanoparticles were then removed, and 100 µL of XTT (2,3-bis-(2-methoxy-4-nitro-5-sulfophenyl)-2H-tetrazolium-5-carboxanilide, Merck, Darmstadt, Germany) solution in the fresh medium was added to the wells at 0,5 mg/mL (with 7,5 µg/mL phenazine methosulfate). The cells were incubated at 37 °C for 3 h. Afterward, the optical density was measured at 450 nm with a multi-plate reader (Thermo Labsystems Multiscan Ascent 354 Microplate Photometer). Finally, the percentage of the cell viability was calculated by the following equation.

$$\text{Viability (\%)} = \frac{\text{Absorbance of experimental group}}{\text{Absorbance of control group}} \times 100 \quad (4)$$

## 2.4. Statistical Analysis

Experiments were triplicated. GraphPad Prism 5 program was used. Homogeneity of variants was determined by ANOVA one-way. Values  $p < 0.005$  were meaningful statistically.

## 3. Results and Discussion

In this study, PgO-Cht-NPs were prepared, and the proliferative effects of PgO-Cht-NPs on SH-SY5Y and L929 were comparatively determined. SH-SY5Y is a neuronal cell line. L929 is a fibroblast cell line that is used to represent a comparison cell for the purpose of the study.

For the chemical steps of the study, an ionic gelation technique was used to prepare the nanoparticles. Briefly, this method is based on an ionic gelation interaction, formed by the repulsive force between positively-charged chitosan and negatively-charged TPP. This procedure was undertaken to synthesize empty Cht-NPs and PgO-Cht-NPs. These two types of nanoparticles were examined and compared for their physicochemical properties, as well as their biological properties in cell culture.

### 3.1. Nanoparticle Characterization Results

#### 3.1.1. Dynamic Light Scattering Analysis

The average size of the blank and PgO-Cht-NPs was determined using the DLS technique, with triplicate measurements (Table 2). Blank Cht-NPs has a size of 51,63 nm, a zeta potential of 10,9 mV, and a PDI of 0,156, whereas PgO-Cht-NPs are 53,22 nm, with a zeta potential of 8,88 mV and a PDI of 0,211. This means that

nanoparticles have a similar size and their diameters are formally called nanoparticles (Data not shown).

Zeta potentials of the nanoparticles are between +30 nm and -30 nm. Zeta potentials that are higher than +30 mV and lower than -30 mV mean instability for the chemical characteristics of the nanoparticles. As a result, this means that we obtained chemically stable nanoparticles.

**Table 2.** Zeta-average diameter results of nanoparticles.

Nanoparticles	Size (nm)	PDI	Zeta potential (mV)
Cht-NPs	51,63	0,156	10,9
PgO-Cht-NPs	53,22	0,211	8,88

#### 3.1.2. Determination of Encapsulation Efficiency, Loading Efficiency and Release Profile

The standard curve obtained using various concentrations of PgO (Figure 1) was used to determine the encapsulation efficiency, loading capacity and release profile of the PgO-Cht-NPs. Equation 1 was used for encapsulation efficiency and it was found that encapsulation efficiency was 86%. When the literature is examined, it is seen that these rates have lower percentages ((36.2% and 17.2%, respectively) than the results we obtained [27, 28].

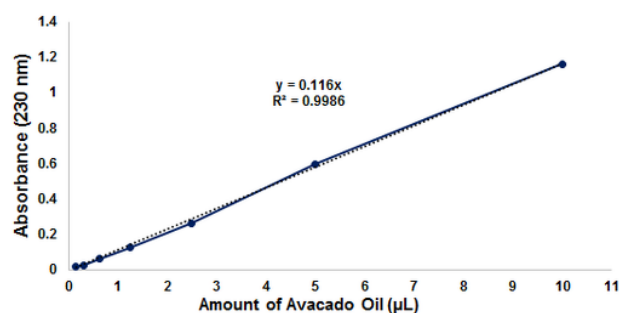


**Figure 1.** Calibration curve of PgO.

This ratio of encapsulation efficiency (86%) shows that encapsulation is successful. Equation 2 was used to calculate the loading efficiency of PgO-Cht-NPs. The data show that 0,625 µl of PgO is present in each 1 mg nanoparticle. It means the loading capacity was 62.5%, whereas in other studies these rates were much lower (19.2% and 3.38%, respectively) [27, 28]. When we look at the release profile, it is seen that PgO is released in a controlled and slow way from Cht-NPs. The *in vitro* release profile of PgO-Cht-NPs is given in Figure 2. *In*

*vitro* release profile determination was performed using PBS (pH: 7,4) solution. The first ten hours' releasing value was determined as 3,16  $\mu\text{L}$ , and this rate was determined as 9,925  $\mu\text{L}$  after 216 hours.

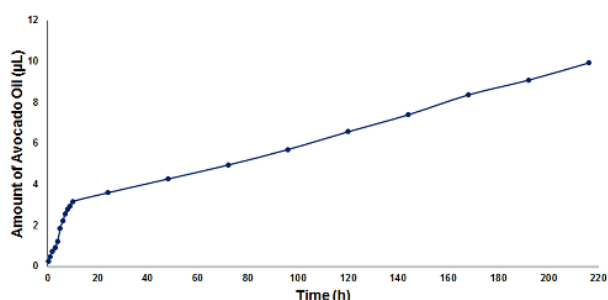


**Figure 2.** In vitro release profile of PgO-Cht-NPs.

### 3.1.3. Cell Culture Results

After the characterization experiments of PgO, PgO-Cht-NPs, and CNs, we applied six different concentrations (1, 5, 10, 20, 50, and 100  $\mu\text{g}/\text{mL}$ ) in cell culture experiments. For this purpose, thawed cells were adapted into the cell culture conditions. Both cells lines were grown in 37 °C and 5% humidified incubator for 4-7 days (Figure 3). After they reached 80% confluence cells were used for the toxicity experiments.

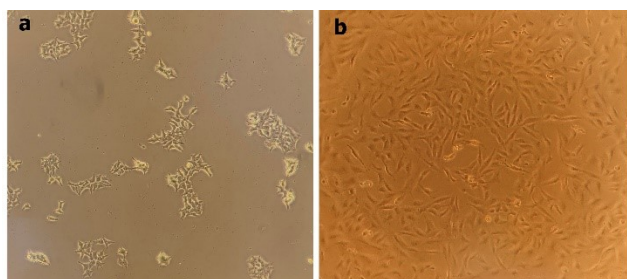


**Figure 3.** Observation of SH-SY5Y (a) and L929 (b) cell lines culture at inverted microscope (20X).

According to the results non-capsulated PgO concentrations, showed a significant toxic effect on the SH-S5Y5 cell lines. Although cell viability started to decrease from the lowest concentrations to higher for SH-S5Y5, while L929 cell line survived at a stable level. The blank CNs presented no significant decrease in cell viability for both SH-S5Y5 and L929 cell lines at the investigated concentrations. Whatever, it is known that chitosan is a biocompatible polymer and does not provoke a toxic effect on cells [37]. And our cell culture results also support this literature data. Finally, PgO-Cht-NPs showed a significant induction for SH-S5Y5 cell line approximately 77% (min 54%, max 90%) while its lower concentrations (1 and 5  $\mu\text{g}/\text{mL}$ ) induced L929 cell line proliferation up to 27%, and higher concentrations (10, 20,

and 50  $\mu\text{g}/\text{mL}$ ) do not affect but 100  $\mu\text{g}/\text{mL}$  showed a decrease in cell proliferation (24%). PgO is used in many different cosmetic products such as well skin and hair care products. Vitamins A, D, E, lecithin, Omega 9 fatty and phytosterols acids promote healing, skin regeneration, collagen augmentation and protection from the aging effects of UV light and pollution [29]. In addition, cytotoxicity [10, 30], nitric oxide and superoxide generation inhibition [10, 31], anti-cardiovascular disease [32], acetyl-CoA carboxylase inhibition [33], skin lysyl oxidase inhibition [34], and liver injury suppressing [35] effects have also been demonstrated, and suggest *P. gratissima* fruits are a healthy natural product to consume [6].

### 3.1.4. Cytotoxicity Results

Effects of different concentrations of PgO, blank Cht-NPs and PgO-Cht-NPs were performed using with XTT assay. Initial results showed that PgO has an inhibitory effect on SH-SY5Y for all concentrations. On the other hand, PgO did not decrease the cell proliferation rate for L929 (Figure 4).

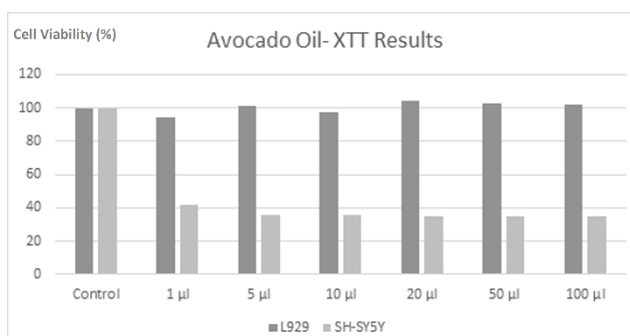


**Figure 4.** XTT results for PgO on L929 and SH-SY5Y cell lines.

Cht-NPs effect on both cell lines was measured. As known in literature [20], Cht-NPs showed no inhibitory or activator effects on cell lines (Figure 5).

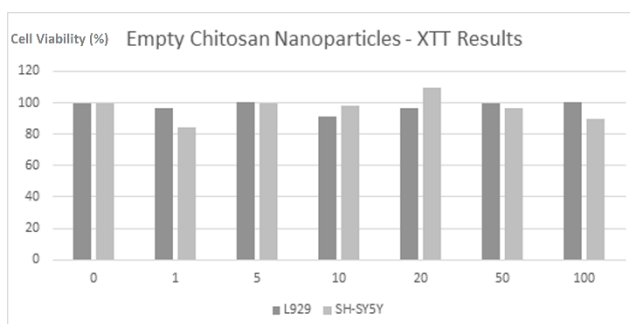


**Figure 5.** XTT results for Cht-NPs on L929 and SH-SY5Y cell lines.

While PgO decreased cell proliferation and blank Cht-NPs did not affect cell proliferation of SH-SY5Y, PgO-Cht-NPs showed a higher inductive effect (appr. 90%). Compared to L929, as seen in Figure 6, all concentrations of PgO-Cht-NPs were seen to have an increased cell viability. Although there is a decrease in cell viability at increasing concentrations (1, 5, 10, 20, 50, and 100%), it has been observed that the resistance of SH-SY5Y cells to this is significantly high between 54 – 90%.

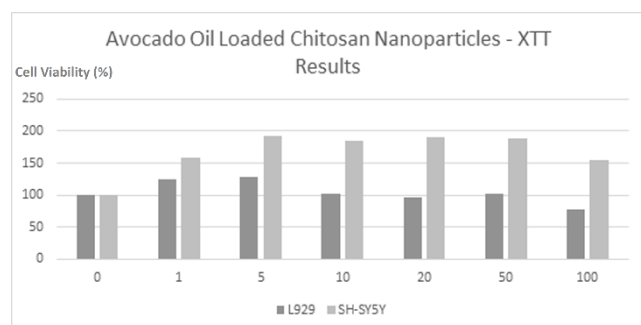


**Figure 6.** XTT results for PgO-Cht-NPs on L929 and SH-SY5Y cell lines.

When we search PgO's efficiency on various kinds of cell lines related to diseases, the neurodegenerative effect of  $\beta$ -sitosterol came across as an alternative model for neuronal diseases probably with its rich amount of phytosterols and its analogs especially  $\beta$ -sitosterol. As a hypothesis mitochondrial dysfunction has been declared to be a key factor in the progression of hyperglycaemia-mediated neuronal damage [24] and a study reported that  $\beta$ -SITO is a tubulin-binding unit and its interaction with tubulin involves several interesting features [13]. Additionally, the maintenance of oxidative phosphorylation capacity is extremely important in the central nerve system (CNS) since about 90% of the energy required for the healthy function of neurons is provided by mitochondria. Thus, mitochondrial dysfunction may cause loss of neuronal metabolic control and, consequently, neurodegeneration. This approach is supported by data demonstrating mitochondrial function decline with aging and in age-related diseases [24]. Thus, we cultured SH-SY5Y cell line and investigated the mitochondrial function degree (related to cell proliferation rate) by XTT method for PgO, CNs, and PgO-Cht-NPs compared to the L929 cell line.

As we mentioned above, this study is an initial investigation to observe the neuroprotective effects of PgO-Cht-NPs. Our results showed similar results for Cht-NPs on cell proliferation declared in literature [20, 36, 37] and a new perspective (approach, modality) was offered to use as a protective formula for neurodegenerative diseases.

## 4. Conclusions

A major challenge associated with several diseases such as cancerogenic and neurodegenerative diseases is the side effects or insufficient drug efficacy [38]. Despite the many benefits of essential herbal oils, they cause some biochemical and physicochemical negations such as high volatility and uncontrollable dosage. Profusion is also a disadvantage that is thought to be easily solved through the encapsulation method. Regarding the advantages of encapsulation techniques, it is expected that the practice of micro/nanoparticles containing essential herbal oils will widely increase in the next years [18]. Our results showed that PgO-Cht-NPs have a proliferative effect for cell proliferation for SH-SY5Y cell line as a neuroprotective agent and no side effect for the fibroblast cell line. In this study, a new perspective was offered to use as a protective formula for neurodegenerative diseases. Given the health benefits of PgO that has important phytosterols such as  $\beta$ -sitosterol, including neuroprotection [17], are proposed as a suitable candidate for further *in vitro* and *in vivo* evaluation as a potential neurodegenerative disease drug formula.

## Declaration of Ethical Standards

The authors of this article declare that the materials and methods used in this study do not require ethical committee permission and/or legal-special permission.

## Conflict of Interest

The authors declare that they have no known competing financial interests or personal relationships that could have appeared to influence the work reported in this paper.

## Acknowledgements

The authors express thanks to Talya Herbal Products INC. (Kepez-Anlatya / Turkey) for the PgO product certificate information. In this study, the infrastructure of Applied Nanotechnology and Antibody Production Laboratory established with TUBITAK support (project numbers: 115S132 and 117S097) was used. The authors would thank TUBITAK for their support. This study has been also funded by Istanbul Gelişim University Scientific Research Projects Application and Research Centre with the project number: KAP-270320-SYB.

## References

- [1] Abubakar A.N.F., Achmadi S.S., Suparto I.H., 2017. Triterpenoid of Avocado (*Persea americana*) Seed and Its Cytotoxic Activity Toward Breast MCF-7 and Liver Hepg2 Cancer Cells. *Asian Pacific Journal of Tropical Biomedicine*, **7**(5), pp. 397-400.
- [2] Lu Y.C., Chang H.S., Peng C.F., Lin C.H., Chen I.S., 2012. Secondary Metabolites from The Unripe Pulp of *Persea americana* and Their Antimycobacterial Activities. *Food Chem*, **135**(4), pp. 2904-2909.
- [3] Jorge T.d.S., Polachini T.C., Dias L.S., Jorge N., Telis-Romero J., 2015. Physicochemical and Rheological Characterization of Avocado Oils. *Ciência e Agrotecnologia*, **39**, pp. 390-400.
- [4] Harborne J.B., Williams C.A., 2000. Advances in Flavonoid Research since 1992. *Phytochemistry*, **55**(6), pp. 481-504.
- [5] Álvarez J.M., Juan M., Luis E.C., Alegre A.C.P., Ana B.R.M., Ignacio F., Alberto F.G., 2016. Phenolic Constituents of Leaves from *Persea caerulea* Ruiz & Pav; Mez (Lauraceae). *Biochemical Systematics and Ecology*, **67**, pp. 53-57.
- [6] Leite J.J., Brito E.H., Cordeiro R.A., Brillhante R.S., Sidrim J.J., Bertini L.M., Morais S.M., Rocha M.F., 2009. Chemical Composition, Toxicity and Larvicidal and Antifungal Activities of *Persea americana* (Avocado) Seed Extracts. *Rev Soc Bras Med Trop*, **42**(2), pp. 110-113.
- [7] Kruthiventi A.K., Krishnaswamy N.R., 2000. Constituents of the Flowers of *Persea gratissima*. *Fitoterapia*, **71**(1), pp. 94-96.
- [8] Schlemper S.R., Schlemper V., da Silva D., Cordeiro F., Cruz A.B., Oliveira A.E., Cechinel-Filho V., 2001. Antibacterial Activity of *Persea cordata* Stem Barks. *Fitoterapia*, **2**(1), pp. 73-75.
- [9] Miranda M.M., Almeida A.P., Costa S.S., Santos M.G., Lagrota M.H., Wigg M.D., 1997. In Vitro Activity of Extracts of *Persea americana* Leaves on Acyclovir-Resistant and Phosphonoacetic Resistant Herpes Simplex Virus. *Phytomedicine*, **4**(4), pp. 347-352.
- [10] Nicoletta H.D., Neto F.R., Corrêa M.B., Lopes D.H., Rondon E.N., Dos Santos L.F.R., de Oliveira P.F., Damasceno J.L., Acésio N.O., Turatti I.C.C., Tozatti M.G., Cunha W.R., Furtado R.A., Tavares D.C., 2017. Toxicogenetic Study of *Persea americana* Fruit Pulp Oil and Its Effect on Genomic Instability. *Food and Chemical Toxicology*, **101**, pp. 114 - 120.
- [11] Terasawa, N., Sakakibara, M., Murata, M., 2006. Antioxidative Activity of Avocado Epicarp Hot Water Extract. *Food Science and Technology Research*, **12**, pp. 55-58.
- [12] Chun H.S., Kim J.M., Choi E.H., Chang N., 2008. Neuroprotective Effects of Several Korean Medicinal Plants Traditionally Used for Stroke Remedy. *J Med Food*, **11**(2), pp. 246-251.
- [13] Mahaddalkar T., Suri C., Naik P.K., Lopus M., 2015. Biochemical Characterization and Molecular Dynamic Simulation of Beta-Sitosterol as A Tubulin-Binding Anticancer Agent. *Eur J Pharmacol*, **760**, pp. 154-62.
- [14] Duester K.C., 2001. Avocado Fruit is a Rich Source of Beta-Sitosterol. *Journal of the American Dietetic Association*, **101**(4), pp. 404-405.
- [15] Soodabeh Saeidnia A.M., Gohari A.R., Abdollahi M., 2014. The Story of Beta-sitosterol- A Review. *European Journal of Medicinal Plants*, **4**(5), pp. 590-609.
- [16] Bouic P.J.D., Etsebeth S., Liebenberg R.W., Albrecht C.F., Pegel K., Van Jaarsveld P.P., 1996. Beta-Sitosterol and Beta-Sitosterol Glucoside Stimulate Human Peripheral Blood Lymphocyte Proliferation: Implications for Their Use as An Immunomodulatory Vitamin Combination. *International Journal of Immunopharmacology*, **18**(12), pp. 693-700.
- [17] Hamedi A., Ghanbari A., Razavipour R., Saeidi V., Zarshenas M.M., Sohrabpour M., Azari H., 2015. *Alyssum homolocarpum* Seeds: Phytochemical Analysis and Effects of The Seed Oil on Neural Stem Cell Proliferation and Differentiation. *Journal of Natural Medicines*, **69**(3), pp. 387-396.
- [18] Ghayempour S., Montazer M., 2016. Micro/Nanoencapsulation of Essential Oils and Fragrances: Focus on Perfumed, Antimicrobial, Mosquito-Repellent and Medical Textiles. *Journal of Microencapsulation*, **33**(6), pp. 497-510.
- [19] Nelson G., 2013. 4-Microencapsulated Colourants for Technical Textile Application, in *Advances in the Dyeing and Finishing of Technical Textiles*, 1st ed., Woodhead Publishing, Sawston, Cambridge.
- [20] Budama-Kilinc Y., Cakir-Koc R., Kaya Z., 2017. Chemistry Preparation and Cytotoxicity of *Coriandrum sativum* L. Oil Loaded Chitosan Nanoparticles *Journal of the Turkish Chemical Society*, **5**(1), pp. 179-92.
- [21] Ghayempour S., Mortazavi S.M., 2013. Fabrication of Micro-Nanocapsules by A New Electrospinning Method Using Coaxial Jets and Examination of

- Effective Parameters On Their Production. Journal of Electrostatics, **71**(4), pp. 717-727.
- [22] Badulescu R., Vera V., Darja J., Bojana V., 2008. Grafting of Ethylcellulose Microcapsules onto Cotton Fibers. Carbohydrate Polymers, **71**(1), pp. 85-91.
- [23] Rodea-Gonzalez D.A, Cruz-Olivares J., Román-Guerrero A., Rodríguez-Huezo M.E., 2012. Spraydried Encapsulation of Chia Essential Oil (*Salvia hispanica* L.) In Whey Protein Concentrate-Polysaccharide Matrices. Journal of Food Engineering, **111**, pp. 102-109.
- [24] Ortiz-Avila O., Esquivel-Martínez M., Olmos-Orizaba B.E., Saavedra-Molina A., Rodríguez-Orozco A.R., Cortés-Rojo C., 2015. Avocado Oil Improves Mitochondrial Function and Decreases Oxidative Stress in Brain of Diabetic Rats. J Diabetes Res, pp. 485-489.
- [25] Çakir Koç R., Budama-Kilinc Y., Kaya Z., Berber Orcen B., Ucarıkus E., 2018. Coconut Oil-Loaded Chitosan Nanoparticles for The Treatment of Acne Vulgaris: Cytotoxicity, Antibacterial Activity, and Antibiofilm Properties. Fresenius Environmental Bulletin, **27**(3), pp. 1-7.
- [26] Calvo P., Remuon-Lopez C., Vila-Jato J. L., Alonso M. J., 1997. Novel Hydrophilic Chitosan-Polyethylene Oxide Nanoparticles as Protein Carriers. Journal of Applied Polymer Science, **63**(1), pp. 125-132.
- [27] Esmacili A., Asgari A., 2015. In Vitro Release and Biological Activities of Carum Copticum Essential Oil (CEO) Loaded Chitosan Nanoparticles. Int J Biol Macromol, **81**, pp. 283-290.
- [28] Mohammadi A., Hashemi M., Hosseini S.M., 2015. Chitosan Nanoparticles Loaded with Cinnamomum Zeylanicum Essential Oil Enhance the Shelf Life of Cucumber During Cold Storage. Postharvest Biology and Technology, **110**, pp. 203-213.
- [29] Salazar M.J., El Hafidi M., Pastelin G., Ramírez-Ortega M.C., Sánchez-Mendoza M.A., 2005. Effect of an Avocado Oil-Rich Diet Over an Angiotensin II-Induced Blood Pressure Response. Journal of Ethnopharmacology, **98**(3), pp. 335-338.
- [30] Oberlies N.H., Rogers L.L., Martin J.M., McLaughlin J.L., 1998. Cytotoxic and Insecticidal Constituents of the Unripe Fruit of *Persea Americana*. J Nat Prod, **61**(6), pp. 781-785.
- [31] Kim O.K., Murakami A., Nakamura Y., Takeda N., Yoshizumi H., Ohigashi H., 2000. Novel Nitric Oxide and Superoxide Generation Inhibitors, Persenone A and B, From Avocado Fruit. J Agric Food Chem, **48**(5), pp. 1557-1563.
- [32] Adeboye J.O., Fajonyomi M.O., Makinde J.M., Taiwo O.B., 1999. A Preliminary Study On the Hypotensive Activity of *Persea Americana* Leaf Extracts in Anaesthetized Normotensive Rats. Fitoterapia, **70**(1), pp. 15-20.
- [33] Hashimura H., Ueda C., Kawabata J., Kasai T., 2001. Acetyl-CoA Carboxylase Inhibitors from Avocado (*Persea americana* Mill.) Fruits. Bioscience, Biotechnology, and Biochemistry, **65**, pp. 1656-1658.
- [34] Werman M., Mokady, S., Neeman, I., 1990. Partial Isolation and Characterization of a New Natural Inhibitor of Lysyl Oxidase from Avocado Seed Oil. Journal of Agricultural and Food Chemistry, **38**, pp. 2164-2168.
- [35] Kawagishi H., Fukumoto Y., Hatakeyama M., He P., Arimoto H., Matsuzawa T., Arimoto Y., Suganuma H., Inakuma T., Sugiyama K., 2001. Liver Injury Suppressing Compounds from Avocado (*Persea americana*). Journal of Agricultural and Food Chemis, **49**, pp. 2215-2221.
- [36] Budama-Kilinc Y., Cakir-Koc R., Kecel-Gunduz S., Kokcu Y., Bicak B., Mutlu H., Ozel A.E., 2018. Novel NAC-Loaded Poly(Lactide-Co-Glycolide Acid) Nanoparticles for Cataract Treatment: Preparation, Characterization, Evaluation of Structure, Cytotoxicity, and Molecular Docking Studies. PeerJ, **6**, pp. e4270.
- [37] Kumar M., 2000. A review of Chitin and Chitosan Applications. Reactive & Functional Polymers, **46**(1), pp. 1-27.
- [38] Law B.Y.K., Wu A.G., Wang MJ., Zhu Y.Z., 2017. Chinese Medicine: A Hope for Neurodegenerative Diseases? J Alzheimers Dis, **60**(s1), pp. 151-160.



# Representing American Sign Language Letters and Numbers with Humanoid Robot Arm

Mehmet GÜL<sup>1,\*</sup> 

<sup>1</sup> Department of Computer Engineering, Şırnak University, Şırnak, 73000, Turkey, **ORCID:** 0000-0002-4819-4743

## Article Info

### Research paper

Received : February 17, 2021

Accepted : July 07, 2021

### Keywords

Humanoid Robotic Arm  
Sign Language  
Deep Learning  
Human-Robot Interaction  
Speech-Recognition

## Abstract

The widespread use of robotic systems is an example of increasing technological developments in daily life. The robotic systems that are accustomed to widespread use in the industry show huge impact in education, health, and many other areas nowadays. Robotic systems are no longer expensive and are not difficult to access systems that can be drawn and designed with design software like CAD programs. Within the scope of the study, major changes are made in the reference design, and Python software is used to send data to the Arduino control card that is used for control of the robotic system and to provide movement. The humanoid robotic arm developed in the study is printed with the 3D printer, sign languages that can be realized by one-handed letters among sign languages were investigated. All 26 alphabetical letters of English in American Sign Language can be demonstrated with the right hand alone. It has nearly the same principle that represents the demonstration of sign language expressions with a robotic hand, and the American Sign Language is the most widely known sign language. If experience is gained with this study, it can be used for the other sign language. In this study, audio and text messages sent over Python were performed on the humanoid robotic arm.

## 1. Introduction

Sign language is considered the language that helps deaf people communicate with the outside world by converting the letters, numbers, words, and sentences of a natural language into hand and head gestures. Hearing-impaired individuals use hand gestures and facial expressions instead of sound to express themselves. Sign language varies from country to country and from region to region. The Ministry of Family Labor and Social Services of the Republic of Turkey published a statistics bulletin in 2020. There is a statistical table in that bulletin and according to the disabled people table, there were about 1.5 million hearing and speech impaired people in 2011 (Table 1) [1].

Hearing and speech loss bring about significant communication problems for individuals in daily life. Most people with this condition use sign language to

communicate with normal individuals. On the other hand, this situation is not understood by many individuals and is limited to individuals with hearing or speech impairment. Hearing-impaired individuals deserve all the help they need to continue their daily lives like normal people. One way to tackle this situation is to use advanced technology to overcome some of the challenges it faces. For example, high-tech machines that perform sign language, which is a combination of hand and head movements and facial gestures, and act as mediators between them and normal people, such machines are an example of human-machine interaction.

Today, humanoid robots are used in education [2], therapy [3], and entertainment. These developments are provided by encouraging experiments on humanoid robots. Studies on the use of robots as friends in the education and treatment processes of children with disabilities and special needs can be given as an example [4]. Teaching sign language to hearing-impaired children with the help of a humanoid robot can be given as an example.

Learning sign language is the most basic communication tool for people with hearing and speech

\* Corresponding Author: [mgul@simak.edu.tr](mailto:mgul@simak.edu.tr)



impairments to communicate with each other or other normal individuals. It has also been observed that sign language contributes significantly to the cognitive and intellectual development of individuals with hearing and speech impairments [5]. The special bond that a child will create with the humanoid robot can be an ideal tool for the use of the developed robot for both educational and therapeutic purposes for the child with whom it is in communication. Accordingly, it has been proposed to use humanoid robots as a game-based learning method in

education. It has been found that the quality of education and the willingness to play and interact with a child's autonomy or disability can be increased [6]. In some studies, robotic systems have been used in education, and it has been noted that they can be more effective than computer-based teaching systems [7, 8]. Kinematic limitations of the NAO and Robovie 3 robotic systems used in these studies, which greatly limit the number of signals, have been determined.

**Table 1** Population of disabled individuals across the country according to TURKSTAT 2011 [1].

Disability group	Total Population Rate (%)	Male (%)	Female (%)	Total (Number of People)	Male (Number of People)	Female (Number of People)
Those who have difficulty seeing	1,4	1,3	1,5	1.039.000	478.000	561.000
Those who have difficulty in hearing	1,1	1,1	1,2	836.000	406.000	429.000
Those who have difficulty speaking	0,7	0,8	0,6	507.000	278.000	229.000
Those who have difficulty walking, climbing / descending stairs	3,3	2,4	4,1	2.313.000	861.000	1.452.000
Those who have difficulty carrying / holding things	4,1	3,2	5,1	2.923.000	1.136.000	1.787.000
Those who have difficulty in learning / doing four simple operations / remembering attention according to their peers	2,0	1,6	2,4	1.412.000	565.000	847.000

Today, only a few ingenious anthropomorphic hands have been developed for humanoid robots. Examples of these robots are 13 degrees of freedom (DoF) fifty and Honda's ASIMO Humanoid1. On the other hand, the open-source iCup humanoid platform with 11 DoF [9], the ARMAR III upper body mobile with 8 DoF [10], and NASA's 11 DoF Robo-naut-2 humanoid robots can be cited as examples [11].

The mechanical and software stages of the developed humanoid robot arm in this study are introduced. The letters used in American Sign Language were realized with the humanoid robot arm developed in the study. Compared to the letters made in Turkish Sign Language (TSL) and also British Sign Language, the letters used in American Sign Language (ASL) can only be performed with one hand such as French Sign Language or Irish Sign Language.

## 2. Materials and Methods

The use of humanoid robotic technology in education has been successful, and the results of given examples are extracted from the studies [12, 13]. Letters of some sign languages can be performed with just one hand such as ASL, in the study, the developed robot arm has performed the letters and 0–9 numbers of ASL. There are seven servomotors used to control the robotic arm, two servos for the thumb, and the other four servos for other fingers, and the last one for the wrist.

Sign language, the realization of signs, requires the analysis of structures, especially phonological ones. Phonology in sign language expresses how a sign is created and arranged. Examining the ASL points out that each sign in the ASL can be divided into five components: hand shape, hand shape movement, the position of the mark, palm direction, head direction, and facial expressions, etc. [14]. Research has shown that these components, which can be applied to TSL, together form the meaning of a sign.

### 2.1. Electronic Architecture

The humanoid robotic arm is designed taking into account other design guidelines, such as low development cost, as well as its ability to mimic ASL markings. Palms and fingers are used in the study referenced on the web page of Thingiverse open-source sharing [15]. Other elements of the referenced design are not used, but redesigned due to insufficient actuators. In the reference design, a total of five actuator slots are opened and used for the movement of the fingers. On the other hand, for the movement of the fingers on the palm, a total of six actuators must be used. The reason for this is the unique movement of the thumb. The metacarpal bone in the thumb gives the thumb a different movement feature than other fingers. For this reason, two actuators need to be used to control the thumb (Figure 1).



**Table 2** The used electronic components

Servo Motor	Mini Servo Motor	Servo Control Card
MG996R	SG90	Mini Maestro Pololu 24 Channel Servo Control Board

The design referenced is shown in Figure 1.a. and Figure 1.b is the developed design. The components of the humanoid robot arm are developed using SolidWorks design software and printed on the 3D printer. PLA filament is used for printing the parts. 25 parts of a humanoid robot arm are printed by a 3D printer. In the study, a central computer and a control card providing movement are used to realize the letters and 0–9 numbers in ASL. An Arduino Uno is used to provide the movement. A MG996R servomotor is used for the movement of the fingers and an SG90 mini servomotor for the movement of the thumb from the palm. A Mini Maestro 24 channel servo motor control card is used to ensure the movement of servomotors. The movement is achieved by transferring the messages sent to the Arduino board via Python software to the servo motor control card. The software developed for providing movement is described in the next section.



a) Arm design consisting of 4 servo motors used for the movement of the fingers in the original design



b) redesigned robot arm shape

**Figure 1.** Robot arm printed with the 3D printer.

## 2.2. The Used Actuators and Other Mechanical Parts

It is necessary to use a servo horn to provide finger movements in the developed humanoid robot arm. The servo horn designs used in Thingiverse and other similar open-source web pages are examined, and it is decided to redesign the servo horn based on the experience gained from the applications. The servo horns used in many designs are shown in Figure 2. The humanoid robot developed by InMoov Company uses two different servo horns. In the first design show in Figure 2.a. the classical servo horns are used, and two fishing lines are used for the movement of the finger attached to the servo horn. The first design using servos used for finger movement can stretch the maximum amount of "r" with the servo horn. Figure 2.b shows the next design printed on a 3D printer.

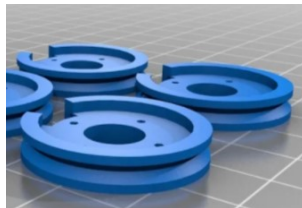
The biggest disadvantage of this design is that the line threads used for stretching and unloading are positioned and connected to the same horn. It has been observed that the line thread is wasted during the movement of the servo motor. It is observed that the InMoov design is used in the reference design. Due to the mentioned disadvantages, the servo horn has been redesigned and shown in Figure 3.

With the developed servo horn, the line thread is wound at least two cycles. In this case, it is noticed that the line thread that is stretched sufficiently fell into nothing. And on the contrary, the line thread is wound more effectively when winding.

Seven actuators are used in the robot arm. Considering easy maintenance and installation design factors, ready-made modular servomotors are judged to be the ideal solution for actuator selection. The robot arm has 16 degrees of freedom. Designs are prepared with the SolidWorks design software used for design and converted to STL format for printing on a 3D printer. In the next step, it is converted into Gcode with Simplfy3D slicing software and printed by a 3D printer. Finger movements are provided with a 90° movement.



a) Servo horn used for finger movement of the InMoov humanoid robot arm [15]



b) Another servo horn developed for InMoov humanoid robot arm [16]



c) Servo horn used in the referenced humanoid robot arm [17]

**Figure 2.** Servo horns used in the humanoid robot developed by InMoov company and referenced robot arm

### 2.3. Finger Design, Flexion/Extension Mechanism

For the palm and finger mechanism, the open-source design on the Thingiverse web page has been used [15]. In particular, the wired finger mechanism used in the iCub robot developed by S. Hirose [18] is taken as an example in the study. Rubber is used to help the finger actuator and replace it when it is idle. The tensile force created by the tire meets the force required by the servomotors used in the movement of the fingers to restore the finger. The finger structure is shown in Figure 4.

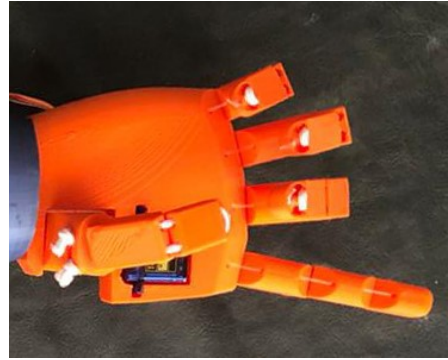
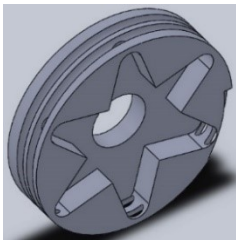


**Figure 4.** Fishing line and rubber used for the movement of the fingers



a. SolidWorks design



b. servo horn printed with the 3D printer

**Figure 3.** Developed servo horn

There is a DoF feature that allows the human wrist to move up and down. In the kinematic structure of the robot, the lateral movement of the wrist is not taken into account, and the tendon mechanism of the wrist movement and the cable routes are shown in Figure 4.

For finger movements, the angular positions of the servomotors are determined and positioned separately. One end of the line rope is knotted at the fingertip and the other end is knotted to Servo Horns attached to the servomotor. A rubber rope is used to restore the unilateral pulling procedure to its original position (see Figure 4). The tensile force accumulated in the rubber rope contributes to the transfer of the fingers to their initial positions.

### 3. Developed Software

Two software packages are used for the integrated software developed for the humanoid robot arm, Python and Arduino. Figure 5 shows the flow chart of the integrated software.

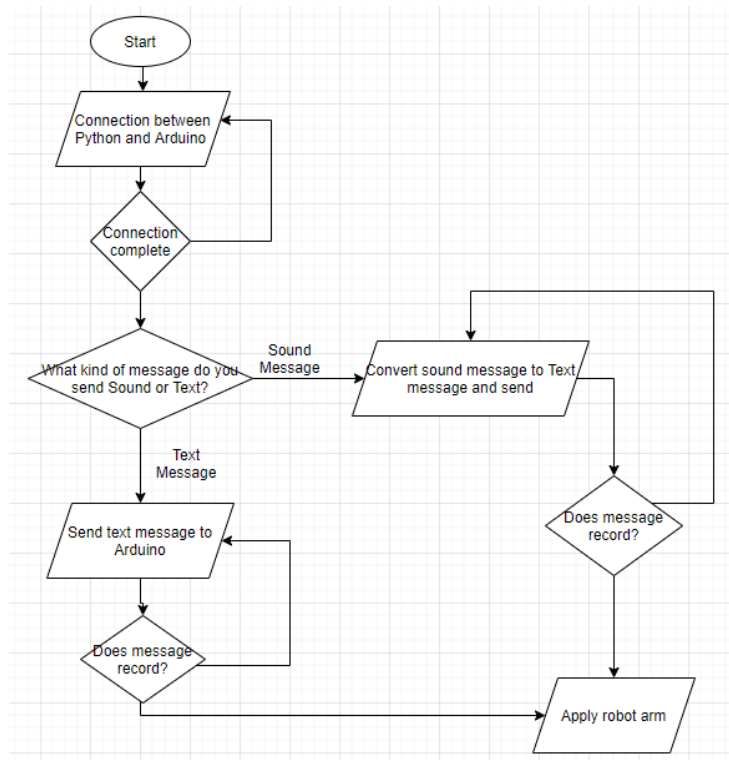


**Figure 5.** Flowchart of integrated software

The speech recognition (SR) system can be speaker-dependent or independent. The speaker-connected system is designed to be usable by a single speaker. In a speaker-independent system, it is designed to be used by any speaker and is naturally more difficult to obtain. These systems have a 3 to 5 higher error rate compared to speaker-connected systems [19]. The most common method used in SR systems is the probabilistic approach. A score is calculated for matching the expressed words to a speech signal. Any word in the vocabulary that is mentioned during the speech is compared to its probability value [20]. From the phonemes in the comparative acoustic model, which words can follow other words through grammar, are calculated. The word string with the highest score is selected as the recognition result. The SR process consists of four stages: preprocessing, feature extraction, decoding, and post-processing. The steps specified in different SR systems are implemented in different ways. In Figure 6, the four main stages are represented in detail.

### 3.1. Pre-Processing

The speech signal recorded through the microphone in the SR process is then extracted with a sampling frequency. According to the Shannon sampling theorem, if the sampling frequency is 16 kHz, the bandwidth limit can be formed to reconstruct a signal, meaning that frequencies up to 8 kHz can be correctly generated [21]. Since the data transmitted over the telephone network is in the range of 5–3.7 kHz, 8 kHz frequency generation is more than enough for speech recognition. In the speech recognition process, frequency values below 100 Hz are considered as noise and are eliminated by using a high pass filter. A significant part of preprocessing takes into account the sections between the start of the recording and the start of the user speech.

### 3.2. Feature Extraction

Acoustic observations made during the feature extraction process are extracted over uniform length time frames. The frame length is 25 ms for the signal that is considered constant between these frames. For acoustic observations in this window, the multidimensional feature vector is calculated and a fast Fourier transform is applied to the spectral field of the vector. The microphones on which speech will be recorded may differ. Therefore, linear filter effects are discarded with Cepstral Mean Subtraction (CMS) to compensate for the difference [22]. The information that can be found on the time change can be obtained by combining sequential feature vectors and creating a very high dimensional controller.

### 3.3. Decoding

The computational process in which word strings are most likely matched to feature vectors representing the acoustic signal is called decoding. In this process, there is a need for three important blocks consisting of an acoustic model containing a Hidden Markov Model (HMM) for each word or phoneme, a dictionary consisting of a word list and their phoneme strings, and a language model consisting of word probability or word strings [23]. The language model, which is not necessarily used in the decoding process, increases the success rate if it is used [24]. Usually fixed grammar or n-gram model consisting of words and probabilities; unigram, bigram, trigram model are used.

### 3.4. Post-Processing

In the last stage, the processed speech expression Viterbi is applied to the search and the best list of  $n$  is created. This list is re-scored using additional sources of information that improve the recognition accuracy of the highest-scoring result. There are more resources needed for computation and memory than unigram or bigram models. Often, the bigram model is combined with the trigram model in the recalculation.

Because of the four steps mentioned above, the processed audio is now ready to be converted into text. There are many different audio processing software packages available today that use similar processing processes. The success rate of sound processing software is inversely proportional to the minimum error rate achieved. The accuracy of human voices defined by sound libraries is measured by the Word Error Rate (WER) obtained because of sound processing [19].

$$WER = \frac{\text{Number of Substitutions+Insertions+Deletions}}{\text{Total number of words}} \quad (1)$$

In a study conducted in 2019, Microsoft Research stated that 5.1% WER was obtained in the NIST 2000 Switchboard task, 6.6% WER was obtained in the lower Switchboard cluster in the IBM Research Hub5 2000 evaluation test set, and finally, Google Research stated that 4.1% WER was obtained [26]. In another study conducted in 2017, Google Speech Recognition (GSR) and Siri, developed by Apple, were compared. In that study, 8-word samples taken from 41 people were processed through both voice recognition software, and it was determined that GSR gave much more successful results than Siri [27].

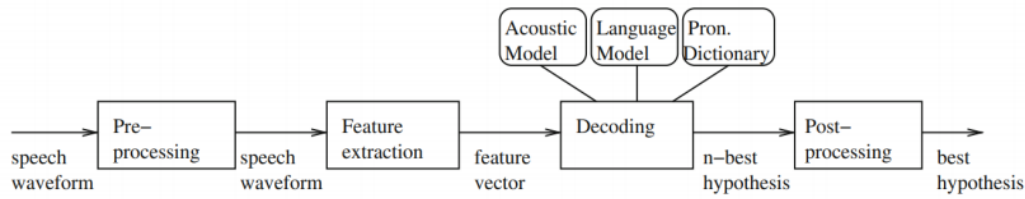


**Figure 6.** Speech Recognition process [25]

In this study, the speech recognition processes are examined, and found that GSR voice processing is successful compared to other similar softwares. In the Python software used in the prepared integrated software, GSR is called in the speech recognition library used for speech recognition, and speech expressions are processed over the GSR.

The Arduino Uno card and Mini Maestro 24 channel servomotor control card are controlled by the integrated Python and Arduino software. First of all, the user is asked to send a text message or a voice message with the right of choice. The GSR sound library is used in voice messages, and spoken messages are converted into text. In both cases, the messages obtained are sent with PySerial to the motherboard, where the Arduino software is processed via Python. Figure 6 shows the letters ASL and the movement of the humanoid robot arm. In the study, 26 letters and numbers (0–9) in English are carried out with a humanoid robot arm (table 3).

#### 4. Results and Discussion

This work focused on mechatronics and electronic design guidelines and integrated software of the humanoid robot arm. First, sign language letters that can be executed with one hand are investigated and ASL is chosen because of its applicability in this respect. The robot arm with integrated software realized all letters and numbers in ASL in Table 2.

The sound data obtained with Python or the entered




































written letters and numbers were sent to the Arduino control card with PySerial, and the comparison is made against the movement recorded on the Arduino and performed on the robot arm. There are eight bones in the human wrist to provide rotational movement. The existing eight bones are located between the forearm and comb bones and are in a structure that is connected by tight ligaments. Rotational motion of the human wrist around its axis does not seem possible in many humanoid robots today. For this reason, the representation of some letters in ASL is created in the closest form. Although there are some limitations in the robotic arm, both the printing on 3D printers and the use of open-source software in the development of the software is shown to be the prominent features of this study compared to the existing studies. The letters and numbers mentioned below with a humanoid robot arm have shown that robotic systems can be used successfully in imitating sign language.

The main features of the developed humanoid robot arm are the ability to use sign language, low development cost, and easy maintenance. The next stage of the study aims to develop a humanoid robot to teach sign language to hearing and speech-impaired children. Other units of the humanoid robot that are hoped to be developed, such as the upper arm, body, and head, are still being researched. The humanoid mobile robot to be developed will have features that can imitate the TSL. It is assumed that this work will contribute to robotic systems that can be printed with 3D printers and shared as open source, and that the work done in this field will continue.

































**Table 3.** Letters and numbers are used in American Sign Language [28]

<b>a</b>	<b>A</b>	<b>b</b>	<b>B</b>	<b>c</b>	<b>C</b>

**Table 3.** (Cont.) Letters and numbers are used in American Sign Language [28]

 d	 D	 e	 E	 f	 F
 g	 G	 h	 H	 i	 I
 j	 J*	 J*		 k	 K
 l	 L	 m	 M	 n	 N
 o	 O	 p	 P	 q	 Q
 r	 R	 s	 S	 t	 T

**Table 3.** (Cont.) Letters and numbers are used in American Sign Language [28]

 <b>U</b>	 <b>U</b>	 <b>V</b>	 <b>V</b>	 <b>W</b>	 <b>W</b>
 <b>X</b>	 <b>X</b>	 <b>Y</b>	 <b>Y</b>	 <b>Z</b>	 <b>Z</b>
 <b>0</b>	 <b>0</b>	 <b>1</b>	 <b>1</b>	 <b>2</b>	 <b>2</b>
 <b>3</b>	 <b>3</b>	 <b>4</b>	 <b>4</b>	 <b>5</b>	 <b>5</b>
 <b>6</b>	 <b>6</b>	 <b>7</b>	 <b>7</b>	 <b>8</b>	 <b>8</b>
 <b>9</b>	 <b>9</b>				

\* To symbolize the letter J in ASL, the little finger is first pointed upwards like the letter I, and after a short while the little finger closes towards the palm. This movement is raised as indicated, the little finger is lifted upwards and after 500 ms it is broken towards the palm.

## Declaration of Ethical Standards

The authors of this article declare that the materials and methods used in this study do not require ethical committee permission and/or legal-special permission.

## Conflict of Interest

The authors declare that they have no known competing financial interests or personal relationships that could have appeared to influence the work reported in this paper.

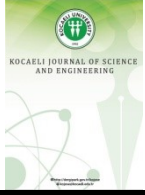
## References

- [1] Republic of Turkey Ministry of Family Labor and Social Services (Web Page: <https://www.ailevecalisma.gov.tr/media/31492/istatistik-bulteni-kasim2019.pdf>) (Date Accessed: 01.05.2020)
- [2] Alemi M., Meghdari A., Ghazisaedy M., 2014. Employing humanoid robots for teaching English language in Iranian junior high-schools. *Int. J. Humanoid Rob.* **11**(3), pp.1–25. doi: 10.1142/S0219843614500224
- [3] Alemi M., Ghanbarzadeh A., Meghdari A., Moghadam L.J., 2015. Clinical application of a humanoid robot in pediatric cancer interventions. *Int. J. Soc. Rob.*, pp. 1–17. doi:10.1007/ s12369-015-0294-y
- [4] Meghdari A., Alemi M., Taheri A., 2013. The effects of using humanoid robots for treatment of individuals with autism in Iran. In: 6th Neuropsychology Symposium, Tehran, Iran.
- [5] Mayberry R.I., 2002. Cognitive development in deaf children: the interface of language and perception in neuropsychology. In: *Handbook of Neuropsychology*, **8**(Part II), pp. 71–107
- [6] Besio S., et al., 2007. Critical factors involved in using interactive robots for play activities of children with disabilities. In: *Proceedings of AAATE 2007 on Challenges for Assistive Technology*, pp. 505–509
- [7] Janssen J.B., van der Wal C.C., Neerinx M.A., Looije R., 2011. Motivating children to learn arithmetic with an adaptive robot game. In: Mutlu, B., Bartneck, C., Ham, J., Evers, V., Kanda, T. (eds.) *ICSR 2011. LNCS*, vol. 7072, pp. 153–162. Springer, Heidelberg
- [8] Nalin M., et al., 2012. Children’s adaptation in multi-session interaction with a humanoid robot. In: 2012 IEEE on RO-MAN. IEEE
- [9] Schmitz A., et al., 2010. Design, realization and sensorization of the dexterous icub hand. In: 10th IEEE-RAS International Conference on Humanoid Robots (Humanoids). IEEE
- [10] Albers A., et al., 2006, Upper body of a new humanoid robot-the design of ARMAR III. In: 2006 6th IEEE-RAS International Conference on Humanoid Robots. IEEE
- [11] Diftler M.A., et al., 2011. Robonaut 2-the first humanoid robot in space. In: 2011 IEEE International Conference on Robotics and Automation (ICRA). IEEE
- [12] Kose H., Akalin N., Uluer P., 2014. Socially interactive robotic platforms as sign language tutors. *International Journal of Humanoid Robotics*, **11**(01), 1450003.
- [13] Köse H., Uluer P., Akalin N., Yorgancı R., Özkul A., Ince G., 2015. The effect of embodiment in sign language tutoring with assistive humanoid robots. *International Journal of Social Robotics*, **7**(4), pp.537-548.
- [14] Valli C., Lucas C., 2000. *Linguistics of American Sign Language: An Introduction*. Gallaudet University Press, Washington DC
- [15] Open-Source Thingiverse Design. <https://www.thingiverse.com/thing:2269115> (Access Time: 01/05/2020)
- [16] Design of Humanoid Robot prepared by InMoov company. <https://www.thingiverse.com/thing:17773> (Access Time: 01/05/2020)
- [17] Design of Humanoid Robot prepared by InMoov company. <https://www.thingiverse.com/thing:65274> (Access Time: 01/05/2020)
- [18] Hirose S., Umetani Y., 1978. The development of soft gripper for the versatile robot hand. *Mech. Mach. Theory*, **13**(3), pp. 351–359
- [19] Stenman M., 2015. *Automatic speech recognition An evaluation of Google Speech*, Corpus ID: 13963607, Published
- [20] Gruhn R.E, Minker W, Nakamura S, 2011. *Statistical pronunciation modeling for non-native speech processing*. Springer Science & Business Media
- [21] Jerri A.J., 1977. *The shannon sampling theoremits various extensions and applications: A tutorial*

review. Proceedings of the IEEE, **65**(11), pp. 1565–1596

- [22] Westphal M., 1997. The use of cepstral means in conversational speech recognition. In: EUROSPEECH
- [23] Rainer E. Gruhn W.M., Nakamura S., 2011. Statistical pronunciation modeling for non-native speech processing. In: Springer Science and Business Media
- [24] Tanigaki K., Yamamoto, H., Sagisaka, Y., 2000. A hierarchical language model incorporating class-dependent word models for oov words recognition. In: INTERSPEECH
- [25] Soudamalla S.K., “Implications of Conversational AI on Humanoid Robots”, site: <https://nbn-resolving.org/urn:nbn:de:bsz:ch1-qucosa2-724268>
- [26] Kim J.Y., Liu C., Calvo R.A., McCabe K., Taylor S.C.R., Schuller B.W., Wu K., 2019. A Comparison of Online Automatic Speech Recognition Systems and the Nonverbal Responses to Unintelligible Speech. arXiv.org > cs > arXiv:1904.12403
- [27] Daniels P., Iwago K., 2017. The suitability of cloudbased speech recognition engines for language learning. JALT CALL Journal, **13**(3), pp.229-239
- [28] American Sign Language. [https://en.wikipedia.org/wiki/American\\_manual\\_alphabet](https://en.wikipedia.org/wiki/American_manual_alphabet) (Access time: 01/12/2020)





## Searching for the Roots of Bloom Syndrome Protein and Its Homologs Using Phylogenetic Analysis

Tuğcan KORAK<sup>1,\*</sup> , Murat KASAP<sup>2</sup> 

<sup>1</sup> Department of Medical Biology, Faculty of Medicine, Kocaeli University, Kocaeli, 41001, Turkey, **ORCID:** 0000-0003-4902-4022

<sup>2</sup> Department of Medical Biology, Faculty of Medicine, Kocaeli University, Kocaeli, 41001, Turkey, **ORCID:** 0000-0001-8727-2096

### Article Info

#### Research paper

Received : March 03, 2021

Accepted : August 11, 2021

#### Keywords

*BLM RecQ Like Helicase (BLM)*  
*Maximum Parsimony*  
*Phylogeny*  
*Phylogenetic Tree*

### Abstract

Phylogenetic analysis (PA) is used for elucidation of relationships among different species and provides information about their evolution. BLM protein (BLM RecQ like helicase) is responsible for the repair of stalled replication fork during double-strand break repair by homologous recombination. In the current study, phylogenetic analysis was performed using BLM protein sequences, sequences of its homologs and its putative homologs from 34 species including covering the genera of Bacteria, Archaea and Eukaryotes. This study was carried out for the purpose of (1) illustrating and comparing relationships among eukaryotic BLM proteins, their homologs (ATP-dependent DNA helicase RecQs in Bacteria) and their potential putative homologs (ATP-dependent DNA helicase Hel308s in Archaea), (2) evaluating how BLM protein evolution took place, what it brought to the organisms by acquiring functional changes and how future potential changes would occur and (3) gaining the general perspective in the evolution of BLM protein. All analyzed species in Bacteria, Archaea and Eukaryota formed a clear inter-species cluster, except for *P. sinensis* (Reptilia). The results supported that Hjm helicase may be one of the candidate potential ancestors of the BLM proteins and their homologs. Moreover, especially two domains which are Helicase ATP-binding and Helicase C-terminal domain were encountered in the all analyzed species and seem to be strictly conserved in the future. Repair related-highly sophisticated interaction network of BLM indicated that its functional evolution reaches a certain level and it appears to have taken an important place in maintaining genomic stability. However, it should be taken into account that BLM may acquire additional functions or become a cornerstone in different pathways in the future depending on its participation in various metabolic roads.

## 1. Introduction

The construction of phylogenetic trees is an essential process to uncover various chemical and morphological mechanisms as well as the evolution of life [1,2]. In a similar manner, molecular phylogenetic trees which are performed for the gene or genome data are used to predict phylogeny of focused species [1]. Analysis of phylogeny has become a routine for the understanding novel gene sequences and is also used for RNA and protein sequences [3]. Moreover, the construction of universal phylogenetic trees with the three domains of life, Bacteria, Archaea,

Eukaryota, leads to an understanding of all extents of life and stages of evolutionary processes through the roots and branches up to the modern cell types. There are two fundamental perspectives of universal phylogenetic trees to facilitate deduction of evolutionary information; (1) the nature of the species represented by its root and (2) how the species bring about the primary organismal lineages [4].

BLM (BLM RecQ like helicase) helicase, which is encoded by BLM gene located on 15q26.1 [5] chromosomal region, is responsible for the repair of halted replication fork during double-strand break (DSB) repair by homologous recombination (HR). It shows DNA-stimulated ATPase activity and ATP-dependent DNA helicase activity. Also, it regulates branch migration of Holliday junctions by interacting with some other proteins

\* Corresponding Author: tugcankorak@gmail.com



for the purpose of HR completion [6,7,8]. Moreover, it contributes to the maintenance of genome integrity by resolving anaphase bridges necessary for accurate chromosome segregation [9]. In addition, BLM was reported to be associated with some tumor suppressor proteins and is thought to play a role in DNA-damage response in the BLM-TOP3A-RM1 complex [10, 11]. On the other hand, studies have shown that mutations in the *BLM* gene may cause Bloom syndrome which is a genetic disease characterized by stature, fertility problems, growth inhibition, light sensitivity and susceptibility to cancer. Moreover, it has been shown that mice models heterozygous for a number of *BLM* exons in which some of them are non-functional are more susceptible to cancer as compared to mice carrying inactivated tumour suppressor genes such as APC. Thus, haploinsufficiency in the *BLM* gene may stimulate cancer development [6,7,11].

Structural studies on BLM protein which belongs to the RecQ helicase family have revealed that it has a zinc-binding subdomain unique to the RecQ helicase family at the C-terminus of ATPase domain [12-15]. Besides, the N-terminal region has been suggested to involve in oligomerization [16]. In another study, the crystal structure of the human RecQ C-terminal (RQC) domain of BLM protein was elucidated and the results demonstrated that the BLM RQC domain has distinguished it from some other helicases in several aspects. Firstly, the C-terminal region of BLM RQC spreads throughout the domain surface. Secondly, there is no aromatic residue at the end of the  $\beta$ -wing region which is used in DNA-strand separation. Eventually, BLM-specific insertion regions located between N-terminal helices have been shown as important for an accurate angle of  $\beta$ -wing and Holliday junction resolution [17].

Considering the important tasks that BLM protein carries out in the cells, we were interested in knowing how this ubiquitous protein evolved over time. To the best of our knowledge, phylogenetic analysis of BLM protein has not been carried out previously. Thus, phylogenetic analysis was performed based on BLM proteins, their homologs and putative homologs in 34 species that are representative of three genera; Archaea, Bacteria, and Eukaryota. The constructed phylogenetic tree provided insights into BLM evolution.

## 2. Materials and Methods

### 2.1. Data Retrieval

For Bacteria (Clade 1): BLASTP software (<https://blast.ncbi.nlm.nih.gov/Blast.cgi?PAGE=Proteins>) was used to obtain homologous sequences of BLM

belonging to bacterial species. The database searched was UniProtKB/SwissProt and the query sequence used was BLM protein sequence of Gorilla gorilla gorilla (Western lowland gorilla) which is more likely to have similar sequences with primitive organisms than the human BLM sequence. All bacterial species which contained protein sequences that have functional similarities with BLM were included in this study.

For Archaea (Clade 2). Since BLM homologs of Archea species could not be obtained in the BLASTP search performed by selecting the UniProtKB/SwissProt database, functional homology search was carried out for these species in the literature. Several studies supported that archaeal Hjm helicase has recq-like functions and may play a role in the repair of stalled replication fork [18-24]. By taking this information into consideration, Hjm helicase sequences were retrieved from the UniprotKB database (<http://www.uniprot.org/>). All archaeal species which contained protein sequences that have functional similarities with BLM were included in the study.

For Eukaryotes (Clade 3): Phylum Chordata including fishes, amphibians, reptiles, birds, mammals in Animalia kingdom of Eukaryota was used in this study. BLM protein sequences were retrieved from the UniprotKB database. The data with the longest BLM sequence length for each species and with compatible to helicase function of BLM were included. Since the higher mammalian data for BLM is readily available in the databases, more of the mammalian species were taken into consideration.

### 2.2. Phylogenetic Analysis

For phylogenetic analysis, amino acid sequences were used in order to exclude compositional bias that may be encountered in DNA sequences [25] BLM amino acid sequences from 34 different organisms were retrieved from the UniprotKB database (<http://www.uniprot.org/>) and listed in Table 1.

Unrooted trees are suitable for determining the degree of inter-species similarity, whereas rooted trees, where a common ancestor is assigned, provide a clearer understanding of the evolutionary path. Fossil data are needed to construct rooted trees [26]. Since there are no fossil data for the phylogenetic analysis carried out in this study, rooted trees were constructed in order to interpret the BLM protein similarity among species better. The rooted tree was constructed using the midpoint rooting approach from the unrooted tree.

The sequences were downloaded in FASTA format and aligned with Clustal Omega (<https://www.ebi.ac.uk/Tools/msa/clustalo/>) in which

output format was chosen as PHYLIP and other parameters were remained as default.

**Table 1.** Uniprot accession numbers of the eukaryotic BLM proteins, their homologs (ATP-dependent DNA helicase RecQs in Bacteria) and their potential putative homologs (ATP-dependent DNA helicase Hel308s in Archaea), and the organisms to which the sequences belong.

<b>Bacteria</b>	<b>UniprotKB No.</b>	<b>Species</b>	
	P15043	<i>Escherichia Coli (E. Coli)</i>	strain K12
	O34748	<i>Bacillus subtilis (B. subtilis)</i>	strain 168
	P40724	<i>Salmonella typhimurium (S. typhimurium)</i>	strain LT2 / SGSC1412 / ATCC 700720
	Q9CL21	<i>Pasteurella multocida (P. multocida)</i>	strain Pm70
	P71359	<i>Haemophilus influenza (H. influenzae)</i>	strain ATCC 51907 / DSM 11121 / KW20 / Rd
<b>Archaea</b>	O73946	<i>Pyrococcus furiosus (P. furiosus)</i>	strain ATCC 43587 / DSM 3638 / JCM 8422 / Vc1
	Q974S1	<i>Sulfurisphaera tokodaii (S. tokodaii)</i>	strain DSM 16993 / JCM 10545 / NBRC 100140 / 7
	Q5JGV6	<i>Thermococcus kodakarensis (T. kodakarensis)</i>	strain ATCC BAA-918 / JCM 12380 / KOD1
	U3TB36	<i>Aeropyrum camini (A. camini)</i>	SY1 = JCM 12091
	D1Z2D5	<i>Methanocella paludicola (M. paludicola)</i>	strain DSM 17711 / JCM 13418 / NBRC 101707 / SANAE
<b>Eukaryota</b>		<b>Fishes</b>	
	E7EZY7	<i>Danio rerio (D. rerio)</i>	Zebrafish
	A0A3B3H755	<i>Oryzias latipes (O. latipes)</i>	Japanese rice fish / Japanese killifish
	A0A1S3KNZ2	<i>Salmo salar (S. salar)</i>	Atlantic salmon
		<b>Amphibians</b>	
	Q9DEY9	<i>Xenopus laevis (X. laevis)</i>	African clawed frog
	A0A6I8PXE0	<i>Xenopus tropicalis (X. tropicalis)</i>	Western clawed frog
		<b>Reptilia</b>	
	G1KPR4	<i>Anolis carolinensis (A. carolinensis)</i>	Green anole
	A0A452GZE4	<i>Gopherus agassizii (G. agassizii)</i>	Agassiz's desert tortoise
	K7FS17	<i>Pelodiscus sinensis (P. sinensis)</i>	Chinese softshell turtle
		<b>Aves</b>	
	U3IGZ2	<i>Anas platyrhynchos (A. platyrhynchos)</i>	Mallard
	U3K8X3	<i>Ficedula albicollis (F. albicollis)</i>	Collared flycatcher
	Q9I920	<i>Gallus gallus (G. gallus)</i>	Chicken
		<b>Mammalians</b>	
	G1M5K3	<i>Ailuropoda melanoleuca (A. melanoleuca)</i>	Giant panda
	E1BQ04	<i>Bos taurus (B. taurus)</i>	Domestic cow
	J9PB86	<i>Canis lupus familiaris (C. l. familiaris)</i>	Dog
	F6ZL78	<i>Equus caballus (E. caballus)</i>	Horse
	P54132	<i>Homo sapiens (H. sapiens)</i>	Human
	O88700	<i>Mus musculus (M. musculus)</i>	House Mouse
	G1PQL6	<i>Myotis lucifugus (M. lucifugus)</i>	Little brown bat
	W5PTL9	<i>Ovis aries (O. aries)</i>	Sheep
	D3ZQW1	<i>Rattus norvegicus (R. norvegicus)</i>	Brown rat
	G3W1C2	<i>Sarcophilus harrisii (S. harrisii)</i>	Tasmanian devil
	H2QA33	<i>Pan troglodytes (P. troglodytes)</i>	Chimpanzee
	G3QXK2	<i>Gorilla gorilla gorilla (G. g. gorilla)</i>	Western lowland gorilla
	F1RMJ2	<i>Sus scrofa (S. scrofa)</i>	Pig

The sequence data were bootstrapped using SEQBOOT for 1000 times by randomly selecting columns from the original alignment to infer the reliability of the trees [27]. PROT-PARS program was used to construct trees with maximum parsimony method (multiple data sets or multiple weights: D, The number of data sets: 1000, Random number seed: 3, Number of times to jumble: 5). Consequently, CONSENSUS program was used to produce majority rule consensus trees and RETREE program was used to assign midpoint to the rooted tree. Finally, DRAWTREE and DRAWGRAM were used to construct unrooted and rooted trees, respectively. The outputs of DRAWTREE or DRAWGRAM were used in Adobe Illustrator 2020 to create the figures for publication.

### 2.3. The Domain and Biological Function Search in the UniprotKB Database

Since the algorithms used for domain identification have some assumptions on the principles of the evolutionary process [28], we initially scanned domain information of all analyzed proteins in sequence depositories. To contribute to the evolutionary history of BLM, we scanned manually the protein domains of Hjm helicase, BLM homologs and BLM proteins in the UniprotKB database (<https://www.uniprot.org/>) for all the selected species of Archaea, Bacteria and Eukaryota, respectively. The UniprotKB numbers of the species were inputted and the domains of each related protein were listed under the “Domains and Repeats” section. In addition, to assess the major biological functions of the analyzed proteins, the “GO - Biological process” section was analyzed for each protein sequence. The elucidated information was used to understand the fundamental aspects of BLM protein evolution.

### 2.4. Identification of Domains and Motifs

PFAM database contains large protein families represented by multiple sequence alignments and hidden Markov models. It is used for the classification of domains and protein families; therefore, it helps understand the function of targeted proteins [29]. To expand and support the data obtained from Uniprot KB domain search, we identified the domains and motifs using the Pfam database (Pfam 33.1, 18259 entries: <http://pfam.xfam.org/>). The FASTA format of protein sequences belonging to Hjm helicase, BLM homologs and BLM proteins for all analyzed species in Archaea, Bacteria and five selected species in Eukaryotes were used as the input sequences. One species was selected from each class (Fishes: *D. rerio*, Amphibians: *X. laevis*, Reptilia: *A. carolinensis*, Aves: *A.*

*platyrhynchos*, Mammalians: *H. sapiens*) to create five representative species of Eukaryota. Consequently, “Significant Pfam-A Matches” were included in the analysis and Adobe Illustrator 2020 was used to combine and edit the results.

### 2.5. BioGrid and STRING Analysis

The BioGrid and STRING analyses were carried out to obtain predicted interaction networks of BLM protein with other proteins. The BioGrid (<https://thebiogrid.org/>) and STRING analysis (<https://string-db.org/>) of BLM was performed by selecting *H. Sapiens* as the target organism. A minimum evidence level of 1 was set as the stringency level in BioGrid analysis. The results were exported in PNG format.

## 3. Results and Discussion

Phylogenetic analysis is carried out to exhibit relatedness among species and to obtain important insights into the evolution of molecular sequences. General principles derived from PA also lead to predicting future changes in DNA or protein sequences. In general, phylogenetic analysis are used in affiliating taxonomy to an organism, pathogen identification, forensic medicine and determining the cryptic speciation in a species [2, 3, 30]. In the current study phylogenetic analysis of BLM protein was performed for 34 species which include the representative species from three clades, Bacteria, Archaea and Eukaryota. Rather than discussing each proximal or binary relationship and explaining their basements, our aim is to gain an overview of the BLM protein evolution. Based on the analysis of the phylogenetic tree together with the other analysis carried out, evolutionary history and the potential fate of BLM protein will be inferred.

The molecular phylogenetic analysis generated by ribosomal RNA (rRNA) sequences specified the phylogenetic relationships among three domains of life; Bacteria, Archaea and Eukaryota. Apart from rRNA, orthologous genes have been used to construct a phylogenetic tree of life; however, the tree resolution permitted by a single gene remains at the minimum level [31]. Protein sequences can also be preferred in molecular evolution researches depending on their several advantageous aspects. Even if all information required for proteins is found in DNA sequences, the natural selection process does not often directly occur on DNA. However, proteins are the main building blocks and essential components of life on which natural selection occurs. In addition, while four bases create DNA sequences, functional characteristics of proteins are defined by 20

amino acids which bring about much higher resolution in the phylogeny of evolutionary distantly related organisms [32]. Hence, we constructed the phylogenetic tree using protein sequences to evaluate BLM protein evolution in the tree domain of life by considering its homologs (ATP-dependent DNA helicase RecQs in Bacteria) and its potential homologs (ATP-dependent DNA helicase Hel308s in Archaea) processing stalled replication fork.

### 3.1. Evaluation of Phylogenetic Trees for Elucidation of Relationships Among BLM Proteins

The proximal and distal relationships that were attributed to the species were based on the amino acid sequences of BLM proteins or their homologs or Hjm helicase. In both unrooted and rooted trees, three clades were created. As expected, each clade was formed by the species belonging to the corresponding genus. The clade formed by the bacterial species was more closely related to the species formed by the archaeal ones. The eukaryotes, on the other hand, formed a more distantly related clade. The archaeal species were more closely related to the eukaryotes than the bacterial clade. However, there appeared to be some species that carried the transition form of the protein and thus found a place on the tree between the archeal and the eukaryotic clades. Those species were *A. carolinensis*, *G. agassizii*, *A. platyrhynchos*, *G. gallus* and *F. albicollis*.

By using midpoint rooting, a rooted tree was created that provides a better illustration of relationships among species. (Figure 1 and 2). Except for the bootstrap value (352.3) for *E. caballus* and *A. melanoleuca-C. l. familiaris*, the majority of other bootstrap values represented above the nodes were obtained as 1000 or close to 1000.

For Clade 1 (Bacteria): All species revealed distant relationships with other clades. Close binaries were revealed between *H. influenza* and *P. multocida* as well as *S. typhimurium* and *E. Coli*. *B. subtilis* were obtained as less close in terms of BLM homologs (Figure 1 and 2).

For the Clade 2 (Archaea): All species revealed distant relationships with other clades (Figure 1 and 2). Close binaries were revealed between *S. tokodaii* and *A. camini*. *T. kodakarensis* were obtained as less close in terms of Hjm helicases (Figure 2).

For the Clade 3 (Eukaryota): Species belonging to different classes in phylum Chordata were assigned to their own classes, except for *P. sinensis* (reptilia) which is acquired as more closely related to the species of Bacteria. In mammals, the closest relative of *H. Sapiens* was *P. troglodytes*, and *S. harrisii* was observed as the most distant relative of all species in the mammalian class. Other close binaries in the mammalian class were as follows: *A. melanoleuca-C. l. familiaris*, *O. aries-B. taurus* and *M. musculus-R. norvegicus*. The species of Amphibians, Fishes and Aves were seen as more close relatives as compared to other classes in terms of BLM protein (Figure 1 and 2).

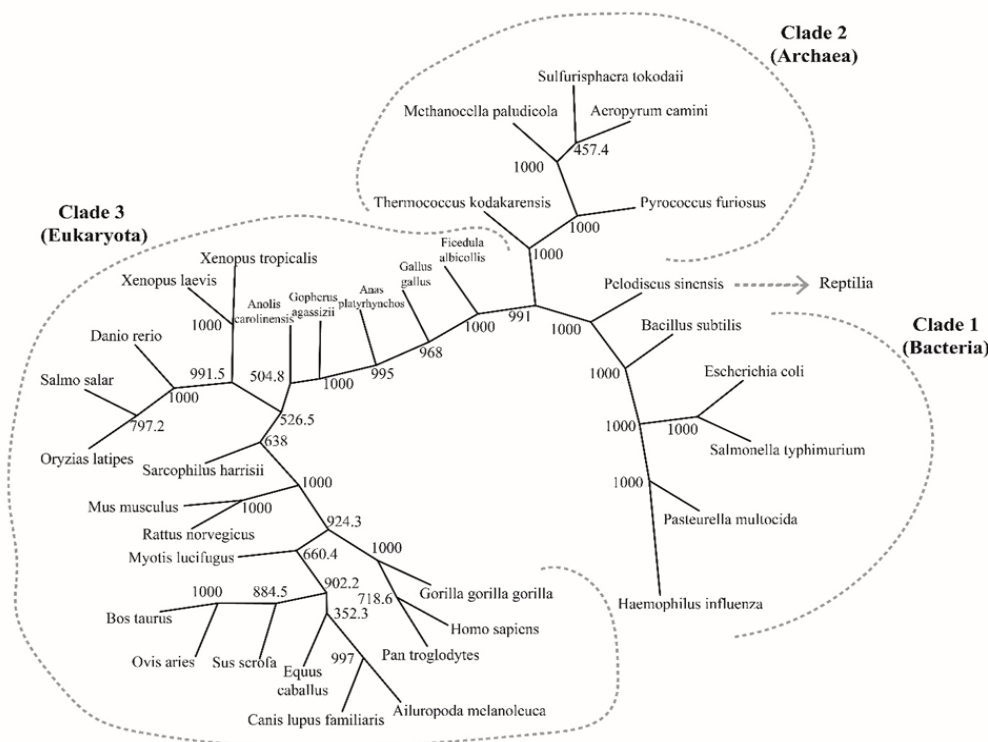


**Figure 1.** Unrooted maximum parsimony tree constructed for BLM amino acid sequences and its homologs of 34 different species in Bacteria, Archaea, and Eukaryota. Numbers near the nodes are bootstrap values.

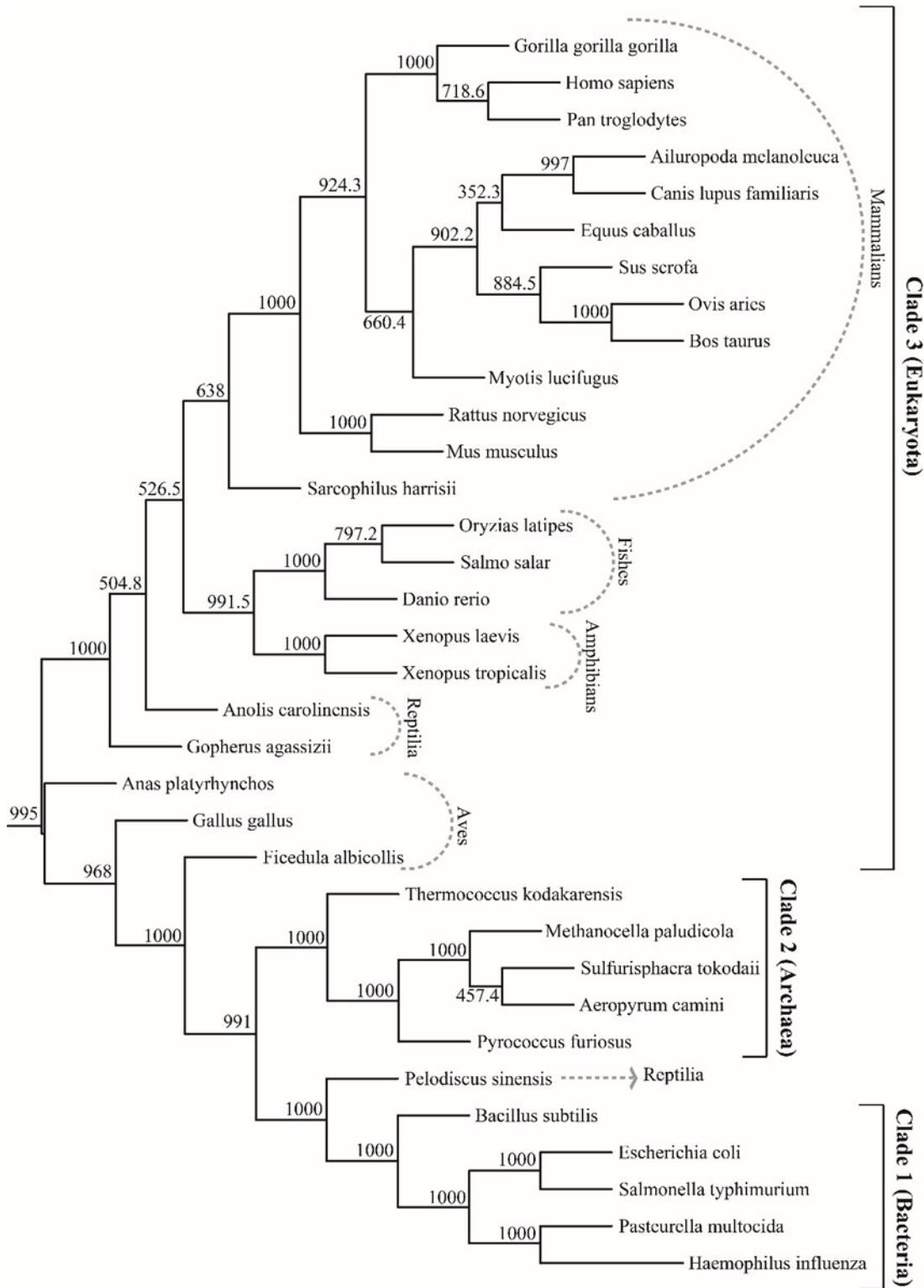


**Figure 2.** Rooted maximum parsimony tree constructed for BLM amino acid sequences and its homologs of 34 different species in Bacteria, Archaea, and Eukaryota. The different classes including mammals, amphibians, fishes, reptilians and aves in phylum chordata were indicated. Numbers near the nodes are bootstrap values.

Both rooted and unrooted trees are suitable for determining the degree of inter-species similarity, whereas rooted trees provide a clearer understanding of the evolutionary path by representing ancestral species [26, 33]. In general, the fossil data are necessary to predict

divergence dates and also to generate rooted tree [26]. On the other hand, unrooted trees are frequently constructed when there is no sufficient information to assign the root and they still offer insights into evolutionary relationships of organisms without ancestral perspective [33]. Since

there are no fossil data in this phylogenetic analysis, we generated a rooted tree to interpret the notion of evolution of BLM protein better. Also, an unrooted tree was constructed to consider and to reveal the possible alternative root nodes, besides investigating the relatedness of BLM protein among organisms. The generated rooted and unrooted trees commonly demonstrated binary phylogenetic relatedness of organisms in terms of BLM proteins and their homologs (Figure 1 and 2). The bootstrap values represented near the nodes provide to evaluate the reliability of the phylogenetic trees. The bootstrap values of 95% or greater specify statistically significant and mean “support” for a clade while the values less than 5% indicate the rejection of a node. However, the values should not be evaluated as the measurement of the truth or accuracy of the phylogeny. They imply the repeatability rather than accuracy of the phylogenetic trees [27]. In the phylogenetic analysis of BLM protein, the node of *E. caballus* and *A. melanoleuca-C. l. familiaris* has the lowest bootstrap value as 352.3, while the majority of others were obtained as 1000 or close to 1000. Although it is not possible to state clearly, the low bootstrap values may be due to the increased taxon sample size [34]. The majority of our branching points were supported by high or moderate bootstrap values (Figures 1 and 2).

Due to the dense species sampling within the mammals in Eukaryota detailed aspects of the BLM protein evolution in mammalian species were obtained (Figures 1 and 2). The closest relative of *H. Sapiens* was found as *P. troglodytes* (chimpanzees). It is possible to associate this unsurprising result with the many phenotypic and genomic similarities that exist between the two species. The whole-genome divergence between two species was reported as approximately 4% resulting from ~1.23% single-nucleotide divergence and ~3% insertion-deletion events. Nearly one of the third proteins is identical and the typical protein alters only by two amino acids. Moreover, orthologous proteins of these two species are still highly similar and less than 1% difference is valid for amino acid sequences [35]. This data explains the closest relationships of BLM protein in these organisms. On the other hand, *G. g. gorilla* (gorilla) was found as branching off *H. Sapiens* and *P. troglodytes*. One of the experimental studies supported these results by demonstrating less divergence for selected DNA segments in *H. Sapiens-P. troglodytes* than *H. Sapiens-G. g. gorilla*. Also, the divergence of *G. g. gorilla-H. Sapiens* was estimated as 1.6-2.2 million years earlier than *H. Sapiens* and *P. troglodytes* divergence [36]. Thus, it seems to be valid for BLM protein evolution among these tree species. Furthermore, the accumulated data obtained from various molecular studies indicate that the transcription factors and the genes related to neural functioning, sexual

reproduction, immunity and cell recognition and olfactory receptors evolved faster or evolved under strong positive selection or have different activation states during human speciation and/or after divergence [37-43]. Since the molecular and functional state of BLM protein does not overlap these phenomena, the rate of BLM evolution may proceed at a certain level.

One of the sources of the gene/genome evolution is transposable elements which can lead to mutations, insertions, deletions, rearrangements, copy number variations, etc [44, 45]. The activity of transposable elements (TEs) is strictly regulated by histone modification, DNA methylation and piRNAs. Long interspersed nuclear element-1 (LINE-1) is the member of the class I TE and nearly all LINE-1s are inactive in humans, except for nearly 80-100 ones [46, 47]. However, all LINE-1 elements of *S. harrisii* (Tasmanian devil) were suggested to be nonfunctional. In addition, the Hidden Markov Model strategy supported that the potential sources of functional reverse transcriptase which plays a key role in the mobilization of retrotransposons lack in the *S. harrisii*'s genome [44]. Along a similar line with this background, *S. harrisii* was observed as the most distant relative of all species in mammalian class in terms of BLM protein. Considering less evolutionary changes depending on inactive LINE-1 and lacking functional reverse transcriptase in the genome, BLM protein may firstly branch off right after other classes in Eukaryota.

The evolutionary order of the classes in phylum Chordata from earliest to latest is as follows: Fishes, Amphibians, Reptilia/Aves and Mammalians [48]. The constructed rooted tree did not contain information about the time of evolution, and the order was obtained as Aves/Reptilia, Fishes, Amphibians and Mammalians for BLM protein (Figure 2). Even if the tree was generated with predictions about evolutionary time, the compatible class order might not be obtained. In fact, it should not be considered as an unusual situation depending on the nature of evolution which refers to a process leading to alterations in the genetic material of a population over time. Evolution occurs in different states; one is microevolution that reflects alterations in DNA sequences and allele frequencies within a species over time, and the other one is macroevolution that covers large-scale changes at the species level following the collection of plentiful small alterations on account of microevolution [49]. Given this information, the evolution of the BLM gene/protein and the selected organisms may not proceed directly proportional. It could be one of the reasons why BLM protein of *P. sinensis* (Chinese softshell turtle) was not obtained in its own class, Reptilia, but rather a close relative to bacterial BLM homologs. Although it has been rarely documented and accepted, this result may be a sign

of horizontal gene transfer (HGT) between Bacteria and the Eukaryota. HGT is the movement of genetic material within and/or across species and may occur in all possible directions among three clades [50, 51]. It is an essential force that modulates evolution in the prokaryotes and certain eukaryotes [51]. After HGT events take place from Bacteria to Eukaryota, genes may retain pre-existing functions or provide the eukaryotic recipients with new functions such as protection, nutrition, or adaptation to extreme conditions. Even if HGT between Bacteria and Eukaryota is a controversial event, it should be considered during inferring phylogenetic trees [52]. Thus, closer relatedness of BLM protein in *P. sinensis* to its bacterial homologs might be depending on HGT events from Bacteria to Eukaryota. After that, the evolution to the current BLM gene and thereafter BLM protein may be driven by the evolution mechanisms including mutations, single-nucleotide alterations, gene flow, genetic drift and natural selection in which they enable also the other species to be positioned in the phylogenetic trees [49, 51]. Since each evolutionary approach is valuable to evaluate BLM protein evolution, this rare event should also be taken into account. From another point of view, it is always possible that multiple sequence alignment of a large sequence may result in inaccurate phylogeny depending on misleading signals that are not historically essential [53].

### 3.2. Domain and Functional Search in UniprotKB

Motifs and domains are functionally essential and evolutionary highly conserved parts of proteins. Motifs (e.g. helix-loop-helix motifs, helix-turn-helix, zinc finger, leucine zipper, helix-hairpin helix) are generally shorter sequences defining the specific functions, whereas domains refer to compact and independently folded structures of proteins and can possess motifs within boundaries. Both are the units of evolution in which they lost, gained, or shuffled as one module [54-56]. According to the knowledge of amino acid sequence, atomic structure and biochemical function of the domain are determined, and this provides an essential perspective to domain evolution. Alterations in the amino acid sequences may result in new protein architectures as well as new folds and functional patterns. They offer valuable aspects to establish evolutionary relationships and to infer phylogenies [28, 57].

Following the protein domain search of Hjm helicase, BLM homologs and BLM proteins in the UniprotKB database for all analyzed species, it was revealed that two domains which are Helicase ATP-binding and Helicase C-terminal were encountered in the all selected 34 species.

Three domains- Helicase ATP-binding, Helicase C-terminal and The helicase and RNaseD C-terminal (HRDC)- were detected in all selected species of Bacteria and nearly all species of Eukaryota, except for BLM protein of *G. agassizii* (Agassiz's desert tortoise) and *M. lucifugus* (Little brown bat) in which they contain two following domains; Helicase ATP-binding and Helicase C-terminal (Table 2). These results supported the possibility that Hjm helicase is the ancestor of the BLM protein depending on its common domains (Figure 2). Moreover, these tree domains which are related to helicase functions seem to be very critical for BLM function. It could be deduced that these domains may be preserved in the future and any mutation affecting these domains could alter the BLM function and may affect the natural selection of species. While the DNA repair-focused mechanisms of Hjm helicase have been reported in the UniprotKB database, we have encountered that BLM participates in biological processes on both DNA repair and maintaining genome integrity in a complicated way in Bacteria and especially in Eukaryota. Furthermore, the additional functions such as regulation of cyclin-dependent protein serine/threonine kinase activity, regulation of signal transduction by p53 class mediator, positive regulation of alpha-beta T cell proliferation, negative regulation of thymocyte apoptotic process and protein homooligomerization were declared in this database in some species of Eukaryota. These indicate that BLM will probably continue to conserve genome integrity; furthermore, it may gain different additional functions in the future.

**Table 2.** The UniprotKB domain search of phylogenetically analyzed proteins (BLM proteins, BLM homologs and Hjm helicase) of the species in Archaea, Bacteria and Eukaryota.

	Helicase ATP-binding	Helicase C-terminal	HRDC
<b>Archaea</b>	+	+	
<b>Bacteria</b>	+	+	+
<b>Eukaryota</b>	+	+	+*

+ indicates the presence of domains. \*There is an exception for BLM protein of *G. agassizii* and *Myotis lucifugus* species. They contain only two domains Helicase ATP-binding and Helicase C-terminal.

On the other hand, when the biological functions of analyzed proteins for each species in, Bacteria, Archaea and Eukaryota were evaluated, the DNA repair and genome integrity maintenance related tasks are the major for all organisms. Moreover, the complexity of the involved biological process revealed an increasing trend



for the species of the following clades in order; Archaea, Bacteria and Eukaryota.

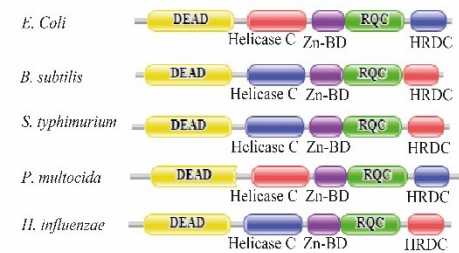
### 3.3. Classification of Domains and Motifs in PFAM Database

Since domains and motifs provide fundamental evolutionary insights on the identification of the sequences and functions of proteins [54], we expanded our work with the Pfam database in selected 15 species as the representatives of Bacteria, Archaea and Eukaryota. Helix-hairpin-helix motifs which are involved in DNA binding without sequence specificity and some enzymatic activities [58] were acquired only in the species of Archaea (Figure 3). While DEAD (corresponding to the region of Helicase ATP-binding encountered in UniprotKB database) and Helicase C-terminal were obtained in the all analyzed species, four domains- DEAD, Helicase C-terminal, Zn-BD, RQC and HRDC- were found in all species of Bacteria and all analyzed species of Eukaryota (Figure 3). When the position of DEAD domain in all analyzed proteins within Pfam was compared to the position of Helicase ATP-binding domain which was encountered as conserved in UniprotKB database, their positions were detected as overlapped. Thus, the conserved domain results of both databases are compatible with each other's. Hjm helicase was detected to contain two common domains with the other analyzed helicases in Bacteria and Eukaryota and observed to consist a low number of domains as compared to the others. Thus, Pfam results also supported that it has a potential ancestral relationship with BLM protein. Besides the other two, especially DEAD and Helicase C terminal domains seem to be highly conserved during evolution. DEAD box containing proteins that can utilize ATP hydrolysis is vital for nearly all cellular activities in which DNA or RNA is involved [59]. Helicase C terminal, Zn-BD (the domain including Zinc-finger motif), RQC domains and HRDC domain are important for protein localization, DNA binding and protein conformation, dsDNA binding and structural integrity, and the assistance in nucleic acid binding and RecQ substrate specificity, respectively [60-63]. Given those roles, they seem to become the main blocks of BLM proteins and their homologs. Also, it can be deduced that the correct positioning of the enzymes was ensured by these additional domains in Bacteria and Eukaryota.

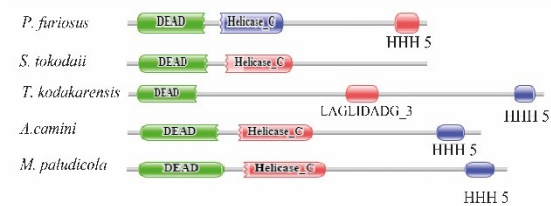
On the other hand, N-terminal domains have only appeared in Eukaryota. The N-terminal domain of BLM was reported to interact variety of proteins (e.g., BRCA1, Exo1, ATM, TOP3 $\alpha$  and DNA2-RPA-MRN complex) and they are generally controlled by phosphorylation mechanisms. Even if it has importance for cellular events,

the structure of the N-terminal has not been elucidated in detail yet. One of the studies revealed that the N-terminal domain is loosely structured, lacking conserved three-dimensional structures and it is highly divergent in terms of sequence and structure. In contrast, the BDHCT domain is highly conserved and contributes to BLM oligomerization [62]. Therefore the fewer data available for enzymatic and structural features of the N-terminal domain which is only appeared in analyzed species of Eukaryota suggested that this domain could be the potential region that may involve or explain the complex interaction network of BLM protein (Figure 3 and 4).

#### Bacteria - BLM Homologs



#### Archaea - Hjm Helicases



#### Eukaryota - BLM proteins

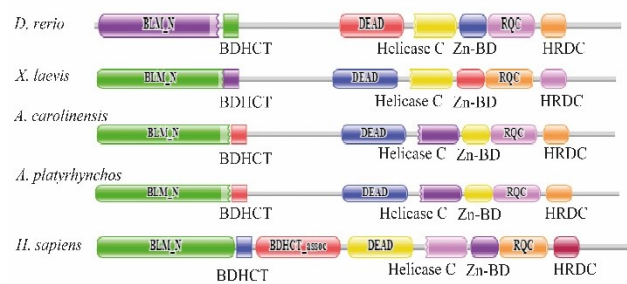


**Figure 3.** Identification of domains and motifs of BLM homologs, Hjm helicases and BLM proteins in Pfam database for the analyzed species in Bacteria and Archaea as well as five selected species in Eukaryota. (DEAD: DEAD/DEAH box helicase, LAGLIDADG\_3: LAGLIDADG-like domain, Helicase C: Helicase conserved C-terminal domain, HHH 5: Helix-hairpin-helix domain, Zn-BD: RecQ zinc-binding domain, RQC: RecQ C-terminal domain, HRDC: The helicase and RNaseD C-terminal, BLM\_N: N-terminal region of Bloom syndrome protein, BDHCT: BDHCT (NUC031) domain, BDHCT\_assoc: BDHCT-box associated domain).

### 3.4. BioGrid and STRING Analysis

Besides these various mentioned BLM functions, studies, and database information, we performed BioGrid analysis that also emphasizes the importance of this unique protein by predicting 173 potential interactors and 371 interactions. It has been observed that a significant number of these are proteins responsible for DNA repair and preserving genome integrity (Figure4).

On the other hand, STRING analysis demonstrated the specific and meaningful possible protein associations of BLM protein. The analysis predicted that BLM has 10

different functional partners which are RPA3 (Replication protein A3), MLH1 (MutL homolog 1), RPA1 (Replication Protein A1), FANCM (Fanconi anemia group M protein), APITD1 (apoptosis-inducing, TAF9-like domain 1), RMI1 (RecQ-mediated genome instability protein 1), C14orf70 (Fanconi anemia core complex-associated protein 100), RPA2 (Replication protein A2), FANCG (Fanconi anemia group G protein), FANCA (Fanconi anemia group A protein). These predicted functional partners play a role in DNA repair, cellular response to DNA damage and genome stability (Figure 5).

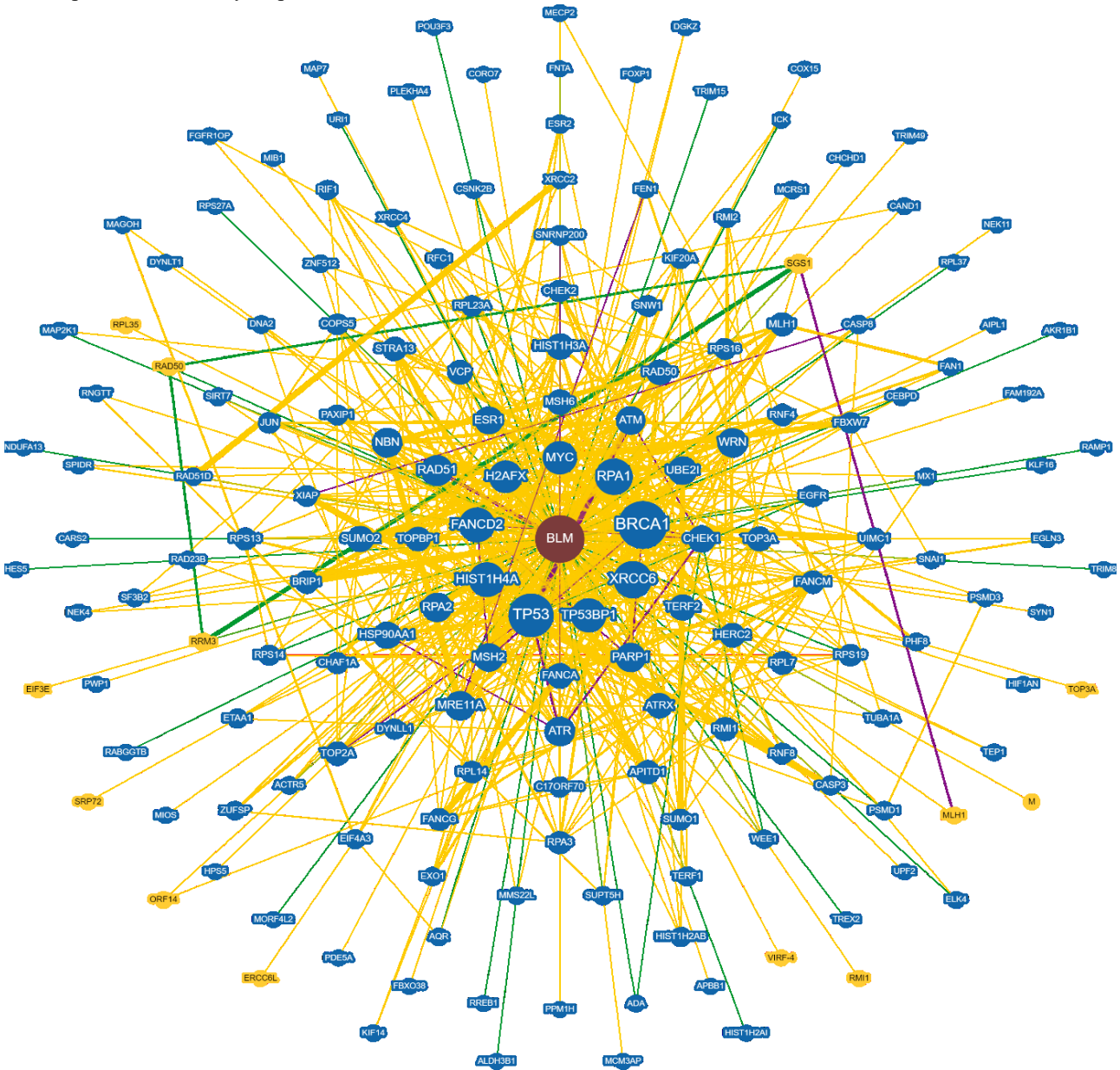


**Figure 4.** Interactome analysis of BLM protein generated by using BioGrid analysis. The complex interaction network of BLM was demonstrated. The yellow, green and purple lines indicated physical, genetic and physical/genetic interactors, respectively. BioGrid analysis of BLM protein in *H. sapiens* revealed that it totally has 173 potential interactors including 126 physical interactors, 45 genetic interactors and 2 physical/genetic interactors and 371 interactions.

Although BLM has interactors with variable functions, it majorly interacts with genome integrity and/or repair associated proteins such as exonucleases, ligases, histone proteins, checkpoint kinases, topoisomerases, recombinases, dyneins, kinesins, etc. related-highly sophisticated interaction network This repair indicates that functional evolution of BLM reaches to a certain level and it appears to have taken an important place in maintaining

genomic stability. However, it should be taken into account that BLM may acquire new functions or become a cornerstone in different pathways in the future due to its various possible metabolic roads to connect distantly related proteins including interferon regulatory factor, diacylglycerol kinases, ubiquitin-conjugating enzymes and ribosomal proteins.

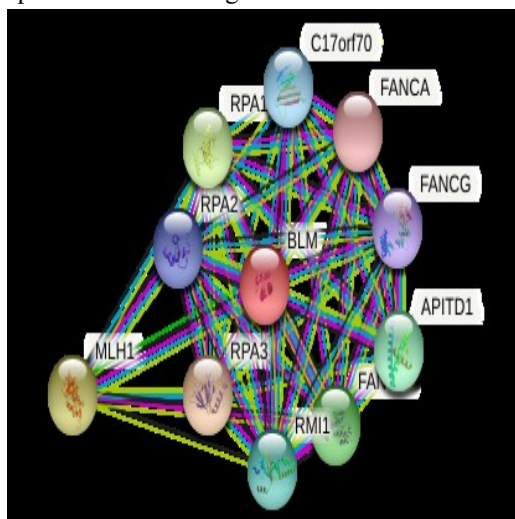


**Figure 5.** The possible protein interactions network of BLM protein is elucidated by STRING analysis. The light blue and purple lines represent the known interactions in which data were retrieved from curated databases and experiments, respectively. The green lines represent gene neighborhoods from predicted interactions. The yellow and black lines represent the textmining and co-expression data, respectively.

#### 4. Conclusions

All in all, the universal phylogenetic tree construction for a targeted protein opens the doors from the past to the current time. This approach also provides a broad perspective on the notion of evolution as well as the future fate of the focused protein. However, there are some challenges faced by researchers when they attempt to establish science-based and logical associations between the homologous or potentially homologous proteins belonging to quite different organisms living in absolutely different conditions and/or creations. For instance, the BLM protein of *P. sinensis* (reptilia, Chinese softshell turtle) in our study was acquired as more closely related to the Bacteria. Contributing to understanding the evolution of the BLM protein, the current study indicated that H<sub>2</sub> helicase may be one of the candidate potential ancestors of the BLM proteins or their homologs. Moreover, especially two domains-Helicase ATP-binding (or DEAD domain) and Helicase C-terminal BLM proteins- encountered in all species seem to be strictly conserved in the future besides the HRDC domain encountered only in Bacteria and Eukaryota. Therefore, BLM protein is also open to the evolution of a new domain related to helicase function.

Considering its highly sophisticated network, BLM protein may acquire additional functions or play a key role in other cellular networks. To clarify these data phylogenetic analysis could be extended with much more species; moreover, it could be supported by DNA data or different algorithms that predict the evolutionary time of BLM proteins or their homologs. Furthermore, comparative experimental functional analysis can be performed to illustrate how molecular evolution affects the biological function of BLM among species.

#### Declaration of Ethical Standards

The authors of this article declare that the materials and methods used in this study do not require ethical committee permission and/or legal-special permission.

#### Conflict of Interest

The authors declare that they have no known competing financial interests or personal relationships that could have appeared to influence the work reported in this paper.

## References

- [1] Horiike T., Minai R., Miyata D., Nakamura Y., Tateno Y., 2016. Ortholog-Finder: A Tool for Constructing an Ortholog Data Set. *Genome Biology and Evolution*, **8**, pp. 446-457.
- [2] Soltis D.E., Soltis, P.S., 2003. The role of phylogenetics in comparative genetics. *Plant physiology*, **132**, pp.1790–1800.
- [3] Holder M., Lewis P.O., 2003. Phylogeny estimation: traditional and Bayesian approaches. *Nature Reviews. Genetics*, **4**, pp. 275-84.
- [4] Woese C.R., 2000. Interpreting the universal phylogenetic tree. *Proceedings of the National Academy of Sciences of the United States of America*, **97**, pp. 8392–8396.
- [5] BLM, Bloom syndrome RecQ like helicase. <https://ghr.nlm.nih.gov/gene/BLM#location>. Accessed October 20, 2020.
- [6] Ding S.L., Yu J.C., Chen S. T., Hsu G.C., Kuo S.J., Lin Y.H., Wu P.E., Shen, C.Y., 2009. Genetic variants of BLM interact with RAD51 to increase breast cancer susceptibility. *Carcinogenesis*, **30**, pp. 43–49.
- [7] Shen M., Menashe I., Morton L.M., Zhang Y., Armstrong B., Wang S.S., Lan Q., Hartge P., Purdue M.P., Cerhan J.R., Grulich A., Cozen W., Yeager M., Holford T.R., Vajdic C.M., Davis S., Leaderer B., Krickler A., Severson R.K., Zahm S.H., Chatterjee N., Rothman N, Chanock S.J., Zheng T., 2010. Polymorphisms in DNA repair genes and risk of non-Hodgkin lymphoma in a pooled analysis of three studies. *British journal of haematology*, **151**, pp. 239–244.
- [8] Karow J.K., Constantinou A., Li J.L., West S.C., Hickson I.D., 2000. The Bloom's syndrome gene product promotes branch migration of holliday junctions. *Proceedings of the National Academy of Sciences of the United States of America*, **97**, pp. 6504–6508.
- [9] Frank B., Hoffmeister M., Klopp N., Illig T., Chang-Claude J., Brenner H., 2010. Colorectal cancer and polymorphisms in DNA repair genes WRN, RMI1 and BLM. *Carcinogenesis*, **31**, pp. 442–445.
- [10] Wang Z., Xu Y., Tang J., Ma H., Qin J., Lu C., Wang X., Hu Z., Wang X., Shen H., 2009. A polymorphism in Werner syndrome gene is associated with breast cancer susceptibility in Chinese women. *Breast cancer research and treatment*, **118**, pp. 169–175.
- [11] Broberg K., Huynh E., Schläwicke Engström K., Björk J., Albin M., Ingvar C., Olsson H., Höglund, M., 2009. Association between polymorphisms in RMI1, TOP3A, and BLM and risk of cancer, a case-control study. *BMC cancer*, **9**, pp. 140.
- [12] Vindigni A., Marino F., Gileadi, O., 2010. Probing the structural basis of RecQ helicase function. *Biophysical Chemistry*, **149**, pp. 67–77.
- [13] Pike A.C., Shrestha B., Popuri V., Burgess-Brown N., Muzzolini L., Constantini S., Vindigni A., Gileadi O., 2009. Structure of the human RECQ1 helicase reveals a putative strand-separation pin. *Proceedings of the National Academy of Sciences of the United States of America*, **27**, pp. 1039-1044.
- [14] Bernstein D.A., Zittel M.C., Keck J.L., 2003. High-resolution structure of the E.coli RecQ helicase catalytic core. *The EMBO Journal*, **22**, pp. 4910–4921.
- [15] Hoadley K.A., Keck J.L., 2010. Werner helicase wings DNA binding. *Structure*, **18**, pp. 149–151.
- [16] Beresten S.F., Stan R., van Brabant A.J., Ye, T., Naureckiene, S., Ellis, N. A., 1999. Purification of overexpressed hexahistidine-tagged BLM N431 as oligomeric complexes. *Protein Expression and Purification*, **17**, pp. 239-248.
- [17] Kim S.Y., Hakoshima T., Kitano K., 2013. Structure of the RecQ C-terminal domain of human Bloom syndrome protein. *Scientific Reports*, **21**, pp. 3294.
- [18] Fujikane R., Shinagawa H., Ishino Y., 2006. The archaeal Hjm helicase has recQ-like functions, and may be involved in repair of stalled replication fork. *Genes to cells : devoted to molecular & cellular mechanisms*, **11**(2), pp. 99–110.
- [19] Guy C.P., Bolt E.L., 2005. Archaeal Hel308 helicase targets replication forks in vivo and in vitro and unwinds lagging strands. *Nucleic acids research*, **33**(11), pp. 3678–3690.
- [20] Fujikane R., Komori K., Shinagawa H., Ishino Y., 2005. Identification of a novel helicase activity unwinding branched DNAs from the hyperthermophilic archaeon, *Pyrococcus furiosus*. *Journal of Biological Chemistry*, **280**(13), pp. 12351–12358.
- [21] Li Z., Lu S., Hou G., Ma X., Sheng D., Ni, J., Shen Y., 2008. Hjm/Hel308A DNA helicase from *Sulfolobus tokodaii* promotes replication fork regression and interacts with Hjc endonuclease in vitro. *Journal of bacteriology*, **190**(8), pp. 3006–3017.

- [22] Hong Y., Chu M., Li Y., Ni J., Sheng D., Hou G., She Q., Shen Y., 2012. Dissection of the functional domains of an archaeal Holliday junction helicase. *DNA Repair*, **11**(2), pp. 102-111.
- [23] Liew L.P., Lim Z.Y., Cohen, M., Kong, Z., Marjavaara L., Chabes A., Bell, S.D., 2016. Hydroxyurea-Mediated Cytotoxicity Without Inhibition of Ribonucleotide Reductase. *Cell reports*, **17**(6), pp. 1657–1670.
- [24] Zhai B., DuPrez K., Han X., Yuan Z., Ahmad S., Xu C., Gu L., Ni J., Fan L., Shen Y., 2018. The archaeal ATPase PINA interacts with the helicase Hjm via its carboxyl terminal KH domain remodeling and processing replication fork and Holliday junction. *Nucleic acids research*, **46**(13), pp. 6627–6641.
- [25] Foster P.G., Hickey D.A., 1999. Computational bias may affect both DNA-based and protein based phylogenetic reconstructions. *Journal of molecular evolution*, **48**(3), 284–290.
- [26] Heath T.A., Huelsenbeck J.P., Stadler T., 2014. The fossilized birth-death process for coherent calibration of divergence-time estimates. *Proceedings of the National Academy of Sciences of the United States of America*, **111**, pp. E2957-66.
- [27] Felsenstein J., 1985. Confidence limits on phylogenies: an approach using the bootstrap. *Evolution*, **39**, 783–791.
- [28] Bagowski C.P., Bruins W., Te Velthuis A.J., 2010. The nature of protein domain evolution: shaping the interaction network. *Current genomics*, **11**(5), 368–376.
- [29] Mistry J., Chuguransky S., Williams L., Qureshi M., Salazar G.A., Sonnhammer E., Tosatto S., Paladin L., Raj S., Richardson L.J., Finn R.D., Bateman A., 2021. Pfam: The protein families database in 2021. *Nucleic acids research*, **49**(D1), pp. D412–D419.
- [30] Challa S., Neelapu N.R.R., 2019. Phylogenetic Trees: Applications, Construction, and Assessment. In: Hakeem K., Shaik N., Banaganapalli B., Elango R. (eds) *Essentials of Bioinformatics*, Volume III. Springer, Cham, Switzerland.
- [31] Yokono M., Satoh S. Tanaka A., 2018. Comparative analyses of whole-genome protein sequences from multiple organisms. *Scientific Reports*, **8**, pp. 6800.
- [32] Opperdoes, F.R., 2003. Phylogenetic analysis using protein sequences. In *The Phylogenetics Handbook: A Practical Approach to DNA and Protein Phylogeny*, 1st ed. Salemi, M., Vandamme, A.-M., Eds., Cambridge University Press, Cambridge, London, United Kingdom.
- [33] Bogdanowicz D., Giaro K., 2010. Comparing arbitrary unrooted phylogenetic trees using generalized matching split distance. 2nd International Conference on Information Technology, (2010 ICIT), Gdansk, Poland, pp. 259-262.
- [34] Soltis P., Soltis, D., 2003. Applying the Bootstrap in Phylogeny Reconstruction. *Statistical Science*, **18**(2), pp. 256-267.
- [35] Varki A., Altheide T.K., 2005. Comparing the human and chimpanzee genomes: searching for needles in a haystack. *Genome research*, **15**(12), pp. 1746–1758.
- [36] Chen F.-C., Li W.-H., 2001. Genomic Divergences between Humans and Other Hominoids and the Effective Population Size of the Common Ancestor of Humans and Chimpanzees. *The American Journal of Human Genetics*, **68**(2), pp. 444-456.
- [37] Suntsova M.V., Buzdin A.A., 2020. Differences between human and chimpanzee genomes and their implications in gene expression, protein functions and biochemical properties of the two species. *BMC Genomics*, **21**, pp. 535.
- [38] Chimpanzee Sequencing and Analysis Consortium, 2005. Initial sequence of the chimpanzee genome and comparison with the human genome. *Nature*, **437**(7055), pp. 69–87.
- [39] Dorus S., Vallender E.J., Evans P.D., Anderson J.R., Gilbert S.L., Mahowald M., Wyckoff G.J., Malcom C.M., Lahn, B.T., 2004. Accelerated evolution of nervous system genes in the origin of *Homo sapiens*. *Cell*, **119**(7), pp. 1027–1040.
- [40] Evans P.D., Gilbert S.L., Mekel-Bobrov N., Vallender E.J., Anderson J.R., Vaez-Azizi L.M., Tishkoff S.A., Hudson R.R., Lahn B.T., 2005. Microcephalin, a gene regulating brain size, continues to evolve adaptively in humans. *Science (New York, N.Y.)*, **309**(5741), pp. 1717–1720.
- [41] Zhang J., Webb D.M., Podlaha O., 2002. Accelerated protein evolution and origins of human-specific features: *Foxp2* as an example. *Genetics*, **162**(4), pp. 1825–1835.
- [42] Wyckoff G.J., Wang W., Wu C.I., 2000. Rapid evolution of male reproductive genes in the descent of man. *Nature*, **403**(6767), pp. 304–309.

- [43] Go Y., Niimura Y., 2008. Similar numbers but different repertoires of olfactory receptor genes in humans and chimpanzees. *Molecular biology and evolution*, **25**(9), pp. 1897–1907.
- [44] Gallus S., Hallström B.M., Kumar V., Dodt W.G., Janke A., Schumann G.G., Nilsson, M.A., 2015. Evolutionary histories of transposable elements in the genome of the largest living marsupial carnivore, the Tasmanian devil. *Molecular biology and evolution*, **32**(5), pp. 1268–1283.
- [45] Kazazian H.H., Jr, Moran J.V., 2017. Mobile DNA in Health and Disease. *The New England journal of medicine*, **377**(4), pp. 361–370.
- [46] Wang P.J., 2017. Tracking LINE1 retrotransposition in the germline. *Proceedings of the National Academy of Sciences of the United States of America*, **114**(28), pp. 7194–7196.
- [47] Ostertag E.M., Kazazian H.H., Jr, 2001. Biology of mammalian L1 retrotransposons. *Annual review of genetics*, **35**, pp. 501–538.
- [48] Peat J.R., Ortega-Recalde O., Kardailsky O., Hore, T.A., 2017. The elephant shark methylome reveals conservation of epigenetic regulation across jawed vertebrates. *F1000Research*, **6**, pp. 526.
- [49] Evolution, 2014. Scitable by Nature Education. <https://www.nature.com/scitable/definition/evolution-78/>. Accessed January 10, 2021.
- [50] Mozhayskiy V., Tagkopoulos I., 2012. Horizontal gene transfer dynamics and distribution of fitness effects during microbial *in silico* evolution. *BMC Bioinformatics*, **13**, pp. S13.
- [51] Boto L., 2010. Horizontal gene transfer in evolution: facts and challenges. *Proceedings. Biological sciences*, **277**(1683), pp. 819–827.
- [52] Husnik F., McCutcheon J.P., 2018. Functional horizontal gene transfer from bacteria to eukaryotes. *Nature reviews. Microbiology*, **16**(2), pp. 67–79.
- [53] Naylor G.J.P., Brown W.M., 1998. Amphioxus mitochondrial DNA, chordate phylogeny, and the limits of inference based on comparisons of sequences. *Systematics Biology*, **47**, pp. 61–76.
- [54] Xiong J., 2006. Protein Motifs and Domain Prediction. In *Essential Bioinformatics* (pp. 85-94). Cambridge: Cambridge University Press. Cambridge, London, United Kingdom.
- [55] Pavlov A.R., Belova G.I., Kozyavkin S.A., Slesarev, A.I., 2002. Helix-hairpin-helix motifs confer salt resistance and processivity on chimeric DNA polymerases. *Proceedings of the National Academy of Sciences of the United States of America*, **99**(21), pp. 13510–13515.
- [56] Alberts B., Johnson A., Lewis J., Raff M., Roberts K., Walter P., 2002. *Molecular Biology of the Cell*. In *DNA-Binding Motifs in Gene Regulatory Proteins*. 4th ed. Garland Science, New York, USA.
- [57] Newman J.A., Savitsky P., Allerston C.K., Bizard A.H., Özer Ö., Sarlós K., Liu Y., Pardon E., Steyaert J., Hickson I.D., Gileadi O., 2015. Crystal structure of the Bloom's syndrome helicase indicates a role for the HRDC domain in conformational changes. *Nucleic acids research*, **43**(10), pp. 5221–5235.
- [58] Shao X., Grishin N.V., 2000. Common fold in helix-hairpin-helix proteins. *Nucleic acids research*, **28**(14), pp. 2643–2650.
- [59] Umate P., Tuteja N., Tuteja R., 2011. Genome-wide comprehensive analysis of human helicases. *Communicative & integrative biology*, **4**(1), pp. 118–137.
- [60] Yankiwski V., Noonan J.P., Neff N.F., 2001. The C-terminal domain of the Bloom syndrome DNA helicase is essential for genomic stability. *BMC cell biology*, **2**, pp. 11.
- [61] Guo R.B., Rigolet P., Zargarian L., Fermandjian S., Xi X.G., 2005. Structural and functional characterizations reveal the importance of a zinc binding domain in Bloom's syndrome helicase. *Nucleic acids research*, **33**(10), pp. 3109–3124.
- [62] Shi J., Chen W.F., Zhang B., Fan S.H., Ai X., Liu N.N., Rety S., Xi X.G., 2017. A helical bundle in the N-terminal domain of the BLM helicase mediates dimer and potentially hexamer formation. *The Journal of biological chemistry*, **292**(14), pp. 5909–5920.
- [63] Manthei K.A., Keck, J.L., 2013. The BLM dissolvosome in DNA replication and repair. *Cellular and molecular life sciences : CMLS*, **70**(21), pp. 4067–4084.



## Local Geology Effects on Soil Amplification and Predominant Period in Düzce Basin, NW Turkey

Ergin ULUTAŞ<sup>1</sup> , Özkan CORUK<sup>2</sup> , Ahmet KARAKAŞ<sup>3,\*</sup> 

<sup>1</sup> Department of Geophysical Engineering, Kocaeli University, Kocaeli, 41001, Turkey, **ORCID:** 0000-0002-3553-5051

<sup>2</sup> Department of Geological Engineering, Kocaeli University, Kocaeli, 41001, Turkey, **ORCID:** 0000-0001-5072-200X

<sup>3</sup> Department of Geological Engineering, Kocaeli University, Kocaeli, 41001, Turkey, **ORCID:** 0000-0002-4672-2063

### Article Info

#### Research paper

Received : June 15, 2021

Accepted : August 24, 2021

#### Keywords

Local Geology  
Soil Amplification  
Predominant Period  
Düzce Basin

### Abstract

Amplification and predominant periods of soils in Düzce Basin were investigated by analysing the data sets of last two major earthquakes and aftershocks of Kocaeli and Düzce earthquakes occurred in 1999 with a magnitude of  $M_w=7.4$  and  $M_w=7.2$ , respectively. Two different methods named horizontal/vertical spectral acceleration ratio (HVSAR) and soil-to-rock Response Spectral Acceleration Ratio (RSAR) were used to determine soil amplifications for various periods in Düzce Basin. The data set includes 31 strong ground motion records from five strong ground motion stations. It was found that the site amplifications at stations are directly related to the local geology underlying the stations. Averaging the residuals between the predicted and observed PGAs resulted in soil amplification from 1.33 to 2.33. The HVSAR method presented soil amplification values between 2.7 and 10 and predominant period values between 0.4 and 0.7 s. Soil amplification values from 1.5 to 14 and predominant periods from 0.5 to 0.8 s were obtained by the RSAR method. High site amplifications and predominant periods mainly depend on the thickness of lithological variances accompanied by low physical and geotechnical properties of alluvial deposits.

## 1. Introduction

Two major earthquakes struck cities located in the Düzce Basin. The first earthquake occurred on 17 August 1999 ( $M_w=7.4$ ) (Kocaeli earthquake) and the second one occurred on 12 November 1999 ( $M_w=7.2$ ) (Düzce earthquake). The epicenter of the first earthquake was located near Golcuk at a depth of 15 km [1] and the epicenter of the second earthquake was located 3.5 km southeast of Düzce at a depth of 12 km [2, 3]. 17 August 1999 ( $M_w=7.4$ ) earthquake hit the eastern Marmara Region and generated approximately 150 km of surface rupture with dextral offsets exceeding 5 m [4-6]. On 12 November 1999 ( $M_w=7.2$ ) earthquake, most of the damage occurred in southern Düzce city founded on young alluvial deposits [7] due to soil amplification and poorly constructed buildings [8].

It has been proven that ground motion during an earthquake can be amplified by local conditions [9-10]. In some cases it amplifies the seismic shake in a range of periods that coincide with the periods of vibration of the damaged structures [11]. To this extent [12], the relationship between the amplification caused by surface geology and the extent of damages on buildings can be established. Attenuation relationships for peak ground accelerations (PGAs), and the H/V (Horizontal/Vertical) Spectral Acceleration Ratio (HVSAR) and soil-to-rock Response Spectral Acceleration Ratio (RSAR) methods for strong ground motion records were commonly used to estimate the response of soil-site ground motions [13-18].

The large number of ground motion acceleration recordings after the 17 August 1999 and 12 November 1999 earthquakes provided an opportunity to study attenuation models for the Marmara Region [14], [19-22]. Although the attenuation relationships are used in regional seismic studies, they are not sufficient to explain the damage that occurs in a region after an earthquake. Therefore, site amplification studies are required taking

\* Corresponding Author: akarakas@kocaeli.edu.tr



into consideration the local geology for analyzing the damage pattern that could be created by a possible earthquake. Some previous studies investigated the site amplification and its effects in northwestern Turkey [16], [23-26]. One of the regional site effect studies defined the site amplification in the Adapazarı Basin [16].

This study investigated the amplification and predominant periods of soil deposits in Düzce Basin, located in east of the Marmara Region, based on the seismologic, geologic, and geotechnical data to evaluate the relationship between the surface and subsurface geology and damage pattern. The study used 26 strong

ground motion records of the main shocks and aftershocks of the 1999 Kocaeli and Düzce earthquakes, as well as an additional five moderate earthquakes which occurred in the year 2000 in the Marmara Region. A total of 31 strong ground motions recorded at stations located in the Düzce Basin and one station located on a rock site near the Düzce Basin, was evaluated for site amplification and predominant period of the soil deposits (Figure 1). The residuals of peak ground accelerations (PGAs), HVSAR and RSAR methods were used to determine site amplifications and predominant periods of study area stations.

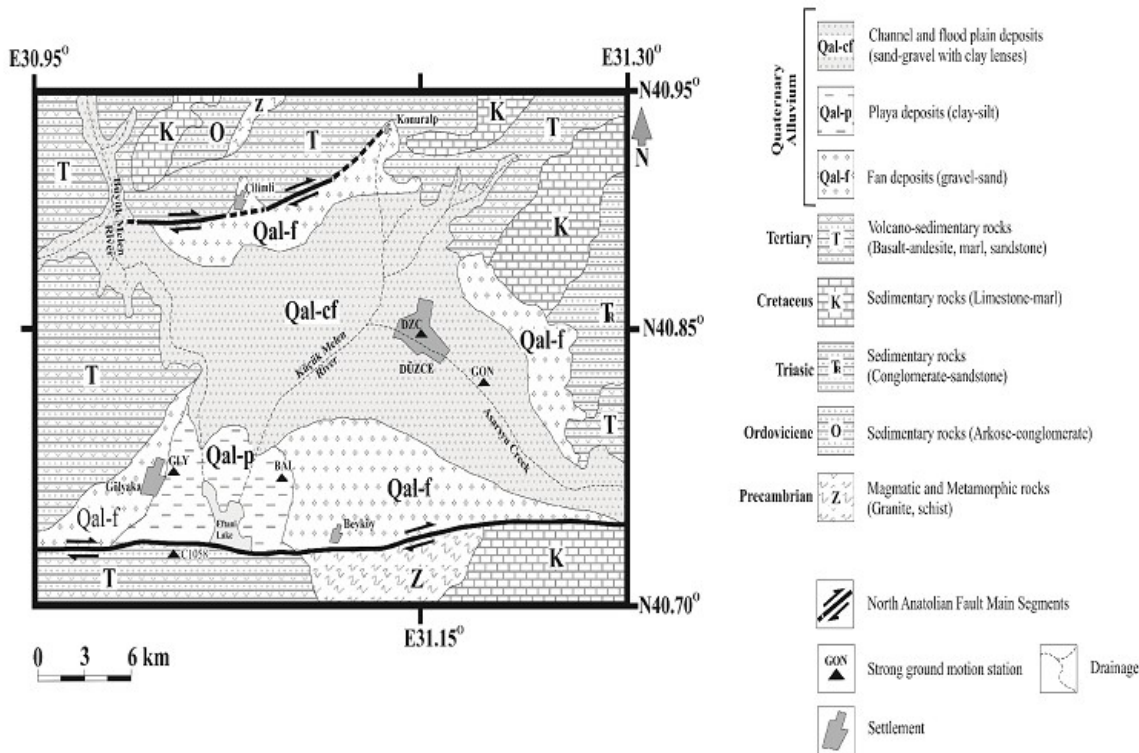


Figure 1. Geology map of the study area.

## 2. Geological Setting

The geologic setting includes the geological, geomorphological, and tectonic features of the Düzce Basin and its surroundings. Düzce Basin, as a graben-like basin, was formed by the tectonic activities of the North Anatolian Fault (NAF). The basin is bounded in the south by the active Gölyaka-Eftani-Beyköy Fault (GEBF) and in the north by the Çilimli-Konuralp Fault (ÇKF). ÇKF is relatively less active than GEBF. These faults are parts of the southern and northern segments of the NAF and are the main features that shape the morphology of the region. The slopes of the southern elevations facing the Düzce Plain are steeper than the slopes of the northern elevations. Düzce Plain, located in the central part of the basin, presents a low-inclined topography towards the southwest (towards Eftani Lake). The drainage network developed

depending on the morphology of the basin has NE-SW and E-W flows. The hydrological and morphological features in the basin are the result of intense tectonic activity that controls the basin structure and the general slope of the plain.

The basement rocks of the region consist of Precambrian magmatic and metamorphic rocks (Z) (Figure 1). Schists and granitic rocks are the basement rocks on which a thick sedimentary sequence is found. The sequence begins with Ordovician arkose and conglomerate sedimentary rocks (O). Triassic sandstone and conglomerate (TR) alternations are exposed on the Ordovician rocks in the east of the basin. Cretaceous limestone-marl alternations (K) are widely observed on Triassic rocks in the region. Tertiary volcano-sedimentary rocks (T) with flysch character were deposited on Cretaceous rocks. Volcano-sedimentary unit consisting of



interbedded basalt-andesite, marl and sandstone lithologies. The dominant lithologies in the southwestern part of the region are basalts and andesites. The youngest unit is the alluvium deposited in the basin. The thickness and lithological variation of the alluvium depend on the tectonic environment, which directly affects the morphology and basin geometry. Alluvial fan deposits (Qal-f) on the northern and southern mountain slopes, channel, and flood plain deposits (Qal-cf) and lacustrine-playa deposits (Qal-p). Alluvial fan deposits consist of gravel-sand, channel and flood plain deposits consist of clay-lensed sand-gravel and lake-playa deposits consist of clay-silt deposits.

Tectonic activities that control the morphology and geometry of the basin caused deposition of thick alluvial sediments. The bedrock topography of the plain is inclined toward the southwest, as is the surface topography. Accordingly, the alluvium thickness reaches up to between 215 m and 255 m around the city of Düzce and the northern border of Lake Eftani. While the alluvium thickness toward the west border of the basin is around 100 m, it is around 50 m toward the east and north borders of

the basin [27]. The bedrock inclination is an indication of the active tectonism in south. Therefore, there is a sudden increase in the thickness of the alluvial deposits from the south border of the basin to north of Lake Eftani.

### 3. Geology of the Station Sites

The geotechnical properties of the station sites located on the alluvial deposits of the Düzce Plain were obtained from the shallow geotechnical investigation borings. The data for the thickness and geological properties for deeper levels of the deposits were obtained from the studies of [27-28]. The geologic and geotechnical properties of the study area rocks were determined by the field observations and laboratory tests. Ref [29] standard was used to categorize the ground (soil and rock layers) of the study area stations based on the geotechnical properties. A summary of the geotechnical properties of each station is shown in Figure 2 and the detailed geologic and geotechnical properties of each station are explained below.

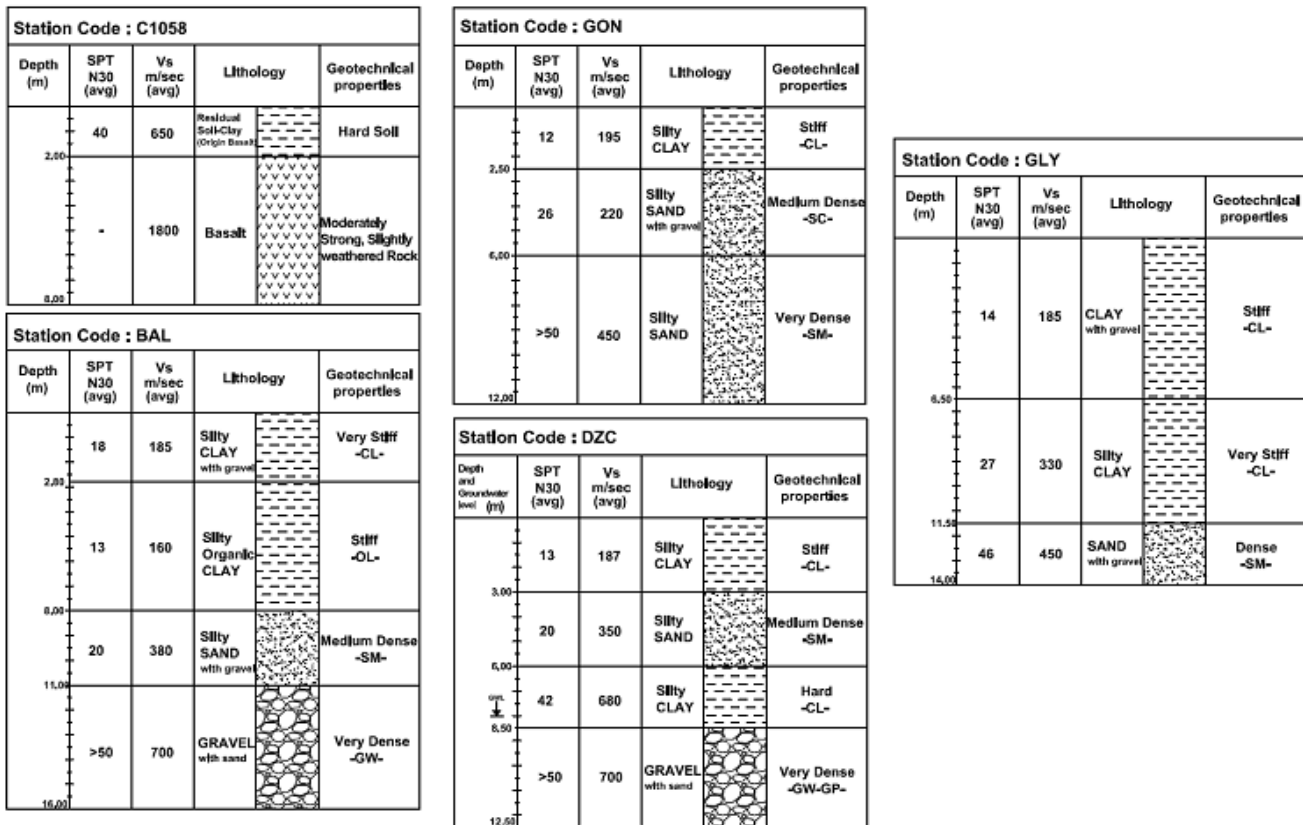


Figure 2. Summary of geotechnical properties of each station.

#### 3.1. Station 1058

This station is located on a basalt level of the Tertiary volcano-sedimentary rocks (T). It is located on a site approximately 520 m south of the GEBF. The basalt level

has a two-meter weathered zone below the surface. This zone has gained a residual soil character under the atmospheric conditions. The laboratory tests run for the samples of this zone indicated a hard soil with low plasticity. This zone has a 650 m/s average Vs (Shear Wave

Velocity) based on the geotechnical properties and falls into the “Hard Soil” category according to the [29] standard. At depths below two meters, there is a dark brown, slightly weathered, very wide spaced discontinuity and moderately strong basalt level. The recording device was located on the weathered zone and the slope of the site location is around 25 percent toward the plain.

### 3.2. Station BAL

This station is located on the lacustrine-playa deposits (Qal-p) to the north of Eftani Lake. The distance between the station and the GEBF is about four km. The thickness of the alluvial deposits is approximately 210 m in this section. According to the 16 m geotechnical boring data, the soil layers downward are very stiff silty clay with gravel (CL) (2.80 m), stiff silty organic clay (OL) (5.20 m), medium dense silty sand with gravel (SM) (3.00 m) and very dense gravel with sand (GW) (in excess of 5.00 m). The  $V_s$  values of the layers vary between 160 m/s and 700 m/s based on the seismic refraction measurements [30]. The soil layers below the station yield different geotechnical properties. Especially, the second layer (organic clay) has low geotechnical properties (consistency, unit weight, SPT- $N_{30}$  values, etc.) and  $V_s$  value.

### 3.3. Station GLY

This station is also located on the lacustrine-playa deposits (Qal-p) in the western section of Düzce Plain. The distance between the station and the GEBF is about 2.3 km. The thickness of the alluvial deposits is approximately 120 m in this section. According to the 14 m geotechnical boring data, the soil layers downward are very stiff clay with gravel (CL) (6.80 m), stiff silty clay (CL) (5.00 m) and very dense sand with gravel (SM) (in excess of 2.50 m). The  $V_s$  values of the layers vary between 185 m/s and 450 m/s based on the seismic refraction measurements [31]. The soil profile of the station site ground presents homogeneity with depth in general. The soil profile consisted of an 11.50 m clay layer and increasing geotechnical properties with depth. The organic material proportion is quite low in the clay layer. The environment of deposition should be the margin of a lake and flood plain for the clay layer. The sand with gravel layer below the 11.50 m depth should be part of the upper levels of the alluvial fan deposits (Qal-f). The geotechnical properties of the clay layer are low.

### 3.4. Station GON

This station is located on alluvial deposits (Qal-cf) in the eastern section of Düzce Plain. The distance between

the station and the GEBF Fault is about five km. The thickness of the alluvial deposits is approximately 170 m in this section. According to the 12 m geotechnical boring data, the soil layers from the surface are stiff silty clay (CL) (2.50 m), medium dense silty sand with gravel (SC) (3.50 m) and very dense silty sand (SM) (in excess of 6.00 m). The  $V_s$  values of the layers vary between 195 m/s and 450 m/s based on the seismic refraction measurements [32]. The soil profile under the station consisted mainly of fine- and coarse-grained sand layers covered by a cap clay layer. The sand layers were deposited in the channel and floodplain of the river with low energy. The geotechnical properties of homogeneous sand layers indicate a consistent increase with depth in general.

### 3.5. Station DZC

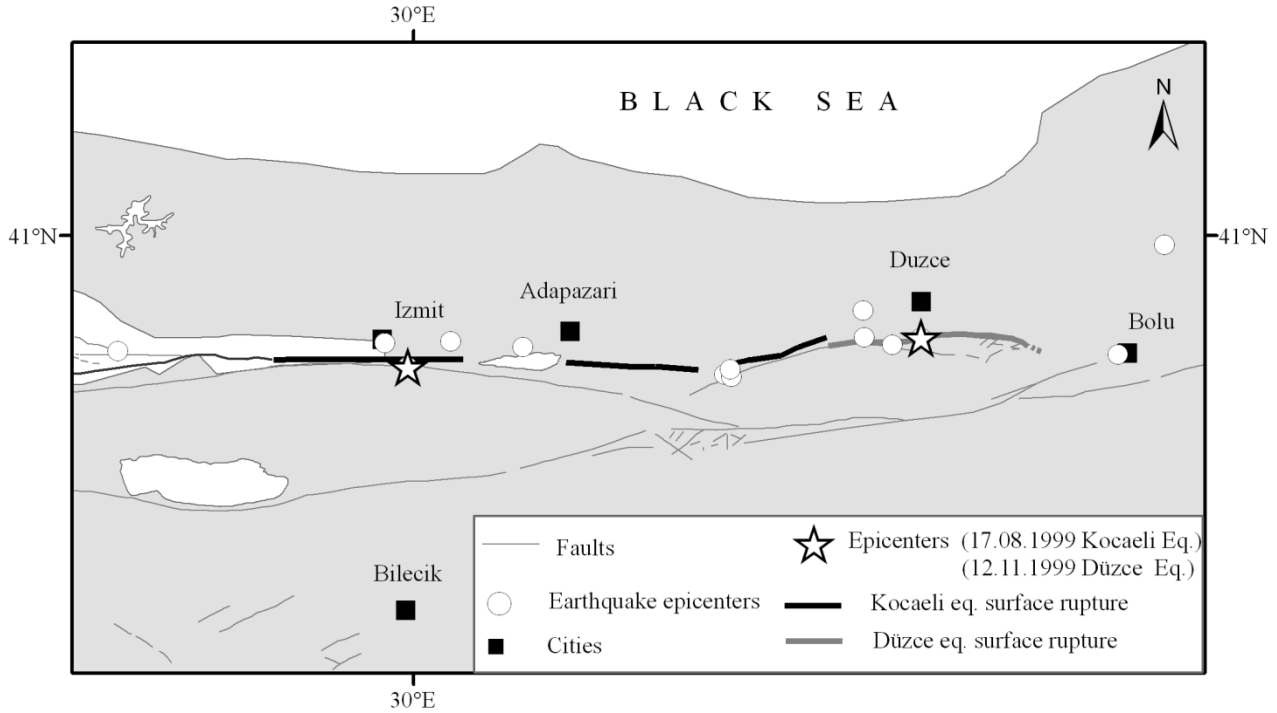
This station is also located in the central part of Düzce Plain with alluvial deposits (Qal-cf). The distance between the station and the GEBF is about 8.5 km. The thickness of the alluvial deposits is approximately 220 m in this section. According to the 12.50 m geotechnical boring data, the soil layers downward are stiff silty clay (CL) (3.00 m), medium dense silty sand (SM) (3.00 m), hard silty clay (CL) (2.50 m) and very dense gravel with sand (GW-GP) (in excess of 4.00 m). The  $V_s$  values of the layers vary between 187 m/s and 700 m/s based on the seismic refraction measurements [33]. The soil profile of the ground at the station site presents heterogeneity with depth in general, due to soil layers with different soil grains. The gravel layer at the bottom of the soil profile must be the channel deposits of the river, placed with high energy. On the other hand, the clay and sand layers should be deposited in the channel and flood plain during the energy decrease of the river.

## 4. Data Processing

The data set for this study included acceleration records of 31 strong ground motions recorded at five different stations. These strong ground motion data came from 15 different recordings of earthquakes that occurred between 1999 and 2000 (Figure 3). The strong ground motion stations were operated by three data centers (Table 1); Boğaziçi University Kandilli Observatory Earthquake Research Institute (KOERI), Ministry of Public Works and Settlement Department of Disaster Affairs Earthquake Research Department (ERD) and Columbia University Lamont Doherty Earth Observatory (LDEO). Accelerometers set up in various ground types recorded the strong ground motion data and Table 1 shows the recording types and sampling frequencies of the study area stations.

**Table 1.** Sensor type and sampling rate of the records of the study area stations.

Station Code	Lat. (°)	Long.(°)	Operator	Type of Recorders	Sampling Rate (Hz.)
BAL	40.780	31.102	KOERI	GSR-12	200
C1058	40.755	31.014	LDEO	TERRA-TEK	100
DZC	40.843	31.151	ERD	SMA-1	200
GON	40.817	31.210	KOERI	GSR-12	200
GLY	40.786	31.009	ERD	K2-ALTUS	200

**Figure 3.** Locations of 15 earthquakes used for the soil amplification of the sites.

The data set is restricted to earthquakes with  $M_w$  greater than or equal to 4.7 (Table 2). Focal depths of the earthquakes are between 6 and 22 km. The earthquake size is characterized by the moment magnitude ( $M_w$ ) as described by [34].  $M_w$  corresponds to a well-defined physical property of the source. Thus, all types of

magnitudes were converted to the moment magnitudes with an empirical equation Eq. (1) proposed by [15] for the Marmara Region:

$$M_d = 0.778M_w + 1.525 \quad (1)$$

**Table 2.** Sensor type and sampling rate of the records of the study area stations.

Event Index	Date	hr:min:sec	Lat. (°)	Long. (°)	$M_w$	Depth (km)
1	17.08.1999	00:01:39	40.75	29.86	7.4	17
2	22.08.1999	14:30:58	40.64	30.77	5.1	10
3	31.08.1999	08:10:49	40.71	29.95	4.7	10
4	13.09.1999	11:55:28	40.71	30.05	5.8	13
5	29.09.1999	00:13:05	40.74	29.35	5.0	10
6	07.11.1999	16:54:41	40.69	30.73	5.2	10
7	11.11.1999	14:41:25	40.74	30.27	6.0	22
8	12.11.1999	16:57:19	40.76	31.16	7.2	10
9	12.11.1999	17:17:56	40.78	31.12	5.6	10
10	13.11.1999	00:54:55	40.77	31.05	4.7	10
11	19.11.1999	19:59:07	40.81	30.97	5.1	6
12	16.11.1999	17:51:18	40.72	31.61	5.0	10
13	14.02.2000	06:56:34	41.02	31.76	5.1	10
14	06.06.2000	02:41:49	40.69	32.99	5.6	10
15	23.08.2000	13:41:28	40.68	30.72	5.4	15

All of the raw strong ground motion data were obtained from different databases supplied by the following organizations: European Strong-Motion Data (ISESD); the Pacific Earthquake Research Center (PEER); Consortium of Organizations for Strong Motion Observation Systems (COSMOS) and the United States Geological Survey (USGS). The raw data always contain some errors, so these errors should be corrected prior to conducting the site amplification analyses. Thus, a software application developed by [35] as “The Basic Strong-Motion Accelerogram Processing Software” was used to carry out the data corrections for all of the raw data of time-history records. Firstly, a baseline correction was applied. A Fast Fourier Transform (FFT) is calculated for all recording to ensure that the selected frequency is the dominant signal band. A more or less constant amplitude of the FFT spectrum at frequencies lower than  $f_c$  (corner frequency) or at frequencies beyond  $f_{max}$  (maximum frequency) is generally an indicator to understand low or high frequency noise, respectively [36-16]. This situation proves the necessity of band-pass filter usage to eliminate low-and high-frequency noise. Therefore, the signal parts considered to be noises and the reliable parts of the signal were filtered with a Butterworth filter of order 2. The Butterworth filter is one of the ideal filters that has a very sharp transition from passband to stopband. The filter intervals defined for all of the records are mainly in the range of 0.12-20 Hz.

## 5. Methods

Determination of soil amplification consisted of four stages: data gathering, data correction, data analysis and interpretation of the results. Raw strong ground motion data gathered in the field were corrected to be used by the amplification methods. The amplification methods were performed using the corrected data. Three different methods were used to define the soil amplifications and predominant periods in the basin. These methods are residuals of peak ground accelerations (PGAs), HVSAR and RSAR methods. The results obtained from these methods were interpreted by considering the geology of the basin and the engineering geological properties of the soils deposited in the basin. Application of each amplification method is explained below in detail.

### 5.1. Residual of Peak Ground Accelerations (PGAs)

The previous GMPEs [14-16] predicted from a number of records recorded in the NW of Turkey were selected for the purpose of a set of site amplifications and spectral shapes of the ground motions. The GMPEs were then used to predict the differences between the measured

and the observed values of strong ground motions, also known as the residual approximation of strong ground motions. For the residual calculations, the horizontal components of PGAs from the earthquake magnitudes of  $M_w \geq 4.7$  were used. The rupture distance were chosen as a surface projection of the rupture area. In order to calculate the residuals of PGAs, the empirical attenuation relationship used in this study was chosen from the coefficients of [15], who had collected a considerable amount of PGA data and derived an attenuation relationship by using basic linear regression empirical approaches [37]. The formulation of PGA for the Marmara region proposed by [15] is given in Eq. (2):

$$\log A = 0.183684 + 0.534677M_w - \log_{10}(r_{rup} + 0.0183 \times 10^{0.4537M_w}) - 0.001622r_{rup} \quad (2)$$

where A is acceleration in g and  $r_{rup}$  is source to site distance as Joyner and Boore distance [38] in km. Site effect terms were not included in the model [15]. This is because some of the stations do not have  $V_{S30}$  measurements (the average shear-wave velocity for the upper 30-m depth in m/s). The behavior of the attenuation curves (Figure 4) of the selected model curve are in good agreement with the model of [14].

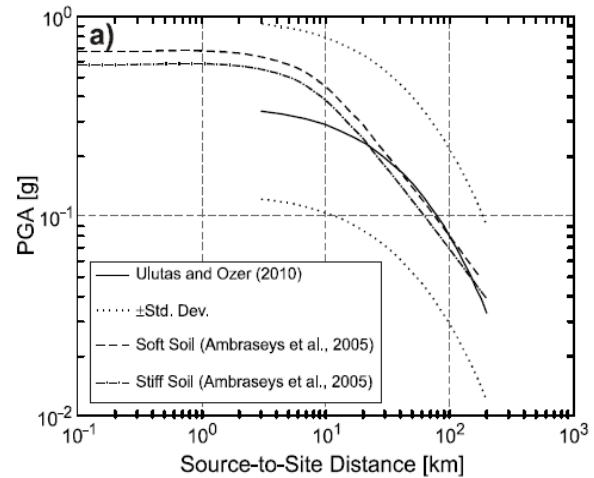


**Figure 4.** Comparison of the attenuation relationships of [14-16]

In order to assess site amplification, the records of the five stations installed in Düzce Basin were chosen. The site amplifications were determined empirically by averaging the abovementioned residuals between observed and predicted values of PGAs and SAs. Eq. (3) is the formulation for the site amplifications [38]:

$$S = \exp \left[ \frac{1}{n} \sum_{i=1}^n \ln(D_i/\bar{D}_i) \right] \quad (3)$$

where  $D_i$  the observed PGA value and  $\bar{D}_i$  is the predicted PGA value. For the peak ground motion, the observed PGA could be multiplied with the above-mentioned site amplification factor (S) as explained in Eq. (4).

$$(S \times D_i) \tag{4}$$

For comparing the results from various empirical PGA attenuation relationships, one of the most commonly used relationship was selected [14]. Table 3 presents the calculated site amplification values of the stations by using the residuals of PGA proposed by [14-15]. The amplification results of these two models are consistent with soil conditions of stations.

**Table 3.** Comparison of site amplifications

Station Code	Site Amplification for PGA <sup>1</sup>	Site Amplification for PGA <sup>2</sup>
BAL	2.22	1.63
C1058	0.31	0.24
DZC	1.33	1.33
GLY	1.5	1.68
GON	1.35	1.06

<sup>1</sup> PGA attenuation model proposed by [15]

<sup>2</sup> PGA attenuation model proposed by [14]

### 5.2. H/V (Horizontal/Vertical) Spectral Acceleration Ratio (HVSAR)

The second method used for determination of soil amplification and predominant period is the HVSAR method. The technique, originally proposed by [39] and made widely known by [40], consists of estimating the ratio between the Fourier amplitude spectra of the horizontal (H) and vertical (V) components of ground motion at a single station.

The hypothesis of this technique is that for a soft layer overlying a half space, the soft layer will amplify the horizontal component of ground motion, while amplification effects on the vertical component are small enough to be neglected [40]. Comparisons between this technique and other methods for site response estimation were described by [18], [41-43]. It has been found that the HVSAR method is consistent with the general geological conditions of the recording sites [44]. It is accepted that the results of the HVSAR method reflect the predominant period of the sediments. However, the general conclusion is that the technique fails at the amplitude level, especially for high periods [45].

The spectral ratios are calculated by taking the ratio

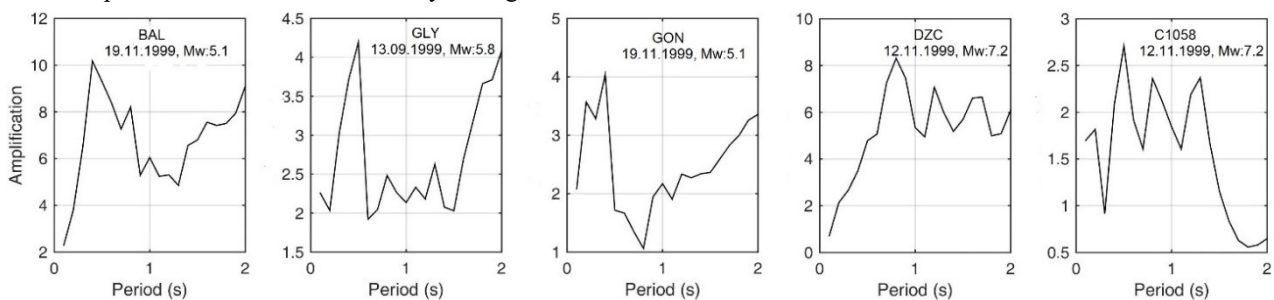


**Figure 5.** HVSARs on strong ground motion data from the various earthquakes at BAL, GLY, GON, DZC and C1058 stations.

of the Fourier amplitude spectra (FAS) or response spectra (RS) of a soil site record [40-48,18]. The RS is a very useful tool of engineering seismology and earthquake engineering for analyzing the performance of structures during an earthquake. It is an approach to estimate the effects of ground motion on buildings for the various natural periods. The natural period that affects a building is related to damping ratios defined by the structural features of buildings. The vibration created by an earthquake on a building is damped by converting it to friction and heat energy with the interaction of building elements. The degree of damping depends on the type of construction of the building in question. A damping ratio of 5% is generally accepted for the design of reinforced concrete construction [49]. The RS ratios were used for 5% critical damping from the earthquakes ( $M_w > 5.1$ ) recorded in the region. Selected events are in the moment-magnitude range  $4.7 \leq M_w \leq 7.4$  and focal depths range 6 to 22 km in this study. The horizontal component used in HVSAR method is the largest peak among the two horizontal components (EW-NS).

The RS clearly demonstrate that the horizontal components of motion have dominant peaks. These peaks are very significant in describing the damage to structures in a city. The HVSAR method facilitates the calculation of the transfer function using the relationship in Eq. (5).

$$R = (A(f)_{horizontal}) / (A(f)_{vertical}) \tag{5}$$

The HVSAR of each station is calculated by using the largest earthquakes that have occurred in the region and been recorded by the stations located in the basin. Figure 5 shows the characteristics of H/V spectral ratios versus period for the BAL, GLY, DZC, C1058, and GON stations. The amplification values of the stations ranged from 2.7 to 10. The largest amplification corresponds to a 0.4 s predominant period for the BAL station, a 0.5 s predominant period for the GLY station, a 0.7 s predominant period for the DZC station and a 0.5 s predominant period for the GON station. The C1058 station, set on the bedrock outcrop at the basin margin, yielded a smaller amplification value than other stations, as expected.

### 5.3. Soil to Rock Response Spectral Acceleration Ratio (RSAR)

This method considers a “reference” motion to a nearby rock site. The critical assumption in this method is that the surface-rock-site record is equivalent to the input motion at the base of the soil layers [50]. The records of C1058 station were chosen for the soil-to-rock spectral ratios. First, the horizontal components that have the peak acceleration values were selected for the magnitude 5.1, 5.8 and 7.2 events recorded at the BAL, DZC, GLY and GOL stations. Then, the RS values of the 5% critical damping ratios for horizontal components were determined from the selected three events which are the largest earthquakes recorded at the BAL, DZC, GLY and GOL stations. Each horizontal response spectrum of the soil site records was divided into the response spectrum of the C1058 reference station. This method is accepted to be valid if the distance between the two sites is much smaller than their epicentral distance, and therefore the differences in the records are solely due to site effects [51]. Ratios of response spectra were used rather than Fourier spectra [52] because they require less data smoothing than do Fourier spectra. The amplification values of the stations ranged from 1.5 to 14. The largest amplification corresponds to a 0.5 s predominant period for the BAL station, a 0.8 s predominant period for the GLY station, a 0.7 s predominant period for the DZC station and a 0.5 s predominant period for the GON station. Figure 6 displays the response spectral ratios of each station for the selected earthquakes.

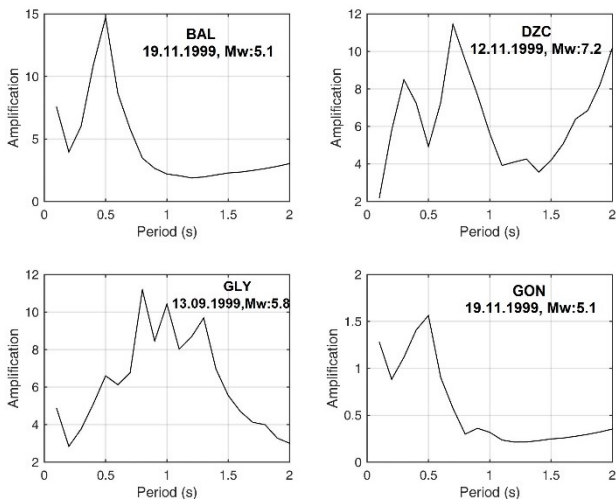


**Figure 6.** RSARs for various events with respect to the reference station of C1058.

## 6. Discussion

Site amplification and the predominant periods at

five stations located in the Düzce Basin were assessed by the GMPEs, HVSAR and RSAR methods and considering local geology. GMPEs, HVSARs and RSARs with a five percent critical damping of recorded strong ground motions give amplification on soil sites in the basin. Four stations (BAL, GLY, GON, DZC) located in the Düzce Basin and one station (C1058) located on a rock site near the Düzce Basin were evaluated for site amplification and predominant periods of the soil deposits in the basin.

The site amplification varies between 1.33 and 2.22 in GLY, BAL, DZC and GON stations according to the observed and predicted PGA residuals for those stations. As expected, de-amplification with a value of 0.31 was calculated at station C1058, which was installed on rock. The amplification values obtained from the residuals are usually valid for the soils with predominant periods shorter than 3 seconds. Additionally, PGA is not generally a good measure for earthquake risk assessment of medium and high-rise structures (>2 stories) [17]. For this purpose, the HVSAR and RSAR methods were used to determine the soil response related to the soil's predominant frequencies in earthquakes.

The results of the HVSARs were obtained by using the data for moderate and large magnitude earthquakes which have occurred in the Marmara Region. The seismic record of the 19 November 1999 earthquake ( $M_w=5.1$ ) for the BAL and GON stations, the seismic record of 11 December 1999 earthquake main shock ( $M_w=7.2$ ) for the DZC station and the seismic record of 13 September 2011 earthquake ( $M_w=5.8$ ) for the GLY station were used in the HVSAR method.

Although the C1058 station yielded a de-amplification according to the results of calculated residuals from observed and predicted acceleration values, it showed an amplification value of 2.5 at a 0.5 s period in the HVSAR method. However, this amplification value of 2.5 is lesser than the amplification values of the other stations, obtained from the HVSAR and RSAR methods. As expected, periods and amplifications revealed by the HVSAR and RSAR methods for the C1058 station located on rock are lower than those located on alluvium deposits. The two-meter weathered zone of the C1058 station site probably caused the amplification value of 2.5 in the HVSAR method.

The critical assumption in the reference site amplification studies is to define the amplification by selecting the optimum rock site motion. Although this assumption is the best possible approximation revealing the site amplification effects on the ground, the selection of the most suitable reference site is difficult in practice, because a reference rock site can have a site response of

its own. The amplification values observed at the consecutive periods for the C1058 station suggest that this station reflected its own site response. The reference site was selected according to the geotechnical data and geologic information that was available for the study area. The differences in the amplification results of the stations with the same site classes depend on the rock-soil seismic impedance difference, depth to bedrock, layer thicknesses, lithology variance and geotechnical properties of the soils.

## 7. Conclusions

It could be concluded from the study that the empirical models using the residuals can provide only a general estimation of the actual amplification of the sites. The residuals obtained from this study are the results of PGAs and do not reflect the dominant frequencies of the soils. The amplification results of the study for soft soils and rock at the site are important to predict the site response of sedimentary deposits if similar earthquakes occur in the near future. Although the results obtained from these methods indicate a general approximation, effects of the seismic impedance between the bedrock and soil layers should be considered in amplification studies. It is possible that the seismic impedance could affect peak amplifications spread in a broader band for the DZC and GLY stations.

The residual method allowed classification of the different soil types based on the amplification results. Also, the HVSAR and RSAR methods allowed determination of the predominant periods of the soil deposits in the basin. Determination of predominant periods is a necessary step to differentiate the fundamental period of engineering structures and the dominant period of soils. It is concluded that the average predominant periods of the stations are between 0.4 and 0.8 s. Moderately to severely damaged or collapsed 5-6 story buildings [53], in Düzce Earthquake, indeed support these predominant frequencies.

## Declaration of Ethical Standards

The authors of this article declare that the materials and methods used in this study do not require ethical committee permission and/or legal-special permission.

## Conflict of Interest

The authors declare that they have no known competing financial interests or personal relationships that could have appeared to influence the work reported in this paper.

## References

- [1] Polat O., Eyidoğan H., Haessler H., Cisternas H., Philip H., 2002. Analysis and interpretation of the aftershock sequence of the August 17, 1999, İzmit (Turkey) earthquake. *Journal Seismology*, **6**(3), pp. 287-306.
- [2] Bouin M.P., Bouchon M., Karabulut H., Aktar M., 2004. Rupture process of the 1999 November 12 Düzce (Turkey) earthquake deduced from strong motion and Global Positioning System measurements. *Geophysical Journal International*, **159**, pp. 207-211.
- [3] Taymaz T., 1999. Seismotectonics of the Marmara region: Source characteristics of 1999 Golcuk-Sapanca-Duzce earthquakes. *Proceedings of the International Symposium on the Kocaeli Earthquake*. Istanbul, Turkey, 2-5 December, pp. 55-78.
- [4] Pucci S., Martini P.M., Pantosti D., 2008. Preliminary slip rate estimates for the Düzce segment of the North Anatolian Fault Zone from offset geomorphic markers. *Geomorphology*, **97**, pp. 538-554.
- [5] Pucci S., Martini, P. M., Pantosti, D. 2008. Preliminary slip rate estimates for the Düzce segment of the North Anatolian Fault Zone from offset geomorphic markers. *Geomorphology*, **97**, pp. 538-554.
- [6] Utkucu M., Nalban S.S., McCloskey J., Steacy S., Alptekin Ö., 2003 Slip distribution and stress changed associated with the 1999 November 12, Düzce (Turkey), *Geophysical Journal International*, **153**(1), pp. 229-241.
- [7] Rathje E. M., Stewart J. P., Baturay M. B., Bray J. D., Bardet J. P., 2006. Strong ground motions and damage patterns from the 1999 Düzce earthquake in Turkey. *Journal Earthquake Engineering*, **10**(5), pp. 693-724.
- [8] Özmen B., 2000 12 Kasım 1999 Düzce Depreminin Konut ve İşyeri Hasarları (Rakamsal Verilerle), Bayındırlık ve İskan Bakanlığı, Afet İşleri Genel Müdürlüğü, Deprem Araştırma Dairesi, Ankara, pp. 155-214.
- [9] Aki K., 1993. Local site effects on weak and strong ground motion. *Tectonophysics*, **218**, pp. 93-111.
- [10] Bard P., 1999. Microtremor measurements: A tool for site effect estimation. *Proceedings of the Second International Symposium on the Effects of Surface Geology on Seismic Motion*. Yokohama, Japan, **3**, pp. 1251-1279.

- [11] Seo K., 1994. On the applicability of microtremors to engineering purpose, Preliminary report of the Joint ESG Research on Microtremors after the 1993 Kushiro-Oki (Hokkaido, Japan) earthquake. Proceedings of 10th European Conference on Earthquake, 4, pp. 2643-2648.
- [12] Navarro M., Enomoto T., Sánchez F. J., Matsuda I., Iwatate T., Posadas A., Luzón F., Vidal F., Seo K., 2001. Surface soil effects study using short-period microtremor observations in Almeria City, Southern Spain. Pure Applied Geophysics, 158, pp. 2481-2497.
- [13] Rosenblueth E., Archiniega A., 1992. Response spectral ratios. Earthquake Engineering Structural Dynamics, 21, pp. 483-492.
- [14] Ambraseys N. N., Douglas J., Sarma S. K., Smith P. M., 2005. Equations for the estimation of strong ground motions from shallow crustal earthquakes using data from Europe and the Middle East: horizontal peak ground acceleration and spectral acceleration. Bulletin Earthquake Engineering, 3, pp. 1-53.
- [15] Ulutaş E., Özer, M. F., 2010. Empirical attenuation relationship of peak ground acceleration for Eastern Marmara region in Turkey. Arabian Journal Science Engineering, 35, pp. 187-203.
- [16] Ulutaş E., Coruk, Ö., Karakaş A., 2011. A study of residuals for strong ground motions in Adapazarı basin, NW Turkey, by Ground Motion Prediction Equations (GMPEs). Studia Geophysica Geodaetica, 55, pp. 213-240
- [17] Douglas J., 2003. Earthquake ground motion estimation using strong motion records: A review of equations for the estimation of peak ground acceleration and response spectral ordinates. Earth-Science Reviews, 61, pp. 43-104.
- [18] Field E. H., Jacob K. H., 1995. A comparison and test of various site-response estimation techniques including three that are not reference-site dependent. *Bulletin Seismology Society America*, 85: pp. 1127-1143.
- [19] Gülkan P., Kalkan, E., 2002. Attenuation modeling of recent earthquakes in Turkey. Journal Seismology, 6, pp. 397-409.
- [20] Ozbey C., Sarı, A., Manuel, L., Erdik, M., Fahjan, Y., 2004. An empirical attenuation relationship for northwestern Turkey ground motion using a random effects approach. Soil Dynamics Earthquake Engineering, 24, pp. 115-125.
- [21] Ulusay R., Tuncay E., Sonmez H., Gokceoglu C., 2004. An attenuation relationship based on Turkish strong motion data and iso-acceleration map of Turkey. Engineering Geology, 74, pp. 265-291.
- [22] Gulkan P., Kalkan E., 2005. Discussion of the paper: An empirical attenuation relationship for northwestern Turkey ground motion using a random effects approach. Soil Dynamics Earthquake Engineering, 25, pp. 889-891.
- [23] Bakır S., Sucuoğlu H., Yılmaz T., 2002. An overview of local site effects and the associated building damage in Adapazarı during the 17 August 1999 İzmit Earthquake. Bulletin Seismology Society America, 92, pp. 509-526.
- [24] Şafak E., Erdik, M., 2000. Recorded main shock and aftershock motions. Earthquake Spectra, 16, pp. 97-112.
- [25] Özel O., Sasatani T., 2004. A site effect study of the Adapazarı basin, Turkey, from strong-and weak motion data, Journal Seismology, 8, pp. 559-572.
- [26] Özel N., Sasatani, T., Özel, O., 2004. A study of strong ground motions during the largest aftershock ( $M_w = 5.8$ ) of the 1999 Kocaeli Turkey Earthquake. Tectonophysics, 391, pp. 347-335.
- [27] Şimşek O., 1994. Consolidation properties of clays at Düzce Plain and their relationship with geological evolution. Unpublished Ph.D. Thesis, Department of Geology, İstanbul University, 88.
- [28] Şimşek O., Dalgıç S., 1997. Consolidation properties of clays at Düzce Plain and their relationship with geological evolution. Geological Bulletin of Turkey, 40(2), pp. 29-38.
- [29] BS 5930., 1999, Code of Practice for Site Investigations: British Standards Institution, London, 207.
- [30] Özyapıcı Mühendislik Ltd. Şti., 2008. Konaklı Balıca Köyü Geoteknik Araştırma Raporu, 38 p.
- [31] Akbulut Mühendislik ve Müşavirlik Ltd. Şti., 2008. Gölyaka-İmamlar Mahallesi Geoteknik Araştırma Raporu, 47p.
- [32] Özyapıcı Mühendislik Ltd. Şti., 2011. Düzce-Kaynaşlı D100 Otoyolu Geoteknik Araştırma Raporu, 128 p.
- [33] Özyapıcı Mühendislik Ltd. Şti., 2010. Düzce Uzunmustafa Mahallesi Geoteknik Araştırma Raporu, 47 p.



- [34] Hanks T.C., Kanamori H., 1979. A moment magnitude scale. *Journal Geophysical Research*, 84, pp. 2348-2350.
- [35] Converse A., Brady, A.G., 1992. *Basic Strong-Motion Accelerogram Processing Software, Version 1.0*: United States Department of the Interior, Geological Survey Open-File Report 92-296A, Washington, D.C.
- [36] Zare M., Bard, P. Y., 2002. Strong motion dataset of Turkey: Data processing and site classification. *Soil Dynamics Earthquake Engineering*, 22, pp. 703-718.
- [37] Joyner W.B. Boore D.M., 1981. Peak horizontal acceleration and velocity from strong-motion records including records from the 1979 Imperial Valley, California earthquake. *Bulletin Seismology Society America*, 71, pp. 2011-2038.
- [38] Wu Y.M., Shin T.C., Chang C.H., 2001. Near real-time mapping of peak ground acceleration and peak ground velocity following a strong earthquake. *Bulletin Seismology Society America*, 91, pp. 1218-1228.
- [39] Nogoshi M., Igarashi, T., 1971. On the amplitude characteristics of microtremor (Part 2). *Journal Seismological Society Japan*, 24, 26-40 (in Japanese with English abstract).
- [40] Nakamura Y., 1989. A method for dynamic characteristics estimation of subsurface using microtremor on the ground surface. *Quarterly Report Railway Technical Research Institute*, 30(1), pp. 25-30.
- [41] Bonila L.F., Steidl J.H., Lindley G.T., Tumarkin A. G., Archuleta R.J., 1997. Site amplification in the San Fernando Valley, California: Variability of site-effect estimation using the S-wave, coda and H/V methods, *Bulletin Seismology Society America*, 87, pp. 710-730.
- [42] Huang H.C., Teng, T.L., 1999. An evaluation on H/V ratio vs. spectral ratio for site-response estimation using the 1994 Northridge earthquake sequences. *Pure Applied Geophysics*, 156, pp. 631-49.
- [43] Riepl J., Bard P.Y., Hatzfeld D., Papaioannou C., Nechtschein S., 1998. Detailed evaluation of site-response estimation methods across and along the sedimentary valley of Volvi (EURO-SEISTEST). *Bulletin Seismology Society America*, 88, pp. 448-502.
- [44] Gosar A., 2010. Site effects and soil-structure resonance study in the Kobarid basin (NW Slovenia) using microtremors. *Natural Hazards Earth System Science*, 10, 761-772.
- [45] Sokolov VYu., Loh C.H., Jeanc W.Y., 2007. Application of horizontal-to-vertical (H/V) Fourier spectral ratio for analysis of site effect on rock (NEHRP-class B) sites in Taiwan. *Soil Dynamics Earthquake Engineering*, 27, pp. 314-323.
- [46] Berilgen M.M., 2007. Evaluation of local site effects on earthquake damages of Fatih Mosque: *Engineering Geology*, 91, pp. 240-253
- [47] Fah D., Kind F., Giardini D., 2001. Theoretical investigation of average H/V ratios. *Geophysical Journal International*, 145, pp. 535-549.
- [48] Zhao J.X., Zhang J., 2010. Side-effect of using response spectral amplification ratios for soft soil sites-earthquake source-type dependent amplification ratios. *Soil Dynamics Earthquake Engineering*, 30, pp. 258-269.
- [49] DBYBHY, Deprem Bölgelerinde Yapılacak Binalar Hakkında Yönetmelik, 2007. Resmi Gazete, Yayın Tarihi: 06.03.2007.
- [50] Steidl, J. H., Tumarkin, A. G., and Archuleta, R. J., 1996. What is a reference site? *Bulletin Seismology Society America*, 86, pp. 1733-1748.
- [51] Safak E., 2001. Local site effects and dynamic soil behavior. *Soil Dynamics Earthquake Engineering*, 21, pp. 453-458.
- [52] Yamazaki F., Ansary, M.A., 1997. Horizontal-to-vertical spectrum ratio of earthquake ground motion for site characterization: *Earthquake Engineering Structural Dynamics*, 26, pp. 671-689.
- [53] Dönmez C., Pujol, S., 2005. Spatial Distribution of Damage Caused by the 1999 Earthquakes in Turkey. *Earthquake Spectra*, 21, pp. 53-69



## Tribological Behavior of Ultra-High Molecular Weight Polyethylene Polymer with Artificial Neural Network Modeling

Kemal ERMİŞ<sup>1,\*</sup> , Hüseyin ÜNAL<sup>2</sup> 

<sup>1</sup> Department of Mechanical Engineering, Sakarya University of Applied Sciences, Sakarya, 54187, Turkey, **ORCID:** 0000-0003-3110-2731

<sup>2</sup> Department of Metallurgical and Materials Engineering, Sakarya University of Applied Sciences, Sakarya, 54187, Turkey, **ORCID:** 0000-0003-0521-6647

### Article Info

#### Research paper

Received : July 02, 2021

Accepted : September 22, 2021

#### Keywords

ANN modeling  
Medical grade UHMW-PE  
Tribology  
Wear

### Abstract

This study presents the tribological properties, wear and friction, of ultra-high molecular weight polyethylene under conditions of dry sliding and Hank's balanced salt solution lubrication. A pin-on-stainless steel disc apparatus was used for the friction and wear tests. Applied load conditions were 38, 50, 88, 100, 138, and 150N. Sliding speed conditions were 0.4, 0.5, 0.8, 1.0, 1.2 and 1.5 m/s. The results show that the coefficient of friction and the wear rate values decrease with the increase of applied load. The coefficient of friction and the wear rate values were highest under the dry sliding condition for the ranges of the sliding speed values and the applied loads tested in the study. In addition, the applicability of artificial neural networks (ANN) for predicting both the coefficients of friction and wear rate values of the material in different sliding conditions was studied. The neural network results were in agreement with the experimental results for the wear rates and coefficients of friction.

### 1. Introduction

Ultra-high molecular weight polyethylene (UHMW-PE) polymer is used regularly in the orthopedics industry due to its superior wear and friction properties. It has many properties that allow for quality performance, like a lower friction coefficient value, higher wear resistance, chemical stability, and biocompatibility, and high impact strength [1–3] Because of these properties, UHMW-PE polymer is used in the industrial sector as well as in orthopedics. As the human body is highly sensitive, the properties of any biomaterials used in the various parts of the human body should be such that they do not disturb the various functions of the human body. One material with the properties needed to be used in the human body is UHMW-PE. The UHMW-PE polymer is used in orthopedic applications involving the knee, hip, elbow, and wrist in the human body. Generally, knee operations involving prosthesis technology are performed when the

patient's joints have deteriorated. The prosthesis geometries and the types of forces acting on it determine the contacted area in the prosthetic component, the size of the contact stresses, and working conditions [4].

A good understanding of the factors affecting prosthesis use is important to reduce patients' pain and to extend the life of the joint replacement components.

The use of artificial neural networks (ANN) has been increasing in many applications to develop better and more reasonable solutions [5]. Therefore, an ANN can be used as an effective method for the prediction of the tribological behavior of medical-grade polymers. In the literature, there are a few ANN investigations on the tribological properties of polymer materials. Zamyad et al. [6] presented a hybrid model of recurrent neural networks for predicting ionic polymer-metal composite (IMPC) bending behaviors and found that their model has acceptable accuracy and flexibility when compared to the experimental data. Kurt and Oduncu [7] presented an ANN model, which was used to compare the volume loss values of UHMW-PE based composite materials. Their study has shown good

\* Corresponding Author: [ermis@subu.edu.tr](mailto:ermis@subu.edu.tr)



consistency between their model and experimental results. Velten et al. [8] studied the prediction of the wear volume of fiber-reinforced polymeric bearing materials by an ANN prediction model. They used an ANN structure that has two inputs and one output; mechanical properties and test conditions being the inputs, and wear volume being the output. Abdelbary et al. [9] studied the wear mathematical model of a polyamide 66 polymer using an ANN. They optimized their model using the ANN's prediction of test results. They found good accuracy results when comparing the simulation results to the experimental test data. Rajesh et al. [10] provided an ANN model of surface roughness during the machining of Multiwall Carbon Nanotube (MWCNT) nanocomposites, demonstrating that an ANN is a dependable tool for predicting and simulating machining response. Sabouhi et al. [11] proposed a method that uses an artificial intelligence model in combination with generic expression programming to evaluate the mechanical and physical behaviors of carbon/polymer nanotube composites. They showed that their model was used to predict satisfactory results for the elastic modulus values of the polymer-carbon nanotube composites in their studied ranges. Zhang et al. [12] predicted the coefficient of friction and the wear rates for polyamide 4.6 (PA 4.6) composites with reinforced glass fiber on a measured database using a feed-forward artificial neural network (ANN) model. According to their results, the predicted values had acceptable accuracy when compared to experimental test values. Khan et al. [13] used an ANN to model the mechanical behavior of cross-ply laminated fiber-reinforced polymer composites (FRPCs), demonstrating that an ANN is a reliable tool for predicting composite mechanical behavior. The study by Lada and Friedrich [14] predicted the wear performance and friction properties of polymer composites based on their obtained data, collected from 124 independent the pin-on-disc (POD) wear tests of polyphenylene sulfide (PPS) composites, by using artificial neural networks (ANNs) and they found their ANN model profiles were consistent with their experimental data for the characteristic tribological properties. Kazi et al. [15] employed an integrated ANN to reduce the time and effort of material characterization for large numbers of samples during the design of fiber-reinforced polymeric composites. Pajchrowski et al. [16] applied an ANN taught by reinforcement learning on an adaptive controller design for electric drive. ANN studies can be used on the tribological performance of polymer materials which have limited studies in the literature.

In this study, an artificial neural network that uses a back-propagation with feed-forward structure was used as the numerical analysis method except for when conducting traditional linear and non-linear analysis in polymer

materials. This study will provide a new approach in the field of tribology, especially with regard to medical applications. This study investigated the tribological properties of medical-grade UHMW-PE polymer in different working conditions, namely dry sliding and Hank's balanced salt solution conditions. Tribological experiments were performed at 38, 50, 88, 100, 138 and 150N of applied load and 0.4, 0.5, 0.8, 1.0, 1.2 and 1.5 m/s of sliding speed. The coefficient of friction values and specific wear rate on the UHMW-PE material under these conditions were determined. The data from the ANN analysis was compared to the experimental data. At the end of the study, the results of the ANN analysis were consistent with the experimental data. In addition, the ANN analysis showed more accurate predictions of the experimental data than linear regression. Generally, the ANN prediction of real values is more accurate than classic linear and non-linear assumptions.

## 2. Experimental Study

### 2.1. Materials

In this study, a UHMW-PE polymer, classified as medical-grade for surgical implants according to ISO 5834 and ASTM F 648 compressed molded low calcium CHIRULEN 1020 (Quadrant PHS, Germany), was used as the base polymer material. The UHMW-PE polymer was also used as the material for the cylindrical pins, each with a 3 mm radius and a length of 50 mm. The counter-face material was used AISI 304L stainless steel which was machined to a radius of 5 cm and thickness of 0.5 cm. The Vickers hardness of the counter-face disc material had an average HV 297.

Before testing, each stainless-steel disc was cleaned with acetone. Table 1 lists the test parameters for the medical-grade UHMW-PE polymer material.

**Table 1.** Test parameters of medical-grade UHMW-PE polymer material.

Ambient temperature, °C	21±2
Applied load, N	38, 50, 88, 100, 138, 150
Sliding speed, m/s	0.4, 0.5, 0.8, 1, 1.2, 1.5
Dropping velocity of water	20 drops/min
Humidity, RH	58±2%

### 2.2. The Tribometer and Tests

To test the sliding wear of the medical-grade UHMW-PE polymer, POD was performed using a wear test machine. The  $\mu$  value (coefficient of friction) of the UHMW-PE polymer was calculated from the POD machine by using Eq. (1). The normalized wear volume

divided by the sliding distance and the applied load is usually how the specific wear rate is determined. Eq. (2) was used to evaluate estimates of the specific wear rate,  $W_{sp}$ , of UHMW-PE polymer samples.

$$\mu = \frac{F_s}{F_n} \tag{1}$$

$$W_{sp} = \frac{V_{sp}}{F_n L} \tag{2}$$

where;  $F_n$  is applied load,  $F_s$  is frictional force on the polymer pin material,  $L$  is the sliding distance,  $V_{sp}$  (mass/density) is volume loss.

The mass and volume losses were obtained from each experimental measurement for different conditions and all samples.

The worn particles were removed from the polymer samples by the completion of 2 km of sliding distance corresponding to the number of turns before and after each run. In addition, stainless steel surfaces were polished to obtain a surface roughness of 0.25  $\mu\text{m}$  by corundum paper for the friction tests. Before the steel discs and the flat-ended polymer pins were installed in the pin-on-disc wear test apparatus, they were cleaned using alcohol and acetone. For both the dry sliding and HBSS (Hank's balanced salt solution) conditions, the coefficient of friction and wear rate tests were performed at sliding speeds ranging between 0.4 to 1.5 m/s and applied loads ranging between 38N to 188N at a temperature of atmospheric ambient. A schematic drawing of the experimental apparatus for the wear test is given in Figure 1.

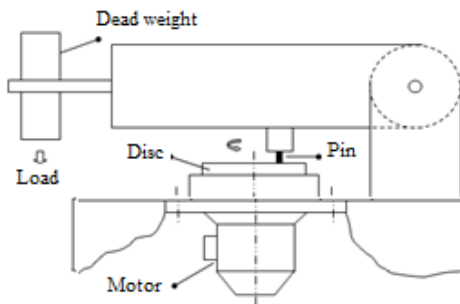


**Figure 1.** A schematic drawing of the experimental apparatus for the wear test.

The wear test apparatus included a pin sample holder and a variable speed, the variable-speed motor delivers unidirectional motion to the turntable, and thus to the disk sample. To apply forces to the sample in the pin-on-disc, the pin sample was rigidly coupled to a pivoted loading arm, which was supported by bearing arrangements. The force of friction was measured using a transducer installed on the loading arm. During the test period, data was collected every second. A microprocessor-controlled data

collecting device was employed in this study to record friction force data at a rate of 35 times per minute on average. The mass loss was measured by weighting the pin with a precision scale, with an accuracy of  $\pm 0.0001$  g. The obtained mass was converted into a volume using the density of the sample. Mass loss measurements were used to calculate the specific wear values. Sliding wear data was the average of more than three runs.

### 3. Artificial Neural Network (ANN) Modelling

A well-trained ANN can be used to create an optimal material design for certain tribological applications. For tool wear estimation on dry hard turning processes of AISI4140 steel, Rajeev et al. [17] used an ANN model with a feed-forward neural network design. Ufnalski and Grzesiak [18] found that special measures should be taken to properly evaluate the performance of the controller because of the nature of the artificial neural network training process. Generally, the back-propagation algorithm is used for the multi-layered, feed-forward network training of models. Ermis [19, 20] developed a new algorithm for training. An ANN model was developed in this study to predict tribological data, the coefficient of friction, and the specific wear rate. The learning and training processes were carried out using an ANN model having a back-propagation and feed-forward configuration. The computer code, developed using C++ programming, was used to solve the ANN model algorithm. This algorithm formulation is shown below:

The training data sets were normalized between 0.1 and 0.9 to use the procedure. All the connection values of the weights were adjusted to threshold values and small random to obtain a training model and network outputs.

The net input for the  $j$ th node was calculated on the hidden layer,

$$\text{Net}_j = \sum_{i=1}^n W_{ij} X_i - \theta_j \tag{3}$$

where;  $W_{ij}$  is the weight's connection value from the  $i$ th node to the  $j$ th node,  $j$  is the hidden layer node,  $i$  is the input layer node and  $x$  is the input.  $\theta_j$  is the threshold between the input and the hidden layer.

Various activation functions are used to develop networks, the usage of which depends on a variety of factors, including how quickly the function changes when the function's argument changes, the interval where the functions are well behaved, or simply personal preferences. Sigmoid is one of the most commonly used activation functions. The activation function of the logistic sigmoid is used in this network structure.

The output was calculated for the  $j^{\text{th}}$  node at the hidden layer:

$$H_j = f_h \left( \sum_{i=1}^n W_{ij} X_i - \theta_j \right) \quad \text{where} \quad f_h(x) = \frac{1}{1 + e^{-\lambda_h x}} \quad (4)$$

where;  $H_j$  represents the hidden layer's neuron vector.  $f_h$  the logistic sigmoid's activation function from the input layer to the hidden layer.  $\lambda_h$  is a factor that is managing the gradient of the sigmoid function in the hidden layer.

At the hidden layer, the net input for the  $k^{\text{th}}$  node was calculated:

$$\text{Net}_k = \sum_j W_{kj} X_j - \theta_k \quad (5)$$

where;  $W_{kj}$  is the weight connection value from the  $j^{\text{th}}$  node to the  $k^{\text{th}}$  node, and  $k$  is the output layer. The threshold between the hidden and output layers is  $\theta_k$ .

At the output layer, the output was calculated for the  $k^{\text{th}}$  node:

$$Y_k = f_k \left( \sum_{j=1}^n W_{kj} X_j - \theta_k \right) \quad \text{where} \quad f_k(x) = \frac{1}{1 + e^{-\lambda_k x}} \quad (6)$$

where;  $Y_k$  is the output of the output layer neurons. The logistic sigmoid's activation function from the hidden layer to the output layer is  $f_k(x)$ .  $\lambda_k$  is a variable that controls the sigmoid function's gradient in the output layer.

Between the experimental output and the target, the output layer error was computed.

$$\delta_k = -(D_k - Y_k) f'_k \quad \text{where} \quad f'_k = Y_k (1 - Y_k) \quad (7)$$

where;  $D_k$  is the target activation of the output layer.  $\delta_k$  is the vector of errors for each output neuron, and it only depends on the faults in the output layer between the target activation and the output.  $f'_k$  is the node activation function's local slope in the output nodes.

The error in the hidden layer was calculated as follows:

$$\delta_j = f'_h \sum_{k=1}^n W_{kj} \delta_k \quad \text{where} \quad f'_h = H_j (1 - H_j) \quad (8)$$

where;  $\delta_j$  is the vector of errors for each neuron in the hidden layer,  $H_j$  is the hidden layer's neuron vector, and  $\delta_k$  is the weighted sum of all nodes. In the hidden nodes,  $f'_h$  is the local slope of the node activation function.

In the output layer, the weights and thresholds were adjusted:

$$W_{kj}^{(t+1)} = W_{kj}^{(t)} + \alpha \delta_k H_j + \eta (W_{kj}^{(t)} - W_{kj}^{(t-1)}) \quad (9)$$

$$\theta_k^{(t+1)} = \theta_k^{(t)} + \alpha \delta_k \quad \text{and} \quad \theta_j^{(t+1)} = \theta_j^{(t)} \alpha \delta_j \quad (10)$$

Where  $\alpha$  is the learning rate,  $t$  is time, and  $\eta$  is the momentum factor.

For each neuron and pattern, all calculation steps were repeated until the output layer error was within the required tolerance. The learning rate and the momentum factor were utilized to allow the prior weight change to affect the weight change in this phase.

The neural network has back-propagation, feedforward, and a three-layer configuration for use in friction coefficient and specific wear rate estimation, as shown in Figure 2.

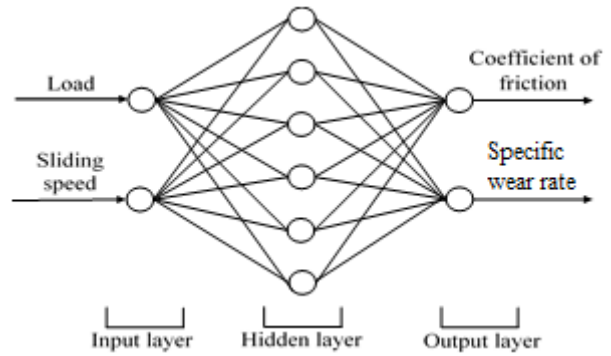


**Figure 2.** A three-layer feed-forward back-propagation neural network for the coefficient of friction and specific wear rate.

In the network structure, two input parameters applied loads and sliding speeds, and two output parameters, coefficients of friction and wear rate values, were used. To reduce the error between current data and output values, the weights, biases, and hidden node numbers were examined. The ANN configurations were set by selecting the hidden layer's numbers, nodes, the momentum coefficient, and the learning rate values to achieve the least error convergence. 18 data sets were evaluated for the cases. All data were separated into two groups. The first group has two sets of data randomly selected from the HBSS and dry sliding conditions to test. One of them was used for network training (67% of all cases) and the other set was used to test the validation of the ANN model. The layered structure of the ANN model for the specific wear rate and the coefficient of frictions are shown in Figure 3.

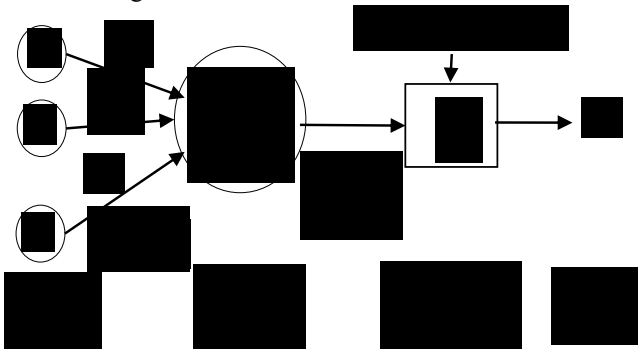


**Figure 3.** The ANN model's layered structure for the specific wear rate and the coefficient of friction.

The ANN model was utilized by using the two inputs, two outputs, and nine hidden layers. The learning ratios and the momentum coefficients setup default to 0.7 for the learning processes in the ANN model. For this process, 300,000 iterations were used to achieve good consistency in the algorithm. The three error measuring parameters given by Sablani [21] are utilized to compare the performance of the various ANN configurations. Three parameters were used for the performances of the ANN configuration. These parameters were the mean relative error percentage (MRE %), the relative standard deviations of error (STD), the absolute fraction variance of error (R2). Their formulations are defined as follows:

$$MRE = \frac{1}{n} \sum_{i=1}^n ABS(A) \tag{11}$$

$$STD = \sqrt{\frac{\sum_{i=1}^n (A - \bar{A})^2}{n-1}} \tag{12}$$

$$R^2 = 1 - \left[ \frac{\sum_{i=1}^n (a_i - y_i)^2}{\sum_{i=1}^n (y_i)^2} \right] \tag{13}$$

Where; A = (P-D)/D. Parameter D and P are the experimental data and the estimated output from the modeled ANN respectively. The arithmetic mean of the numbers is  $\bar{A}$ , whereas the estimated output value is  $y_i$ , the experimental data is  $a_i$ , and the data number is n.

#### 4. Results and Discussion

The results show that with the increase of applied load, both the coefficient of friction and the wear rate values decrease under both dry sliding and HBSS lubrication conditions for the UHMW-PE polymer. For the range of speed and load values tested, the wear rate value and the coefficient of friction were higher under the dry sliding condition than the HBSS lubrication condition as shown in Figure 4 and Figure 5. Comparisons between the experimental data and the estimations by the ANN model for the coefficient of friction values at 50, 100, and 150N of applied load and various sliding speeds for both the dry sliding and HBSS lubrication conditions are shown in Figure 4.

The average friction factor was 0.2039 for the dry sliding condition and 0.1150 for the HBSS lubricate condition. The ratio of dry sliding to HBSS lubricate was 1.8 for the friction factor as shown in Figure 4. The

average specific wear rate value was 4.40 for the dry sliding condition and 3.14 for HBSS the lubrication condition.

Comparisons between the experimental data and the estimations by the ANN model for the wear rate at 38 N, 88 N, and 138 N of applied load and various sliding speeds for both the dry sliding and HBSS lubrication conditions are shown in Figure 5.

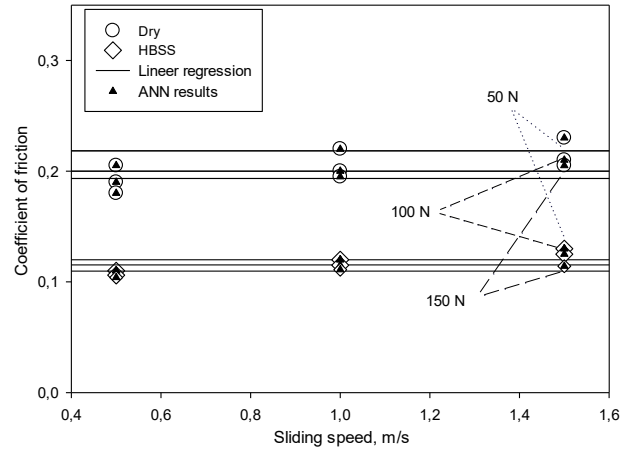


**Figure 4.** Comparisons of the coefficient of friction values between the experimental data and the ANN model estimations at 50N, 100N, and 150N of applied load under various sliding speeds.

The ratio of dry sliding to HBSS lubrication was 1.4 for wear rate as shown in Figure 5.

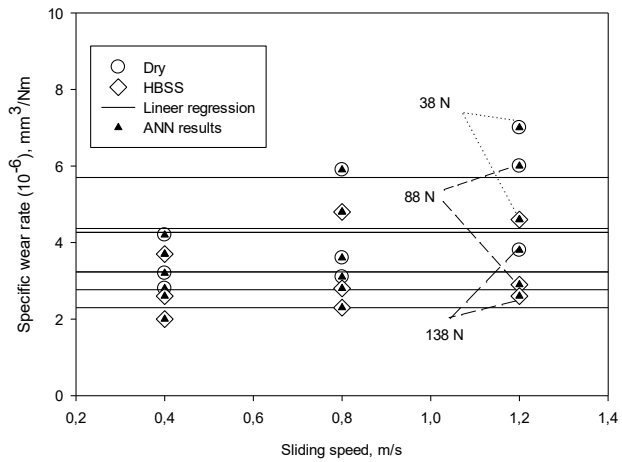


**Figure 5.** Comparison of the specific wear rate values between the experimental data and the ANN model estimated at 38N, 88N, and 138N of applied load under various sliding speeds.

This study investigated the applicability of artificial neural networks (ANN) for predicting both specific wear rate values and coefficients of friction of medical-grade UHMW-PE polymer in different sliding conditions. The

results show that the data predicted by the ANN analysis is consistent with the experimental test results. Comparison of the mean relative error percentage (MRE %), the absolute fraction variance of error ( $R^2$ ), and the relative standard deviations of error (STD) for the coefficient of friction are shown in Table 2 and the specific wear rate are shown in Table 3.

**Table 2.** Comparison of MRE,  $R^2$ , and STD for the coefficient of friction

Test Condition	Coefficient of friction			
	Load (N)	Sliding speeds (m/s)	Experimental results	ANN model results
Dry sliding	50	0.5	0.205000	0.205295
	50	1.0	0.220000	0.220056
	50	1.5	0.230000	0.229521
	100	0.5	0.190000	0.190695
	100	1.0	0.200000	0.198500
	100	1.5	0.210000	0.210655
	150	0.5	0.180000	0.179855
	150	1.0	0.195000	0.197533
	150	1.5	0.205000	0.205640
The mean relative error, MRE (%)				0.388528
The relative standard deviations of error, (STD)				0.002163
The absolute fraction variance of error ( $R^2$ )				1.000000
HBSS (Hank's balanced salt solution)	50	0.5	0.110000	0.110000
	50	1.0	0.120000	0.120000
	50	1.5	0.130000	0.130000
	100	0.5	0.106000	0.105999
	100	1.0	0.115000	0.115001
	100	1.5	0.125000	0.124998
	150	0.5	0.104000	0.104000
	150	1.0	0.111000	0.111001
	150	1.5	0.114100	0.114101
Mean relative error, MRE (%)				0.000628
The relative standard deviations of errors (STD)				0.002164
The absolute fraction variance of errors ( $R^2$ )				1.000000

The modeled ANN has 0.388528 and 0.005873 for the MRE result for the friction coefficient and the wear rate, respectively, for the dry sliding condition. For the HBSS lubrication condition, the ANN model has 0.000628 and 0.002580 for the MRE result for the coefficient of friction and specific wear rate, respectively. Absolute fractions of variances were 1 under both conditions. STD were 0.002163 and 0.046676 for the friction coefficient and wear rate, respectively, for the dry sliding condition.

For the HBSS lubrication condition, the ANN model has 0.002164 and 0.046680 of STD for the friction coefficient and wear rate, respectively, which were

consistent with the experimental results.

**Table 3.** Comparison of MRE,  $R^2$ , and STD for the specific wear rate

Test Condition	Specific wear rate			
	Load (N)	Sliding speeds (m/s)	Experimental results ( $10^{-6}$ )	ANN Model results ( $10^{-6}$ )
Dry sliding	38	0.4	4.200000	4.199650
	38	0.8	5.900000	5.900125
	38	1.2	7.000000	7.000000
	88	0.4	3.200000	3.200575
	88	0.8	3.600000	3.599575
	88	1.2	6.000000	5.999875
	138	0.4	2.800000	2.800000
	138	0.8	3.100000	3.099775
	138	1.2	3.800000	3.800125
The mean relative error, MRE (%)				0.005873
The relative standard deviations of error, (STD)				0.046676
The absolute fraction variance of error ( $R^2$ )				1.000000
HBSS (Hank's balanced salt solution)	38	0.4	3.300000	3.299900
	38	0.8	3.700000	3.700025
	38	1.2	5.600000	5.600000
	88	0.4	2.400000	2.399825
	88	0.8	2.800000	2.799950
	88	1.2	4.400000	4.400038
	138	0.4	2.300000	2.300000
	138	0.8	2.800000	2.799950
	138	1.2	3.300000	3.299900
Mean relative error, MRE (%)				0.002580
The relative standard deviations of errors (STD)				0.046680
The absolute fraction variance of errors ( $R^2$ )				1.000000

### 5. Conclusions

The following are the conclusions of this study;

- The coefficient of friction and wear rate of medical-grade UHMW-PE polymer under HBSS lubricated condition was lower than the dry sliding condition.
- The highest wear rate was  $7. \times 10^{-6}$  mm<sup>3</sup>/Nm for the UHMW-PE polymer at 1.2 m/s sliding speed and 38 N of load under the dry condition. The lowest wear rate was  $2.3 \times 10^{-6}$  mm<sup>3</sup>/Nm under the HBSS lubricated condition at 0.4 m/s sliding speed and 138 N load as shown in Table 3.
- For the range of lubricant conditions used in this investigation, the wear rate was highly influenced by the size of the applied load and the type of lubrication media. For the two lubricant conditions used in this tribological study, HBSS was a more effective lubricant than dry sliding.
- In this paper, we have suggested a new artificial

neural network (ANN) algorithm, which has feed-forward and backpropagation, to predict the specific wear rate and the coefficient of friction.

- The estimates for the wear rate values and the coefficient of friction by the ANN model were consistent with the experimental data.

- For the coefficient of friction, the ANN model has 0.194578% of average mean relative error and 1.0 of the absolute fraction of variance ( $R^2$ ) for both conditions. Also, for wear rate, the model has 0.0042265 % of mean relative error and 1.0 of the absolute fraction of variance ( $R^2$ ) for both conditions. The obtained results show that the use of the ANN for predicting the coefficient of friction and wear rate is a perfectly acceptable method.

### Declaration of Ethical Standards

The authors of this article declare that the materials and methods used in this study do not require ethical committee permission and/or legal-special permission.

### Conflict of Interest

The authors declare that they have no known competing financial interests or personal relationships that could have appeared to influence the work reported in this paper.

### References

- [1] Bartel D. L., Burstein A. H., Toda M. D., Edwards and D. L., 1985 The Effect of Conformity and Plastic Thickness on Contact Stresses in Metal-Backed Plastic Implants. *Journal of Biomechanical Engineering*, **107**(3), pp. 193–199.
- [2] Brach del Prever E. M., Bistolfi A., Bracco P., Costa L., 2009. UHMWPE for arthroplasty: Past or future?. *Journal of Orthopaedics and Traumatology*, **10**(1), pp. 1–8.
- [3] Chandrasekaran M., Loh N. L., 2001. Effect of counterface on the tribology of UHMWPE in the presence of proteins. *Wear*, **250**(1–12), pp. 237–241.
- [4] Briscoe B. J., Sinha S. K., 2002. Wear of polymers, *Proceedings of the Institution of Mechanical Engineers, Part J: Journal of Engineering Tribology*. **216**(6), pp. 401–413. 2002.
- [5] Lin T. Y., Tseng C. H., 2000. Optimum design for artificial neural networks: an example in a bicycle derailleur system. *Engineering Applications of Artificial Intelligence*, **13**(1), pp. 3–14.
- [6] Zamyad H., Naghavi N., Godaz R., Monsefi R., 2020. A recurrent neural network-based model for predicting bending behavior of ionic polymer-metal composite actuators. *Original Article Journal of Intelligent Material Systems and Structures*, **31**(17), pp. 1973–1985.
- [7] Kurt H H. I. and Oduncuoglu M., 2015. Application of a Neural Network Model for Prediction of Wear Properties of Ultrahigh Molecular Weight Polyethylene Composites. *International Journal of Polymer Science*, **315710**, pp. 1–11.
- [8] Velten K., Reinicke R., Friedrich K., 2000. Wear volume prediction with artificial neural networks. *Tribology International*, **33**(10), pp. 731–736.
- [9] Abdelbary A., Abouelwafa M. el Fahham N. I. M., Hamdy A. H., 2012. Modeling the wear of Polyamide 66 using artificial neural network. *Materials and Design*, **41**, pp. 460–469.
- [10] Rajesh D., Verma K., Kumar Kharwar P., Kumar Verma R., Mohan M., 2020. Artificial Neural Network-Based Modeling of Surface Roughness in Machining of Multiwall Carbon Nanotube Reinforced Polymer (Epoxy) Nanocomposites. *FME Transactions*, **48**(3), pp. 693-700.
- [11] Sabouhi R., Ghayour H., Abdellahi M., and Bahmanpour M., 2016. Measuring the mechanical properties of polymer-carbon nanotube composites by artificial intelligence. *International Journal of Damage Mechanics*, **25**(4), pp. 538-556.
- [12] Zhang Z., Friedrich K., Velten K., 2002. Prediction on tribological properties of short fibre composites using artificial neural networks. *Wear*, **252**(7–8), pp. 668–675.
- [13] Khan S. M., Malik S. A., Gull N., Saleemi S., Islam A., Butt M. T. Z., 2019. Fabrication and modelling of the macro-mechanical properties of cross-ply laminated fibre-reinforced polymer composites using artificial neural network. *Advanced Composite Materials*, **28**(4), pp. 409–423.
- [14] Gyurova L. A., Friedrich K., 2011. Artificial neural networks for predicting sliding friction and wear properties of polyphenylene sulfide composites. *Tribology International*, **44**(5), pp. 603–609.
- [15] Kazi M. K., Eljack F., Mahdi E., 2020. Optimal filler content for cotton fiber/PP composite based on mechanical properties using artificial neural network. *Composite Structures*, **251**, pp. 1-7.
- [16] Pajchrowski T., Siwek P., Wójcik A., 2020. Adaptive controller design for electric drive with variable parameters by Reinforcement Learning method. *Bulletin of the Polish Academy of Sciences:*



Technical Sciences, **68**(4), pp. 1019–1030.

- [17] Rajeev D., Dinakaran D., Singh S. C. E., 2017. Artificial neural network based tool wear estimation on dry hard turning processes of AISI4140 steel using coated carbide tool. *Bulletin of the Polish Academy of Sciences: Technical Sciences*, **65**(4), pp. 553–559.
- [18] Ufnalski B., Grzesiak L. M., 2012. Particle swarm optimization of artificial-neural-network-based on-line trained speed controller for battery electric vehicle. *Bulletin of the Polish Academy of Sciences: Technical Sciences*, **60**(3), pp. 661–667.
- [19] Ermis K., Sen Y., 2017. Investigating Performance on Intercooler in Turbocharger Diesel Engine with ANN. 5th International Symposium on Innovative Technologies in Engineering and Science, Baku – Azerbaijan, 29-30 September, pp. 1383–1392.
- [20] Şen Y., Ekmekçi İ., Çallı İ., 2003. Açık kanatlı düz çarklı sirkulasuon pompalarında sıcaklığa bağlı Değişimlerin Yapay sinir ağları ile analizi. International XII Symposium of Artificial Intelligence and Neural Networks. Çanakkale, Turkey, 02-04 July, pp. 1-7.
- [21] Sablani S. S., Kacimov A., Perret J., Mujumdar A. S., Campo A., 2005. Non-iterative estimation of heat transfer coefficients using artificial neural network models. *International Journal of Heat and Mass Transfer*, **48**(3–4), pp. 665–679.

